Master's thesis

NTNU
Norwegian University of Science and Technology
Faculty of Medicine and Health Sciences
Kavli Institute for Systems Neuroscience

Anna Mikalsen Kollstrøm

How does ALS pathology spread to affect healthy neurons? Recapitulation of disease progression in multi-nodal neural networks *in vitro*

Master's thesis in Neuroscience

Supervisor: Ioanna Sandvig (PhD), Axel Sandvig (MD, PhD), Vegard Fiskum (PhD candidate)

June 2020

NTNU
Norwegian University of Science and Technology

Anna Mikalsen Kollstrøm

How does ALS pathology spread to affect healthy neurons? Recapitulation of disease progression in multi-nodal neural networks *in vitro*

Master's thesis in Neuroscience
Supervisor: Ioanna Sandvig (PhD), Axel Sandvig (MD, PhD), Vegard Fiskum (PhD candidate)
June 2020

Norwegian University of Science and Technology
Faculty of Medicine and Health Sciences
Kavli Institute for Systems Neuroscience

NTNU
Norwegian University of
Science and Technology

Abstract

Amyotrophic lateral sclerosis (ALS) is a neurodegenerative disease affecting upper and lower motor neurons, resulting in a gradual weakening of voluntary muscles and eventually leading to death due to respiratory failure. Research on the genetic mutations causing ALS over the past decades has revealed several underlying disease mechanisms which also have implications for sporadic cases. Yet, exactly how the disease progresses to affect more and more motor neurons remains largely unknown. Traditional research on ALS has been mostly dependent on animal models, however, recent technological and genetic advances have made *in vitro* cell-based models a promising approach for the study of disease mechanisms in ALS. To this end we used 3-nodal microfluidic devices with microelectrode array (MEA) interface to create a lab-on-a-chip platform that can be used to monitor the electrophysiological activity generated by structured neural networks. With this model as a base, we performed three experiments. First, we established structured neural networks with rat cortical neurons, and perturbed one of the nodes with NMDA to assess the effects of the spread of perturbations in terms of altered electrophysiological activity and synchronization across the network. We found that overactivation in one of the fluidically isolated nodes caused increased synchronization across the entire network. Secondly, we used an MEA platform to examine differences in the electrophysiological activity of healthy and ALS patient-specific IPSC-derived neurons in single networks at baseline and in response to stress-inducing hypoxic conditions. The activity level of the ALS-specific neurons was very low, and due to issues with correct differentiation of these cells it was difficult to compare them to the healthy controls. Finally, we established structured 3-nodal neural networks with directly reprogrammed motor neurons from human adult fibroblasts from a patient with confirmed ALS in one of the peripheral nodes, and from healthy individuals in the other two nodes (ALS-healthy-healthy), to study the spread of altered activity caused by the ALS-specific neurons. The directly reprogrammed fibroblasts did not develop into fully mature neurons and did not form axonal connections between the nodes. The conclusion of this work is that this model is relevant for the investigation of structure-function dynamics of neural networks and how such dynamics shape the spread of neurodegenerative disease, however, many challenges remain before this approach reaches its full potential.

Sammendrag

Amyotrofisk lateral sklerose (ALS) er en nevrodegenerativ sykdom som påvirker øvre og nedre motornevroner, hvilket fører til en gradvis lammelse av muskler og som til slutt resulterer i død på grunn av respirasjonssvikt. Forskning på de genetiske mutasjonene som forårsaker ALS har i løpet av de siste tiårene avdekket flere underliggende sykdomsmekanismer som også har implikasjoner for sporadiske tilfeller av sykdommen. Det er likevel fortsatt uvisst hvordan sykdommen sprer seg til å påvirke flere og flere motornevroner. Tradisjonell forskning på ALS har i stor grad vært basert på dyremodeller, men nylige teknologiske og genetiske fremskritt har gjort *in vitro* celle-baserte modeller til en lovende tilnærming for å studere sykdomsmekanismer i ALS. Her brukte vi 3-nodale mikrofluidiske brikker med mikroelektroder for å skape en «laboratorie på chip»-plattform som kan brukes til observasjon av den elektrofysiologiske aktiviteten til strukturerte nevrale nettverk. Med denne modellen som grunnlag utførte vi tre eksperimenter. Først etablerte vi strukturerte nevrale nettverk med kortikale nevroner fra rotter, og perturberte en av nodene med NMDA for å studere effektene av spredningen av en slik perturbering på den elektrofysiologiske aktiviteten og synkroniseringen av aktiviteten i nettverket. Vi fant at overaktivering i en av nodene førte til økt synkronisering gjennom hele nettverket. Videre brukte vi en mikroelektrode-plattform for å utforske forskjellene i den elektrofysiologiske aktiviteten til nevroner fra friske individer og fra ALS-pasienter før og etter stress-fremkallende hypoksi. Aktivitetsnivået i ALS-nevronene var veldig lavt og vi fant dermed ingen klare forskjeller ettersom det ble vanskelig å sammenligne mellom de to gruppene. Til slutt etablerte vi strukturerte 3-nodale nevrale nettverk med direkte reprogrammerte humane fibroblaster fra en ALS-pasient i en av de perifere nodene, og fra friske individer i de to andre nodene (ALS-frisk-frisk), for å studere spredningen av endret aktivitet forårsaket av ALS-nevronene. De direkte reprogrammerte fibroblastene utviklet seg ikke til modne nevroner og formet ikke aksoner og forbindelser mellom nodene. Konklusjonen av dette arbeidet er at denne modellen er relevant for utforskningen av forholdet mellom struktur og funksjon i nevrale nettverk, og hvordan dette forholdet former spredningen av nevrodegenerative sykdommer, men mange utfordringer gjenstår før denne modellen når sitt fulle potensial.

Acknowledgements

This project was carried out in the Sandvig lab at the Department of Neuromedicine and Movement Science, Faculty of Medicine and Health Sciences under the supervision of Dr. Ioanna Sandvig. I would like to express my deepest gratitude towards several people in the group.

First of all, I would like to thank Ioanna and Axel Sandvig for giving me the opportunity to do my master's project in your group. Thank you for all support, advice and problem solving. I have learned so much through this year and you have provided me with invaluable skills for developing into a critical and independent thinker and researcher. I would also like to thank my co-supervisor Vegard Fiskum for the opportunity to collaborate with him on this exciting project. I am immensely grateful for the countless hours and effort you have put in with regards to lab work and the writing process, and for keeping me motivated despite the setbacks along the way.

Thanks to Ulrich, for all the help and patience during my final experiment. I would also like to thank Ola, Lars and all the other members of the group for always being available to answer any question I may have. A special thank you to Nicholas, both for all the effort you put in with my data analyses, and for keeping me sane during the final stages.
Thanks to Nicolai, for your dedication towards making the microfluidics work, and for your much appreciated late-night shifts at the Nanolab.

I also want to thank my fellow master students, Rikke and Marit, for all the conversations, the support, and for letting me vent my frustration when things (inevitably) go wrong. Last but not least, thanks to my family, especially my sister Selma, for all the encouragement along the way.

Table of contents

Table of figures

Abbreviations

ALS	Amyotrophic Lateral Sclerosis
AMPA	α-amino-3-hydroxy-5-methyl-4-isoxazolepropionic acid
AP	Action potential
APP	Amyloid precursor protein
ATP	Adenosine triphosphate
ATRA	All-trans retinoic acid
B-27	B-27 Plus supplement
BDNF	Brain-derived neurotrophic factor
C9orf72	Chromosome 9 open reading frame 72
c-Myc	MYC proto-oncogene, BHLH transcription factor
CI	Coherence index
CNS	Central nervous system
CNTF	Ciliary neurotrophic factor
DIV	Days in vitro
D-MEM	Dulbecco's Modified Eagle Medium
Dox	Doxycycline
DPBS	Dulbecco's phosphate buffer saline
DTI	Diffusion Tensor Imaging
EAAT2	Excitatory amino acid transporter 2
EEG	Electroencephalography
Epha4	Ephrin type-A receptor 4
ER	Endoplasmic reticulum
FALS	Familial ALS
FBS	Fetal bovine serum
FM	Fibroblast media
FTD	Frontotemporal dementia
FTLD	Frontotemporal lobar degeneration
FUS	Fused in Sarcoma
GABA	Gamma-Aminobutyric acid
GDNF	Glial cell-derived neurotrophic factor
GFAP	Glial fibrillary acidic protein
ISL1	Islet1
Klf4	Kruppel-like factor 4
LHX3	LIM/homeobox protein
LTD	Long-term depression
LTP	Long-term potentiation
MEG	Magnetoencephalography
MEAs	Microelectrode arrays
MEM NEAA	Minimum essential medium Non-essential Amino Acid solution
MIP	Microfluidic chip
miRNAs	micro RNAs
MNs	Motor neurons
NM	Neuronal media
NMDA	N-methyl-D-aspartate
NMJ	Neuromuscular junction
NT-3	Neurotrophin-3
Oct3/4	Organic cation/carnitine transporter 4

PBS	Phosphate buffer saline
PFA	Paraformaldehyde
PD	Parkinson’s disease
PDMS	Polydimethylsiloxane
PEI	Polyethyleminine
PLO	Poly-L-ornithine
PNS	Peripheral nervous system
RNS	Reactive nitrogen species
ROS	Reactive oxygen species
SALS	Sporadic ALS
Sema3A	Semaphorin 3A
SGZ	Subgranular zone
SVZ	Subventricular zone
SoC	Self-organized criticality
SOD1	Cu/Zn superoxide dismutase 1 (SOD1)
Sox2	SRY (sex determining region Y)-box 2
TARDBP	Transactive response DNA binding protein
TDP-43	TAR DNA-binding protein 43
UPR	Unfolded protein response

Introduction

1.1 Amyotrophic lateral sclerosis

Amyotrophic lateral sclerosis (ALS) is a neurodegenerative disease affecting upper and lower motor neurons (MNs). ALS is characterized by a progressive loss of MNs in the primary motor cortex (upper MNs) and in the brainstem and spinal cord (lower MNs), which results in a gradual weakening of voluntary muscles, eventually leading to death due to respiratory failure[1]. ALS is categorized into sporadic (SALS) and familial forms (FALS). 90-95 % of ALS cases are thought to be sporadic, meaning there are no clear underlying genetic factors, whilst 5-10 % are familial and associated with a genetically inherited component[2]. Interestingly, some of the genes associated with FALS have also been implicated in sporadic cases of ALS[1]. Nevertheless, the lack of specific biomarkers for ALS makes the disease difficult to diagnose, and patients are usually not diagnosed until 13-18 months after they begin to experience symptoms due to the subtle and gradually developing symptoms[2]. There is currently no effective treatment available and patients usually die within three to five years. One drug, riluzole, has been demonstrated to increase survival, but the effect on muscle degradation is limited[1]. Thus, there is an urgent need to increase our understanding of the causes and risks underlying ALS, particularly how the disease progresses to increasingly affect more and more MNs.

Symptoms in ALS start to emerge when axons retract, resulting in denervation of lower MNs or the muscle[3]. The most common symptoms are muscle weakness, twitching and cramping, and, although highly variable, the first onset of symptoms is usually between the ages of 50 and 65[2]. Unlike other neurodegenerative diseases like dementia and Parkinson's disease (PD), ALS is not considered a geriatric disease, but age is considered a risk factor and juvenile onset is rare[3]. In most patients, ALS first affects the limbs (spinal onset), but one fifth of patients experience speech or swallow problems at onset (bulbar onset)[3]. Degeneration of neurons in the prefrontal and temporal cortex results in frontal executive dysfunction and frontotemporal dementia (FTD) in about 15 % of patients. This is called ALS with frontotemporal lobe degeneration (FTLD). Many patients experience cognitive impairments without meeting the criteria for FTLD, and ALS and FTLD are therefore considered to be at opposite ends of the same disease spectrum[3]. As the disease progresses there is a gradual impairment of muscles, but extraocular muscles and those that control bowel and bladder function remain intact in the early phases of the disease[4]. Many patients develop symptoms of dyspnea and dysphagia, and death ultimately results from respiratory failure[2]. Post-mortem examinations show degeneration of MNs in the motor cortex, brainstem, motor nuclei and anterior horns in the spinal cord[4]. Remaining MNs accumulate deposits of aggregated proteins, called inclusions. In many patients, a major component of these inclusions is ubiquitinated and phosphorylated transactive response DNA-binding protein 43 (TDP-43)[3].

The molecular mechanisms resulting in MN degeneration are not fully understood, but several pathophysiological events have been related to ALS, including excitotoxicity, mitochondria dysfunction, dysregulated calcium homeostasis, oxidative and endoplasmic reticulum (ER) stress, stress granules (i.e. aggregates of proteins and RNA molecules generated in a reversible manner upon cellular stress to temporarily stall mRNA translation), aggregated proteins (i.e. accumulations of unfolded proteins that are often

constituents of stress granules in neurodegenerative diseases) and deficits in the unfolded protein response (UPR)[4,5]. However, whether these are initiating factors or later consequential events that result in MN vulnerability remains to be determined[5]. ALS is also a heterogeneous disease, with different molecular pathways being involved in different types of familial and sporadic ALS cases. Furthermore, different mutations can induce various phenotypes, and lead to ALS in some individuals, while causing FTD in others[3]. In addition, factors like region of onset, age of onset, disease duration and association with other conditions contribute to the heterogeneity. Non-motor symptoms such as cognitive impairment also adds to the complexity of the disease[6]. Thus, the mechanisms leading to MN degeneration are multifactorial and both loss-of-function and gain-of-function mechanisms appear to be at play. This constitutes a major obstacle in identifying the underlying causes of ALS as there is not one single disease mechanism leading to MN death, but it also offers many opportunities for therapeutic interventions[3]. Nevertheless, the wide range of possible underlying causes also complicates the search for a cure as intervening with one mechanism may not be sufficient to stop MN degeneration.

1.1.2 Genetic mutations in ALS

A considerable amount of knowledge about the pathophysiological mechanisms involved in ALS has been revealed by studying the genetic mutations, and this has implications also for SALS as the same genetic factors have turned out to be major components in sporadic cases[4]. The genes associated with ALS are usually involved in either protein quality control, RNA homeostasis or cytoskeletal dynamics[4]. The majority of FALS cases are due to mutations in the Cu/Zn superoxide dismutase 1 (SOD1) gene or expansions in the noncoding GGGGCC hexanucleotide repeat located in the first intron of the chromosome 9 open reading frame 72 (C9orf72). The SOD1 gene was the first ALS gene to be discovered and is involved in detoxification of reactive free radicals in the cell[7]. Exactly how mutations in SOD1 result in MN degeneration is incompletely understood, but the toxic function of mutant SOD1 seems to be caused by several acquired toxicities, rather than a loss-of-function of dismutase activity[8]. Mutant SOD1 misfolds but seems to escape the normal degradation process and forms ubiquitinated cytoplasmic inclusions[3,4]. The misfolded protein itself has been demonstrated to be directly toxic for several intracellular processes like mitochondrial energy production and axonal transport. Mutant SOD1 has also been suggested to indirectly inhibit the proteasome by "overloading" the proteasome degradation pathway with misfolded protein aggregates[8]. Nevertheless, reduction of mutant SOD1 aggregates fails to increase survival in mice, suggesting that these aggregates are not necessary for disease progression, and might instead be part of a protective mechanism[4,9]. Since the discovery of the SOD1 mutation, approximately 26 other genes have been identified[6].

C9orf72 expansions are thought to be implicated in several processes involving vesicular trafficking, RNA processing and nuclear trafficking[10]. Healthy individuals normally have less than 10 repeats, while ALS patients can have thousands. The mechanisms by which repeat expansions cause ALS remains to be determined, but both loss-of-function and gain-of-function mechanisms have been proposed. The mutation leads to a reduction in C9orf72 protein, which results in abnormal microglial responses[4]. However, this likely does not cause disease and thus it has been proposed that C9orf72 repeat expansions generates abnormal RNAs, possibly through aberrant recruitment of RNA-binding proteins[3]. Alternatively, alterations in translation may produce potentially toxic dipeptide repeat proteins[3,4].

In 2006, the RNA-binding protein TDP-43 was identified as one of the major components of the cytoplasmic inclusions in affected areas of the brain and spinal cord of patients with ALS and FTLD[11]. In normal conditions, TDP-43 binds DNA and RNA and play a role in transcription, RNA splicing and transport[3]. Mutations alter the functionality of TDP-43 in several ways: increased propensity to aggregate, enhanced cytoplasmic mislocalization, altered protein stability, resistance to proteases and modified binding interactions with other proteins[12]. Mutations in the TARDBP gene encoding TDP-43 have been identified in some cases of FALS, and hyperphosphorylated and ubiquitinated TDP-43 is a hallmark of most sporadic cases of ALS[1,13]. Aggregates of TDP-43 have also been observed in several brain regions in C9orf72 mutations[6]. Normally, TDP-43 is located in the nucleus, but in response to stressors it is mainly found in the cytoplasm where it associates with stress granules[3]. When stress resolves, the stress granules disaggregate and TDP-43 relocates to the nucleus. However, in ALS, it is thought that stress granules constitute a pro-aggregation environment in which TDP-43 accumulate. This results in mRNA splicing deficits. TDP-43 subsequently undergoes modifications like hyperphosphorylation and ubiquitylation, but whether these secondary steps are necessary for ALS pathology is unclear[3]. The involvement of TDP-43 in sporadic cases of ALS, as well as its role in different cases of FALS and FTLD have led to the notion that TDP-43 may play a role similar to that of α-synuclein in PD and amyloid precursor protein (APP) in AD[13]. In fact, TDP-43 pathology has also been found in AD cases[14]. However, while overexpression of α-synuclein and APP is enough to induce PD and AD, a similar function for TDP-43 in ALS has not yet been identified[3].

1.1.3 Disease mechanisms in ALS

The progressive pattern of MN degeneration is similar between cases of FALS and SALS, and as such suggest a common disease mechanism[6]. Neuronal hyperexcitability is a frequently reported feature in ALS patients and has been demonstrated across different genetic mutations[15]. It is well established that hyperexcitability occurs early in ALS, but some studies also report a hypoexcitable cortex in later stages of the disease, which indicates that MN excitability may change during progression of ALS (see ref. 15 for a review on hyperexcitability in ALS).

Hyperexcitability is likely to be caused by several factors and involving several cell types, including neurons, astrocytes and interneurons[15]. One potential mechanism is disruption of inhibitory circuits mediated by GABAergic interneurons. Post-mortem investigations of primary motor cortex tissue of human ALS patients have indicated downregulation of the expression of genes encoding GABA receptors on MNs[16]. Yet, it is unclear whether the disruption is only due to a downregulation of GABA receptors, or if it is instead caused by a loss of GABAergic interneurons, or a combination of both[15]. Alterations in sodium (Na^+) and potassium (K^+) channels have been proposed as a MN-specific mechanism contributing to hyperexcitability[15]. Increased Na^+-channel conductance and currents have been found in the SOD1 mouse model[17]. This causes a decrease in the action potential (AP) refractory period and thus increases repeated firing[15]. Furthermore, reduction in K^+-channel expression, which results in decreased AP threshold, has been documented post-mortem in tissue from ALS patients[18]. A third proposed mechanism is that hyperexcitability is caused by overstimulation of MNs by excessive extracellular glutamate[15]. Most of the glutamate reuptake in the brain is mediated by astrocytes *via* the glutamate transporter EAAT2, but studies have demonstrated that EAAT2 is downregulated in ALS[19]. Furthermore,

impaired astrocytic function has also been suggested to impair K^+ homeostasis, and excess levels of K^+ in the extracellular space can depolarize the resting membrane potential and increase excitability[15]. In summary, hyperexcitability seems to be caused by an interplay of several mechanisms mediated by different cell types, but these mechanisms are not yet understood well enough to determine the exact cause of hyperexcitability[15].

Whether and how hyperexcitability may lead to MN death remains to be elucidated, but it likely contributes to oxidative stress, i.e. the cytotoxic consequences resulting from an imbalance between the levels of oxygen radicals and antioxidants in the cell[20]. Accumulation of reactive oxygen species (ROS) and reactive nitrogen species (RNS) inside the cell can result in oxidative stress[6]. Repetitive firing and excitotoxicity mediated by over-stimulation of glutamate receptors contributes to this accumulation by increasing the levels of calcium (Ca^{2+}) that enters the cell[6]. The ER and mitochondria are responsible for maintaining Ca^{2+} homeostasis, but excessive levels of Ca^{2+} affect several mitochondrial processes and result in increased ROS production and oxidative stress[21]. Furthermore, these factors work in a feedback-loop, where increased oxidative stress increases mitochondrial stress, resulting in generation of more ROS[5]. Oxidative stress also induces stress responses in other organelles, like the ER, and continuous stress and oxidative conditions can result in abnormal protein folding in the ER. This leads to an accumulation of misfolded proteins which again contributes to the cellular stress responses mediated by the ER and mitochondria. Chronic oxidative stress can impair axonal transport mechanisms leading to a depletion of mitochondria at the axon terminal. This results in insufficient ATP production at the distal part of the axon, and the synapse begin to degenerate[5]. Simultaneously the stressed mitochondria can initiate apoptosis[21].

Several factors make MNs particularly vulnerable to excitotoxicity. First of all MNs have low Ca^{2+}-buffering capacity due to the low expression of calcium buffering proteins[22]. One study found that spinal MNs did not express the Ca^{2+}-binding proteins parvalbumin and calbindin, whereas less vulnerable neurons such as oculomotor neurons did express Ca^{2+}-binding proteins[23]. The mitochondria thus become the major Ca^{2+}-buffer in vulnerable MNs, making the mitochondria sensitive to increases in Ca^{2+} levels[22]. Secondly, MNs possess a high number of Ca^{2+}-permeable glutamate AMPA-receptors. AMPA-receptors lacking the GluR2 subunit have a high permeability to Ca2+, and this subunit appears to be more sparsely expressed in MNs compared to other cell types[24]. This property may be crucial in normal motor function as it allows the MNs to act fast upon stimulation. However, in response to alterations in Ca^{2+} levels MNs may become more sensitive to Ca^{2+} overload. Lastly, the relative size of the MNs may make them more vulnerable to excitotoxicity and cellular stress. MNs can have long axonal projections, and as such have large energy demands. This makes MNs particularly vulnerable to reduced ATP production[5]. Although excitotoxicity is not the only mechanism involved in MN degeneration in ALS, the combination of these features can make the consequences of excitotoxicity more devastating for MNs compared to other neuronal subtypes.

1.1.4 Disease spread in ALS

Despite the increasing amount of knowledge about the molecular mechanisms involved in ALS, little is known about where the disease begins or the mechanisms by which it spreads. Neurodegeneration in ALS is further complicated by the fact that not all MNs are equally affected by the disease. The disease targets specific networks in the brain, brainstem and spinal cord, indicating that neuronal circuitry might drive the disease to specific MN

populations[6]. It has further been suggested that pathogenic molecules can spread from cell to cell *via* axonal transport, however, the directionality of this progression is a matter of debate[13]. In the literature, disease spread in ALS is therefore described as a "dying-forward" or a "dying-back" process.

The "dying-forward" hypothesis proposes an anterograde pattern of degeneration that begins in the cortical MNs and spreads *via* monosynaptic connections to the anterior horn cells of the spinal cord[25]. The "dying-back" hypothesis propose instead that degeneration starts at the nerve terminal or neuromuscular junction (NMJ), and spreads *via* retrograde transport of pathogens toward the UMNs[26]. Most of the evidence for this view comes from studies on the transgenic SOD1 mouse model, which have revealed alterations at the neuromuscular junction before the onset of clinical symptoms and neuronal degeneration[27,28]. However, ALS pathology can spread over considerable distances to certain populations of MNs while others remain unaffected, and most of the neurons in affected regions receive projections from neocortical pyramidal cells[13]. This indicates that the site of origin is in the cerebral cortex. Further evidence for this is provided by the fact that populations of MNs without direct projections to cortical areas are spared in ALS, such as the oculomotor MNs[29]. Moreover, TDP-43 pathology mainly develops in structures receiving direct cortical projections (Fig. 1)[13,29]. For pathogens to spread to the UMNs via retrograde transport from the NMJ, the cerebellum and the pallidum would be needed, but none of these regions develop TDP-43 pathology in ALS[13]. Thus, anterograde degeneration of MNs can explain how ALS spreads over large distances, while preserving MN populations in close proximity to the original insult.

The hypothesis that ALS pathology spreads transsynaptically from cell to cell is consistent with a prion-like mechanism for disease spread. Neurodegeneration in ALS is accompanied by misfolded protein inclusions most commonly formed by TDP-43, but also by SOD1 or Fused in Sarcoma (FUS). Evidence suggest that these inclusions propagate in a manner similar to that of prion diseases. Prion diseases are characterized by misfolded proteins with the ability to spread and alter the conformation of normal protein[30]. In vitro studies have shown that small amounts of aggregates of TDP-43, SOD1 and FUS can induce misfolding of normal protein, and the pattern of spread of TDP-43 pathology based on analysis of autopsy cohorts suggest that TDP-43 induce changes in normal protein as it propagates[31,32]. But unlike prion diseases, neurodegenerative diseases cannot spread from individual to individual and are therefore referred to as "prion-like"[31,33]. However, one study found that astrocytes expressing mutated SOD1 release soluble factors that can spread from the culture media and selectively induce pathology in MNs[34]. Thus, this suggests that ALS pathology can spread via the extracellular space, but there are yet no indications of disease being transmitted by exposure to tissue. Nevertheless, further investigations are necessary to determine the similarities between neurodegenerative diseases and prion diseases. Studies have shown that SOD1 aggregates can spread intercellularly by release of aggregates from dying cells, or by packaging of misfolded protein seed into extracellular vesicles[35]. It has later been demonstrated that SOD1 aggregation can also spread *via* synaptic transmission[36]. A prion-like propagation of aggregates *via* synaptic transmission has also been demonstrated for TDP-43[37]. Thus, evidence suggest that ALS spreads in a prion-like manner, and, more importantly, that it can spread via axons.

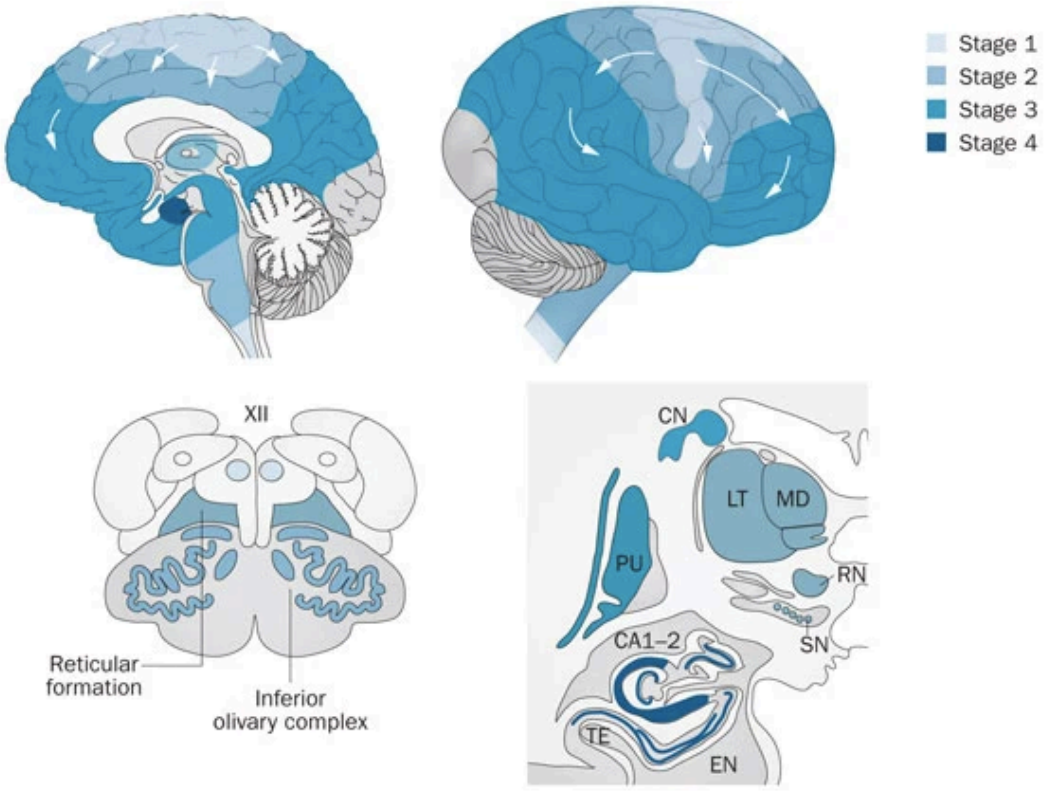

Fig. 1. Progression of TDP-43 pathology in ALS. Based on the distribution of TDP-43 aggregates in post-mortem tissue it has been proposed that the progression of ALS can be divided into four main stages. In stage 1, lesions develop in the agranular neocortex and bulbar (XII)/spinal somatomotor neurons. In stage 2, pathology develops in the reticular formation, precerebellar nuclei and the lateral and medial thalamus (LT, MD). TDP-43 aggregates also start to develop in the parvocellular portion of the red nucleus (RN) and pars compacta of the substantia nigra (SN). In stage 3, lesions develop in the postcentral neocortex and striatum (caudate nucleus (CN) and putamen (PU)). In stage 4, the transentorhinal (TE) and entorhinal (EN) regions become involved, along with the hippocampal area CA1-2 and the dentate fascia. (Figure from ref. 13.)

The connectivity architecture of the brain, the connectome, shapes how the brain responds to perturbation[38]. Axonal propagation of pathogenic seeds (protein aggregates) can facilitate the spread of disease over considerably large distances and affect brain areas relatively remote from the initial starting point. Disease spread follows interconnected areas of the brain rather than spreading locally, and it spreads more extensively between areas with a large number of direct projections, making such areas particularly vulnerable[13]. This has implications for how the disease functionally affects the individual, as remote regions can be functionally or structurally altered and affect functions related to such areas, whereas other areas without direct projections to the starting point can retain function, at least in early stages of the disease[38]. However, perturbations can also spread beyond direct projections. Computational modeling of cortical interactions has suggested that lesions can affect functional connectivity well beyond the injury site[39]. It is therefore plausible that as more and more areas are affected by disease spread through direct

connections, pathology can also spread to more distant sites that are not necessarily directly connected to the starting point. Effectively, this makes the entire network vulnerable to perturbations, not just the site of origin. As a consequence, the individual develops an increasing number of symptoms as the disease progresses to affect more and more brain areas.

There is increasing evidence that disease progression in ALS is not only driven by MNs, but also by their neighboring non-neuronal cells. Glial cells include microglia, astrocytes, oligodendrocytes and Schwann cells, and these provide nutritional and immunoprotective support for neurons. ALS and other neurodegenerative diseases are accompanied by a neuroinflammatory response mediated by glial cells, mainly microglia and astrocytes[40]. Studies in mice have shown that the selective expression of SOD1 in MNs only does not lead to neurodegeneration, indicating a crucial role for glial cells in MN death[41,42]. Furthermore, deletion of SOD1 from microglia and astrocytes slowed disease progression, but did not affect disease onset, suggesting that microglia and astrocytes are involved in disease progression rather than disease initiation[43,44]. In ALS, microglia and astrocytes become more reactive and adopt changes in morphology which may result in reduced support for MNs[40]. For example, alterations in the expression of EAAT2 on astrocytes reduces the ability to maintain glutamate homeostasis[19]. Additionally, both microglia and astrocytes can contribute to MN degeneration more directly by promoting generation of ROS and RNS[40]. A role for oligodendrocytes has also been implicated in ALS. A neuroinflammatory process has been documented for oligodendrocytes before MN death is apparent, suggesting a role in disease onset[45]. Loss of oligodendrocytes are replaced by NG2 cells, however, these are functionally impaired and cannot compensate for the loss of metabolic support provided by oligodendrocytes[45]. Thus, glial cells are involved in several processes contributing to both disease onset and disease progression in ALS. Consequently, ALS cannot only be regarded purely as a MN disease, as this classification does not fully capture all the pathological processes involved in disease progression. Therefore, there is an urgent need for more research to elucidate where the disease begins and how it propagates, both from neuron to neuron and between neurons and non-neuronal cells.

1.2 Models of ALS

The discovery of ALS causing genes has led to the development of several animal models, including primate, rodent, zebrafish, worm and fly models[46]. These models have in combination with post-mortem investigations of ALS patients revealed many disease mechanisms contributing to MN degeneration. However, post-mortem investigations are usually made at the end stage of the disease and animal models cannot fully recapitulate central aspects of the disease observed in humans. For example, the SOD1 mouse model does not show substantial cortical neurodegeneration, a requirement for diagnosis in humans, and TDP-43 mice show a very mild loss of neurons compared to ALS patients (see ref. 46 for a review on ALS rodent models). Furthermore, several promising experimental treatments in animal models have been unsuccessful when tested in humans[47]. Thus, animal models used in ALS research should be improved, however, this may prove difficult due to the high variability in disease pathogenesis in ALS patients[46]. Instead, recent technological and genetic advances have made *in vitro* cell-based models a promising alternative or supplement to animal models, as such models make it possible to directly investigate ALS in patient-derived cells[48].

In 2006, Yamanaka and Takahashi demonstrated that adult somatic cells could be converted into induced pluripotent stem cells (iPSCs) by adding four transcription factors (Oct3/4, Sox2, c-Myc and Klf4)[49]. These cells can be used to study development of tissues and organs, and reprogramming of patient-specific cells can be used for disease modeling and drug screening[50]. iPSC technology thus makes it possible to derive ALS patient-specific cells from minimally invasive skin biopsies and study these *in vitro*. Although removed from their microenvironment, these cells still show many neuropathological hallmarks of ALS and there are several advantages of using iPSCs[46,48]. For example, there is no need to overexpress the transgene with the disease-causing mutation, and gene editing tools make it possible to correct the mutations and generate isogenic controls with the same genetic background as the patient[51]. The iPSC technology also makes it possible to study sporadic cases of neurodegenerative diseases, and introduction of reprogramming factors provide the opportunity to differentiate iPSCs into different subtypes of cells, e.g. upper and lower MNs and astrocytes[48]. Nevertheless, there are still a number of limitations to the iPSC technology. A central one includes the reset of age-related phenotypes. Age is a risk factor for neurodegenerative diseases and the disease usually develops over several years. It is therefore likely that aging of the cells is critical for the development of several disease-associated phenotypes[48]. Additional influences such as environmental factors also contribute to the unique individual epigenetic phenotypes that can affect disease progression. All of these phenotypes are reset when the cells are converted back to a stem cell stage, and iPSC-derived neurons are closer to fetal stages rather than adult stages[52]. Thus, to properly model late stages of ALS *in vitro*, it is necessary to maintain the age-related and epigenetic imprint of the cells.

The emergence of iPSC technology also inspired the development of direct reprogramming techniques, and the discovery that a combination of neural-lineage specific transcription factors could be used to directly convert fibroblasts from mice into neurons has made it possible to circumvent the stem cell stage altogether and maintain age-related and epigenetic markers in the cells (Fig. 2)[53]. Since then, other studies have confirmed the applicability of such methods for human-derived fibroblast, and the possibility of generating subtypes of neurons, offering great potential for studying neurodegenerative diseases that target specific subpopulations of neurons[54,55]. Directly converted neurons have also been shown to retain age-related changes in the epigenetic clock, the transcriptome and microRNAs (miRNAs), ROS levels, DNA damage and telomere lengths[56,57]. Thus, as iPSCs are unable to capture several important risk factors in disease, direct neuronal reprogramming can provide a more accurate depiction of the pathogenesis of ALS. One study has successfully demonstrated the recapitulation of age-related disease phenotypes in directly converted cells from Huntington's patients[58]. However, although MNs have been successfully generated from directly converted fibroblasts, it still remains to be demonstrated whether cultured patient-derived MNs can be used to model ALS[56].

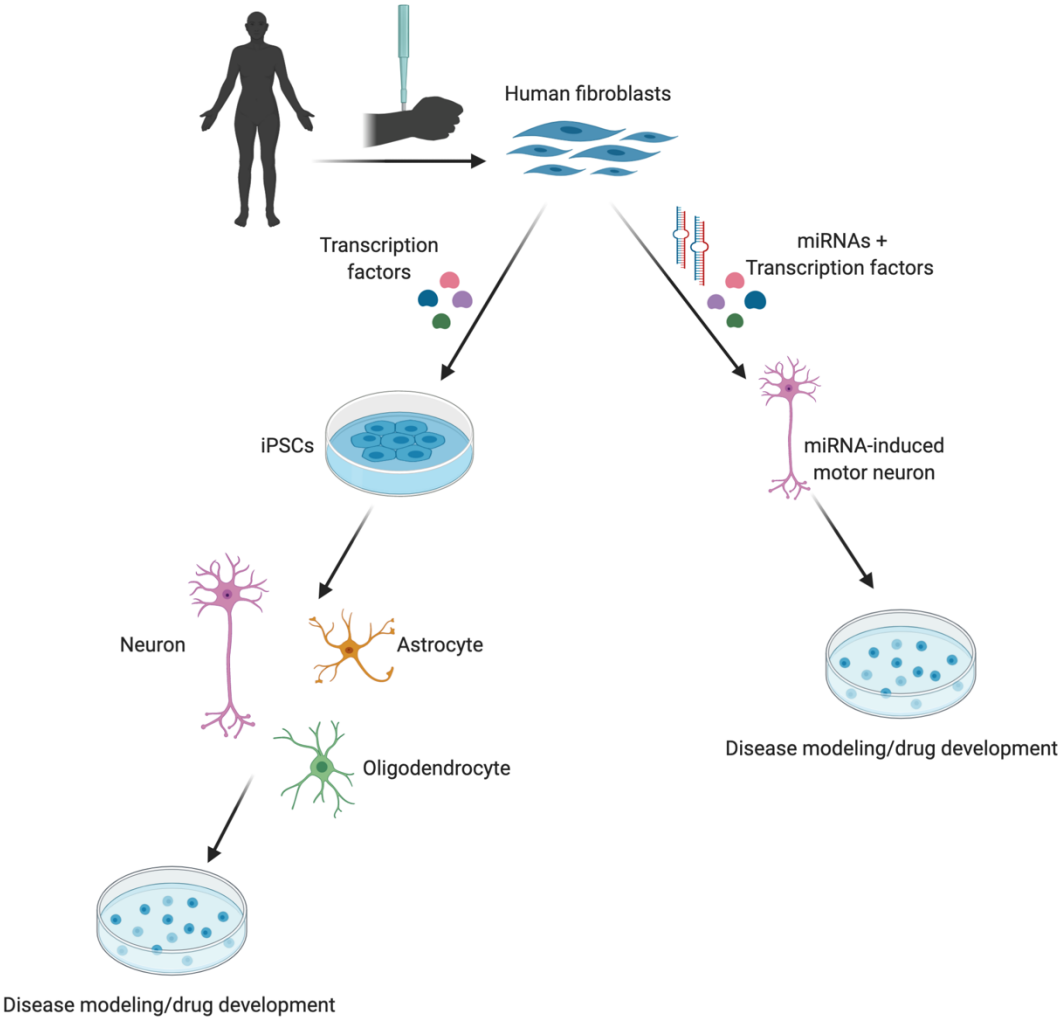

Fig. 2. Reprogramming of adult human fibroblasts into neurons. By adding transcription factors, fibroblasts can be converted into iPSCs, which can then be differentiated into subtypes of neurons or other cell types like astrocytes or oligodendrocytes. Alternatively, fibroblasts can be directly converted with miRNAs and neural lineage-specific transcription factors into a subtype-specific neuron, thus circumventing the stem cell stage. (Figure is made with BioRender.)

1.3 Modeling intrinsic properties of the CNS *in vitro*

The central nervous system (CNS) is an extremely complex, interconnected network combining functional segregation of local specialized neuronal groups with functional integration of brain activity at the global level[59]. It consists of billions of neurons forming trillions of synaptic connections, surrounded by supporting glial cells and other non-neuronal cells. These are embedded in an intricate microenvironment of macromolecules providing structural and biochemical support. As such, there are many inherent challenges associated with modeling a complex system like the brain because such systems cannot be fully understood by only investigating its individual parts[60]. Nevertheless, there are two fundamental characteristics of the CNS that can be recapitulated *in vitro*, namely the

structural and functional self-organization of the network and the emergent network activity. Developing neurons are genetically programmed to extend neurites and search for post-synaptic targets to establish connections, a behavior that is crucial for network formation and which occurs without external sensory inputs[61]. The wiring of the network is accompanied by emergent spontaneous activity, which along with the development and refinement of the network becomes increasingly complex and coordinated[62].

The spontaneous activity in cell populations can be measured with electrophysiological techniques both intracellularly and extracellularly[63]. Extracellular recordings measure the electric fields generated by the movement of ions across the cell membrane following an AP and can be used to measure the activity of many cells simultaneously and reveal network behavior. Microelectrode arrays (MEAs) are most commonly used to record neural network activity *in vitro*. An MEA consist of a cell culture chamber with an array of microelectrodes embedded in an insulating surface. Each electrode measures voltage or current with respect to a common reference electrode, allowing for detection of APs within the measurable area of an electrode[63]. MEAs thus allow measurement of the dynamics in the global network activity by recording spikes, i.e. voltage deflections from the background noise that are presumed to correspond to action potentials, and bursts of synchronized activity. Furthermore, MEAs can be coupled with microfluidic devices, enabling the generation of structured neural networks and measurement of their corresponding activity[64,65]. This makes it possible to exert greater control over the structural organization of the network, and enables the study of self-organization and axon guidance mechanisms[66]. It also holds great potential as a disease model due to the possibility of co-culturing different cell populations in neighboring chambers, providing the opportunity to study how pathology propagates between cells. Taken together, although reductionistic, the combination of different *in vitro* techniques enables the modeling of relatively complex neural networks, and the study of structure-function relationships in healthy and perturbed states.

1.4 Neural plasticity

Neural plasticity is the brain's ability to change its structure and function in response to intrinsic or extrinsic stimuli[67]. It is essential for proper wiring of the brain and refinement of neural circuitry during development. Furthermore, the ability to adapt and modify connections is crucial for the incorporation of new information during life and as such constitutes the basis for learning and memory formation[67]. Neural plasticity can be observed at multiple levels, and spans from structural changes in individual neurons to remapping of entire circuits and functional areas[68]. Plasticity involves several processes, of which the most central ones include Hebbian plasticity, i.e. the strengthening and weakening of synaptic connections *via* long-term potentiation (LTP) and long-term depression (LTD), respectively, and homeostatic plasticity which regulates these modifications and maintains stability in the network activity[69,70]. Plasticity mechanisms remain active throughout life and are crucial for adapting to minor structural and neurochemical changes[68]. Yet, there are major limitations for regeneration in the adult CNS compared to the developing brain. The capacity for generating new neurons is severely restricted in the adult CNS, with the exceptions of the subventricular zone (SVZ) of the lateral ventricles and the subgranular zone (SGZ) of the dentate gyrus in the hippocampus[71]. Furthermore, in contrast to the peripheral nervous system (PNS) where functional recovery can often occur, inhibitory factors in the extracellular environment such

as Nogo and the failure to recruit transcription factors that activate pro-regenerative programs make the CNS particularly sensitive to damage following e.g. spinal cord injury or stroke[72,73].

This also partially accounts for the detrimental effects of neurodegenerative diseases, as neurogenesis cannot compensate for the progressive loss of neurons, and evidence suggest that disease can lead to alterations in the expression of growth factors and guidance molecules making it even more difficult to initiate regeneration of damaged neurons. For example, MNs that are more susceptible to degeneration in ALS express higher levels of Epha4, which regulates synapse formation and can result in cell repulsion, suggesting that high levels of Epha4 inhibits the re-innervating capacity of MNs[74,75]. Moreover, Sema3A is involved in axon repulsion and can lead to cell death, and its expression appears to be upregulated in UMNs and downregulated in LMNs[76]. This could indicate that certain mechanisms promoting regeneration are initiated in response to disease, however, as disease spreads and more and more neurons die, these mechanisms become insufficient or even exaggerated to a point where they become harmful. Indeed, it has been suggested that neurodegeneration is accompanied by endogenous mechanisms involved in regeneration in the early phases of disease, and that therapies should focus on this pre-symptomatic phase, thus preventing disease rather than curing it[77]. However, as patients are either asymptomatic or show very little symptoms in early phases, this requires the identification of biomarkers for early diagnosis.

The consequences of structural alterations will ultimately affect the functionality of the network. Neurons show a specific pattern of synaptic connections with other neurons characterized by high local clustering and fewer long-range connections, and the functionality of a neuronal circuit is partly determined by this pattern[78,79]. Thus, the structural connectivity constrains how the functional interactions within the network can occur[78]. The functional connections are therefore vulnerable to changes in the underlying structure. Structural perturbations can thus disrupt the communication between groups of neurons, and without sufficient homeostatic regulations, these disruptions can change the activity patterns within the network[80]. Alterations in neuronal activity may underlie the cognitive changes observed in psychiatric and neurological disorders[81]. Increased excitatory and decreased inhibitory synaptic activity have been observed in iPSCs from AD patients compared to controls, and hyperexcitability is as discussed above a common feature in ALS[82]. Thus, altered neuronal activity might be an early sign of dysfunction and degeneration in the brain, and is easily detectable with electrophysiological techniques such as MEAs, magnetoencephalography (MEG) and electroencephalography (EEG). Accordingly, electrophysiological measurements are potential diagnostic tools that can be used in the clinic, but abnormalities in activity patterns must be identified first.

1.5 Modeling ALS from a network perspective

The characteristic pattern of high local clustering and few long-range connections in the brain is believed to optimize information processing by segregating information about important stimulus features into specialized neuronal groups and integrating this information across large distances *via* the long-range pathways[83]. This interaction between distinct cell populations results in spatiotemporal correlations of activity within and between cortical areas, generating dynamic patterns of synchronized activity[83]. The processes underlying such dynamics are elusive, but it is hypothesized that the brain

operates close to a so-called "critical point"[84]. Originally a concept from physics, the concept of criticality is used to describe the behavior of systems characterized by different phases, e.g. solid, liquid and gaseous phases. When a system reaches the phase transition between two different types of behavior, the system is said to be in the critical state[84]. It is believed that dynamical systems self-organize into a critical state without the need for external tuning[85]. This self-organized criticality (SoC) in neural networks is characterized by neuronal avalanches, i.e. sequences of bursts of spontaneous activity spreading across the network, with a size distribution described by power laws (Fig. 3)[84,86,87]. These neuronal avalanches can be measured, and some evidence for criticality has been found in cell cultures, animals and humans[88]. Nevertheless, due to the complex dynamics of neural networks it is disputable whether true criticality can exist in the brain[84]. It is instead argued that the brain operates within a critical-like region, where it retains many properties of criticality but is not critical *per se*[89].

As the critical state is in a phase transition, it separates a highly ordered state (the *subcritical* state) from a disordered state (the *supercritical* state)[84]. The subcritical state is too rigid and unable to adapt to changes whereas the supercritical state is too chaotic for efficient communication[88]. The critical state, in contrast, is perfectly balanced between the two and is robust enough to withstand perturbations while also remaining flexible enough to adapt to changing conditions. Therefore, it is believed that SoC optimizes memory capacity and information processing[84]. Yet, a central question concerns what significance the criticality hypothesis has for disease. It is reasonable to assume that larger alterations in the dynamical network activity can lead to divergences in the critical state. Deviations from criticality are for example seen during epileptic seizures where the seizure is characterized by hyper synchronized activity resembling a supercritical state[90]. The hyperexcitability observed in ALS and AD patients could also lead to increased random activity characteristic of the supercritical state, and the progressive loss of connections in neurodegenerative diseases will ultimately affect the underlying structure and dynamics. Deviations from criticality likely also affect the functionality of the network, resulting in impaired information capabilities[90]. Consequently, a better understanding of criticality-like properties in the healthy brain could help identifying disease-related deviations from the critical state.

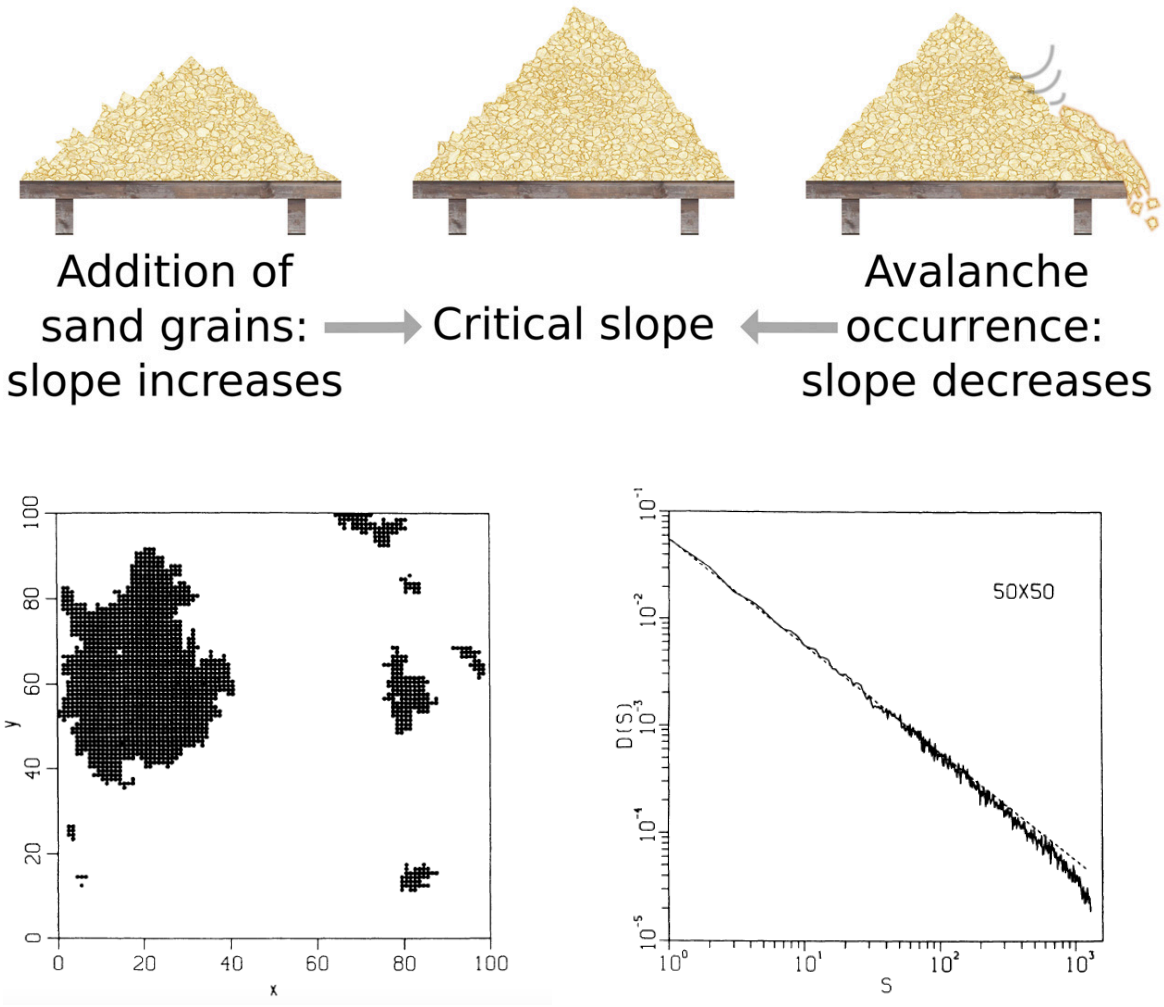

Fig. 3. The sandpile model. A) The sandpile model was introduced by Bak, Tang and Wiesenfeld in their seminal paper from 1987. By randomly placing additional grains onto a pile of sand, the slope will increase, and the pile eventually reaches a specific threshold where some grains will start to slide down the slope of the pile and trigger an avalanche. Following an avalanche, the steepness of the slope decreases. In the long run, the average slope will reach a critical state, where the addition of a single grain of sand can settle on the pile, but also has the potential to trigger a large avalanche. Thus, the system is very sensitive to stimuli but still maintains a certain degree of stability which enables it to evolve into the critical state. A neuronal avalanche occurs in the same way, where a single perturbation can trigger activity that increases in size by spreading throughout large parts of the network. **B)** The sandpile model is a cellular automaton. Such models consist of cells on a grid that evolves in discrete time steps according to a set of rules based on the states of the neighboring cells. The dark cells represent the sizes of avalanches induced by several local perturbations for a 100x100 array. These vary in sizes from a single cell to cells extending across large parts of the system. Thus, the size of a perturbation cannot be predicted, and adding a single grain of sand may cause nothing to happen, or it can trigger a huge avalanche. **C)** By locally perturbing the model several times, the average distribution of avalanche sizes displays a power-law behavior, here shown by the distribution of cluster sizes in a two-dimensional 50x50 array, averaged over 200 samples. The dashed line is a straight line with slope -1.0. (Figures from ref. 84 (**A**) and ref. 85 (**B** and **C**).)

Over the last decades there has been an increased interest in trying to understand the organization of the brain from a graph theoretical perspective, where clusters of neurons are represented by nodes and their connections are represented by links in a graph[60]. With this graph as a base, various analyses can be conducted to reveal information about its underlying network topology. Increasing evidence suggest that the connection topology in the brain is at an intermediate point between that of completely random and completely regular networks, a feature characteristic of a small-world network organization[78,91–93]. The small-world phenomenon originates from social networks, and is characterized by high local clustering and short path lengths between any given pair of nodes that globally connects the entire network (Fig. 4)[78,91,92]. Due to the few long-range connections in the brain, all nodes can therefore communicate *via* a few intermediate steps[78]. This organization is believed to support both segregated and integrated information processing, while also minimizing wiring costs[92]. However, the small-world topology also has implications for the spread of disease. As discussed above, the long-range connections in the brain make it possible for pathogenic proteins to spread from an initial starting point to distant sites. Furthermore, the consequences of damage or disease to a specific region depends on the connection topology of that region[38,39,94]. Damage or disease spreads more profoundly when affecting so-called *connector hubs*, i.e. nodes with a high number of connections to other nodes across different neuronal structures[39]. Thus, the extent of disease spread, and the accompanying functional deficits are determined by the underlying network topology. This could explain why ALS spreads in such an aggressive manner, as connector hubs might be affected early on and thus propagate disease to many areas fast, whereas more slowly progressing neurodegenerative diseases like AD and PD might be constrained to local circuits for a long time.

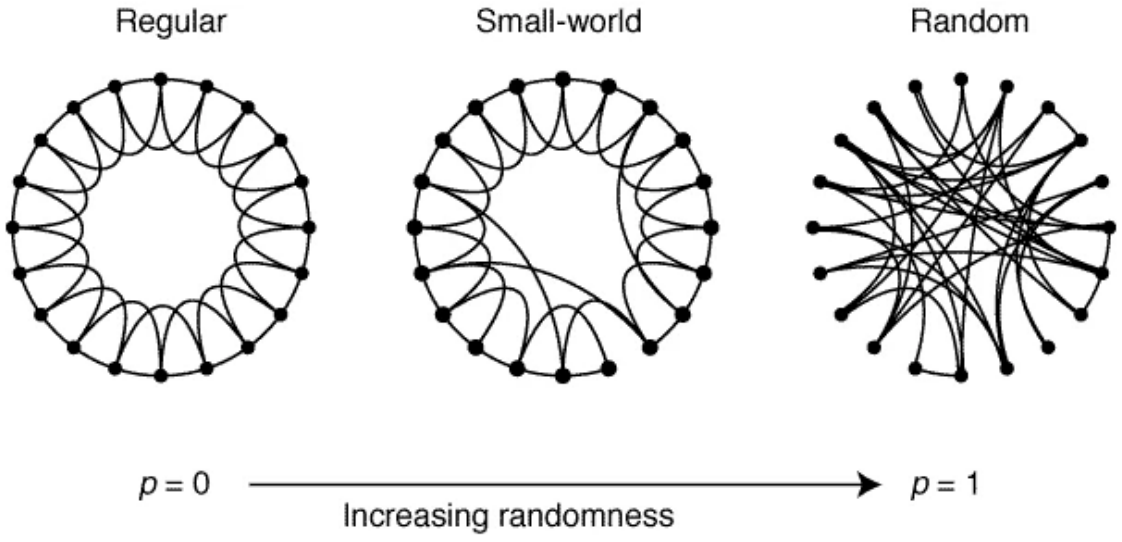

Fig. 4. Representation of a regular, small-world and random network. This model was proposed by Watts and Strogatz in 1998. For intermediate values of *p*, the graph produces a small-world network, which is highly clustered like the regular graph to the left, but also has short average path lengths like the random graph to the right. This facilitates communication between all nodes in the network *via* a few intermediate steps. (Figure from ref. 91.)

Taken together, *in vitro* techniques make it possible to model the structural and functional development of both random and structured neural networks. iPSC technology and directly reprogrammed cells make patient-derived cells more readily available, which enable the development of *in vitro*-based disease models that cannot only recapitulate disease-related aspects, but also network-related concepts such as SoC and small-worldness. Investigating ALS from a network perspective can give insights into how the underlying structure-function relationships shape the spread and effects of disease. Understanding the intrinsic properties of neural networks in both healthy and diseased states potentially enables the prediction of the CNS' responses to perturbations, which can be highly valuable for the development of therapies for neurodegenerative disease, psychiatric disease, stroke and other brain injuries.

Aims and objectives

Based on the above, the purpose of this master's thesis was to develop a multi-nodal *in vitro* model for the recapitulation of neural network behavior and disease progression in ALS, using directly reprogrammed patient-derived fibroblasts. This model is based on a three-well microfluidic chip developed by previous members of the Sandvig group. Recent results from other work in our lab using directly reprogrammed ALS-patient specific fibroblasts have demonstrated that these cells become fully mature neurons and show spontaneous activity. Thus, the next step is to investigate whether disease-related phenotypes remain intact and whether these spread *via* axonal projections to healthy neurons. The project was divided into three main objectives:

1. Proof of concept for the spread of perturbation between connected chambers in microfluidic devices despite fluidic isolation, using rat cortical neurons.

2. Examine the differences in behaviour of healthy and ALS patient-derived motor neurons from iPSCs on MEAs and induce hypoxia to investigate whether the cell types respond differently to perturbations.

3. Co-culture ALS patient-derived motor neurons with healthy motor neurons from directly reprogrammed fibroblasts in separate microfluidic wells and examine the adjacent chambers for signs of spread of altered activity.

Methods

3.1 Experiment 1: Proof of concept

Multi-nodal neural networks were established using 3-well microfluidic chips fabricated at the NTNU Nanolab. The microfluidic chip allows for generation of structured neural networks that can be integrated with MEAs enabling extracellular recordings of the electrophysiological activity in the networks[95]. Furthermore, it enables targeted perturbation of both somata and axons. The microfluidic chip consists of three open cell compartments connected with microtunnels (Fig. 5). The open cell compartments make the wells readily accessible for coating, seeding and media changes, as well as immunocytochemistry and other staining procedures. The chip also has a synaptic channel perpendicular to the tunnels, which enables observation of synaptic contacts from the side, and can be used for axotomy experiments[65]. The material used for the microfluidic chips is polydimethylsiloxane (PDMS). The microfluidic chips are attached to either glass coverslips or MEAs. For additional details on the fabrication of the chips, see ref. 95.

The cell compartments have a diameter of 4 mm and are connected by 52 microtunnels (10 µm in width, 5 µm in height and 500 µm in length). The synaptic channel used for observation of synaptic contacts is 50 µm in width and 45 µm in height and crosses the microtunnels at a distance of about 100 µm from the central node. The MEA that the microfluidic chip is mounted on is a custom-made MEA which consists of 59 recording electrodes and one internal reference electrode. The electrodes are made of titanium nitrate and have a diameter of 100 µm and are separated by 700 µm. The surface area of the electrodes is 2532 μm^2. The electrodes are aligned under the chambers, with some electrodes located around the active zone of each node and under the tunnels. As the microfluidic chips are hand-made there might be some deviations from this alignment. The placement of the electrodes enables recording of the electrophysiological activity from neurons in the nodes, as well as from axon bundles between the nodes.

The electrophysiological activity is recorded with the MEA2100 recording system (Multi Channel Systems), which consists of a headstage and an interface board connecting the headstage to the computer. The headstage has a built-in amplifier, analog-to-digital converter, temperature controller and an integrated stimulus generator. The software package Multi Channel Suite consists of three programs: Multi Channel Experimenter for online data acquisition in real-time, Multi Channel Analyzer for offline data analysis, and Multi Channel DataManager for data export to third-party programs, e.g. Matlab or Python.

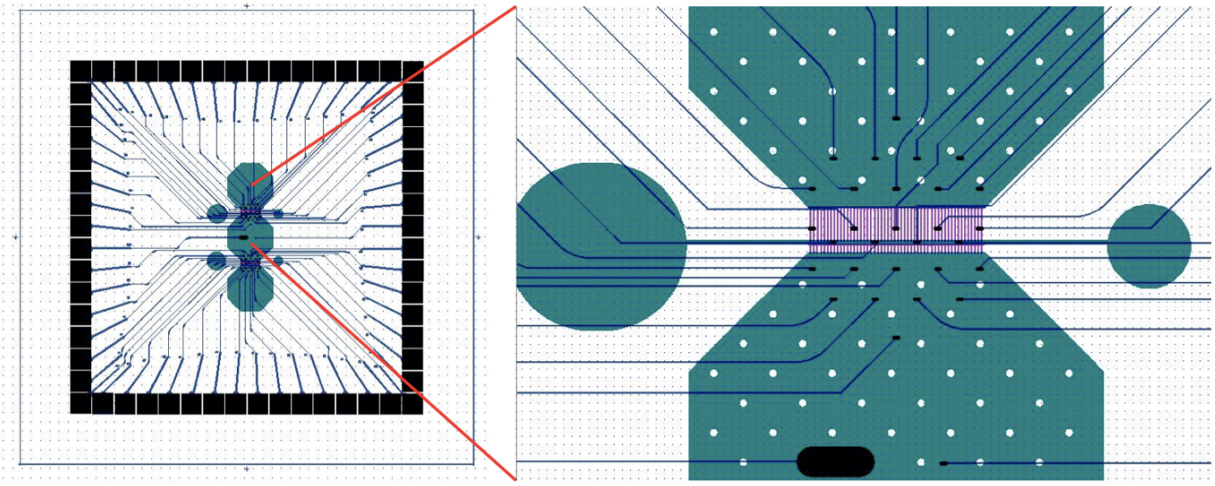

Fig. 5. Design of the three-nodal microfluidic chip with MEA interface. The design includes axonal/dendritic tunnels and axotomy channels which can be seen crossing the tunnels perpendicularly. To the right is the electrode layout in the area between the top and middle well. The reference electrode can be seen in the middle well on the left side (black). (Figure is made with the CAD software Clewin 4 and published with permission from Nicolai Winter-Hjelm.)

3.1.1 Impedance testing, sterilization and coating of microfluidics

Impedance was measured using the MEA IT program (Multi Channel Systems) to check if the electrodes were intact and ready for recording. To measure impedance, the microfluidic culture chamber was filled with phosphate-buffer saline (PBS), which was used as a conductor. An external silver electrode was used as a reference and placed in the PBS solution so that the tip was submerged. After completing the measurement, the PBS was removed, and the microfluidics were washed two times with MQ H_2O. The microfluidics were sterilized by exposure to UV irradiation overnight. All culture vessels were coated with Matrigel diluted in astrocyte medium, made of D-MEM (Thermo Fisher), fetal bovine serum (FBS; Thermo Fisher) and penicillin/streptomycin (Pen-Strep; Thermo Fisher). Each chamber on the microfluidic chip was coated with approximately 50 µL. Additionally, one 8-well ibidi chip (ibidi; 80841) used for immunocytochemistry assays was coated with 250 µL/well. All culture vessels were left in the fridge for half an hour, and then in room temperature for half an hour.

3.1.2 *In vitro* neural networks

Astrocytes at passage number 4 were cultured at an approximate density of 5000 per microfluidic chip and 5000 per ibidi in a D-MEM high glucose high pyruvate media (Thermo Fisher). The media was supplemented with 15 % FBS and 1% Pen-Strep (ca. 50 µL/microfluidic chip, 400 µL/ibidi). After two days in vitro (DIV) the astrocyte media was removed, and rat cortical neurons (passage number 2) were cultured on top of the astrocytes in Neurobasal Plus media supplemented with 1% GlutaMax (Thermo Fisher), and 2% B-27 (Thermo Fisher) and Pen-Strep. 50 000 neurons were cultured on each microfluidic chip (equally divided between each chamber), and on each ibidi well.

The cells were retrieved from the liquid nitrogen tank (-196ºC) and thawed in a 37º liquid water bath until almost fully thawed (about two minutes). In the laminar flow hood, the

cells were transferred dropwise from the vial to a 15 mL conical tube containing 5 mL of prewarmed media. The cells were centrifuged at 200 x g for 5 minutes. Afterward, the supernatant was removed, and the cells were resuspended in 1 mL of media. The total number of cells was determined in suspension via an automated cell counter. Cells were maintained in neuronal media and half of the media was replaced every 2-3 days. To avoid evaporation all microfluidics were placed in a petri dish with a water bath and wrapped in parafilm, and stored in the incubator (37ºC, 5% CO2).

3.1.3 Electrophysiological recordings

A teflon membrane cap was fitted onto the microfluidic chip to prevent exposure to air while recording. A 3-minute lapse was allowed before the start of recording to compensate for any initial noise as a result of movement of the cultures. Each recording lasted 15 minutes. The Multi-Channel experimenter enables electrophysiological data to be acquired in real-time at a sampling rate of 10,000 kHz. The electrophysiological activity was processed by a built-in Butterworth filter with a high pass cutoff at 300-3000 Hz to obtain the spikes at each electrode. The amplitude threshold for spike detection was set at 5.0 standard deviations above the threshold and -5.0 below the threshold. The system records the field potential from the 59 electrodes simultaneously and the program has a Spike Detector for raw data visualization which generate a unique rising and falling threshold for each electrode dependent on the level of background noise. The first recording was made at 11 DIV, and subsequently three times a week until 28 DIV.

3.1.4 Excitatory stimulation with NMDA

At 28 DIV the neural networks in the microfluidic chips were stimulated with N-Methyl-D-aspartate (NMDA; Sigma-Aldrich). Baseline activity was recorded for 15 minutes prior to stimulation. 25 µM of NMDA were added to the top chamber only for 30 minutes. The middle chamber was topped up with media to create a flow barrier between the stimulated chamber and the non-stimulated chambers to ensure that the NMDA was confined to the top chamber only. Immediately after adding the NMDA, the activity was recorded for 15 minutes. The networks were left to rest for 15 minutes after recording, before doing two full media changes to remove all the NMDA. The activity in the networks was monitored every day after the stimulation for four days (see Fig. 6 for a summary of procedures for Experiment 1).

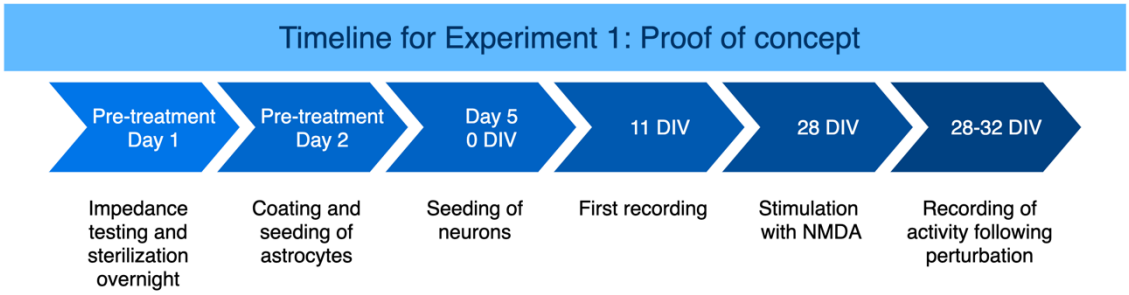

Fig. 6. Simplified timeline of culturing procedures and recordings. The above timeline illustrates the process from pre-treatment of microfluidic chips, coating, culturing of neurons, start of recordings and timepoint for chemical perturbation of the networks. Day refers to the day from the start of the experiment including pre-treatment procedures, whereas DIV (days in vitro) refers to the day since seeding of neurons.

3.1.5 Immunocytochemistry and imaging

At 32 DIV the cells on the ibidi were fixed and used for immunocytochemistry (ICC) assays to confirm cell identity. All cell media were removed, and the cells were washed with 200 µL of PBS. The PBS was removed, and the cells were fixed with 200 µL 4% paraformaldehyde (PFA; Sigma-Aldrich) for 25 minutes at room temperature. The wells were subsequently washed three times with PBS for ten minutes each. A blocking solution was made of PBS, 5% Goat serum (Sigma-Aldrich) and 0.3% Triton-X (Sigma-Aldrich), and 200 µL of this were added to the wells for two hours at room temperature. An antibody solution was made by diluting 1% goat serum and 0.1% Triton-X in PBS and adding the primary antibodies to this. The following antibodies were used: heavy neurofilament (ab8135, 1:1000), NMDA receptor 2B (ab28373, 1:100), GFAP (ab4674, 1:1000) and synaptophysin (ab8099, 1:50). After removing the blocking solution from the wells, 200 µL of the primary antibody solution were added to each well, and the cells were left in the fridge (4 ºC) overnight. On the next day the wells were washed 3 times with PBS. A secondary antibody solution was made in the same way as the primary antibody solution. The secondaries used were anti-mouse 647, anti-rabbit 546 and anti-chicken 488, all at dilution 1:1000. 200 µL of the secondary solution were added to each well and they were left for two hours at room temperature in the dark. 200 µL of Hoechst (bisBenzimide H 33342 trihydrochloride, 14533, Sigma-Aldrich, 1:5000) for nuclear staining were added to each well for 5 minutes towards the end. Subsequently, the cells were washed with PBS three times for 15 minutes each. The silicone chambers of the ibidi were removed and the remaining glass slide was dipped in water. Excess water was removed using Kimtech wipes. Eight small drops of Fluoroshield Mounting Medium (abcam) were added to each slide, one to each cell culture, and a coverslip was carefully placed on top. The slides were left in the fridge overnight. Images were obtained using an EVOS M5000 microscope (Invitrogen Thermo Fisher Scientific) with DAPI (AMEP4650), CY5 (AMEP4656), GFP (AMEP4651) and TxRed (AMEP4655) LED light cubes. All images were processed using Fiji, an open source image processing program distributed by ImageJ.

3.1.6 Data Analysis

In the Multi Channel DataManager program, the files were converted to Nexon system file format (NEX) and uploaded *via* Neuroexplorer 5 (Nex Technologies) to Matlab R2019b (The MathWorks Inc.). Filtering and spike detection were done with a custom-made Matlab script developed by members of the Sandvig group. The spikes recorded at each electrode were ordered according to chamber and tunnels. The mean firing rate (MFR) was estimated for each microfluidic chip for all days of recording, including baseline, during stimulation and after stimulation. To obtain the MFR, the sum of all spikes generated on all electrodes during a recording were divided by the total length of the recording, which generated a mean of spikes/minute for each electrode. This was summed and divided by all electrodes (i.e. 59) to generate an average MFR for all electrodes in the same recording. Correlation was calculated using Pearson's correlation coefficient r. The total network correlation was calculated for each chip for all days of recording. Heatmaps of cross correlations were used to visualize spike correlation within the chambers on the same chip.

3.2 Experiment 2: Hypoxia

Neural networks were established using Axion Biosystems Cytoview 48-well MEA plates. These MEAs contain 16 electrodes arranged in a 4 x 4 grid in each of the conical shaped wells (M768-tMEA-48B). The plate has a transparent well bottom for visualization and assay multiplexing, and built-in humidity chambers. Each well has an internal diameter of 5.30 mm at the bottom and 10.35 mm at the top, and a height of 12.15 mm. The PEDOT electrodes have a 50 µm diameter and are separated by 350 µm. The wells also have a reference electrode that does not record and is placed around the edge of the well bottom. Cells are grown on top of the electrodes on a SU-8 insulation layer. Each of the electrodes are capable of recording or stimulation, which enables recording of the electrophysiological activity of the cells on top of or within the vicinity of 1.1 x 1.1 mm of the electrodes, as well as stimulation of all or selected electrodes. The MEA plates are delivered in sterile packaging that can be opened directly in the laminar flow hood. A sterilization protocol is therefore not necessary before starting experiments.

The Maestro Pro recording system can be used for extracellular recordings from the 48-well MEA plates. The system has BioCore V4 processor chip technology, a built-in chamber that controls heat and CO_2 levels across the plate and an onboard status update screen. This allows for fairly long recordings as heat and CO_2 levels can be held stable over time. Axion's Integrated Studio Software (AxIS) Navigator records and displays electrophysiological activity in real-time, and the AxIS Stimulaton Studio allows electrical or optical stimulation to all or selected electrodes/wells. AxIS also provides integrated tools for offline data analysis, and data export to other programs (e.g. Matlab, Python).

3.2.1 *In vitro* neural networks

Human motor neuron progenitors from Axol Bioscience, derived from a healthy donor (ax0078) and from a patient with confirmed ALS (ax0074, C9orf72 mutation), were plated on two 48-well Cytoview MEA plates, and on two 8-well ibidi chips. Prior to seeding, the plates were coated with polyethyleminine (PEI) and Laminin. 70 µL of PEI diluted in HEPES (both Sigma-Aldrich) to a final concentration of 0.05% were added to each well on the MEA plate, and the ibidi wells were coated with 250 µL. All humidity chambers were filled with distilled water and the plates were sealed with parafilm to prevent evaporation. The plates were left in the incubator (37 ºC, 5% CO_2) overnight. The next day, the PEI solution was removed, and all wells were rinsed four times with distilled water. Then all the water was removed, also from the humidity chambers, and the plates were left in the laminar flow hood to airdry overnight. They were covered with tin foil to avoid exposure to UV light. The next day, all MEA wells were coated with 70 µL of Natural Mouse Laminin (20 µg/mL; Thermo Fisher) diluted in DPBS without calcium and magnesium (Sigma-Aldrich). The humidity chambers were refilled with sterile water and the plates were sealed with parafilm and left in the incubator for 1 hour. All ibidi wells were coated with 250 µL.

Cells were plated immediately after removing the Laminin, without rinsing. Motor neuron progenitors and human astrocytes (Thermo Fisher Gibco K1884, lot 1948466) were thawed, spinned and resuspended separately, and then seeded in mixed suspension, using Axol Motor Neuron Recovery media (ax0071) supplemented with retinoic acid at 0.1 µM and Y-27623 2HCL at 10 µM according to the Axol's recommendations. 25 000 neurons and 2,500 astrocytes were seeded in each MEA well, in a small volume (50 µL) concentrated

within the reference electrodes. Cells were plated in an alternating fashion to avoid placement- or plate-specific effects (see Fig. 7). Each Ibidi-well was seeded with 50 000 motor neuron progenitors and 5 000 human astrocytes in the same media. The MEA plates were sealed with parafilm and left in the incubator for approximately 1 hour to allow cells to attach before adding more media to a final volume of 300 µL. The next day, half of the cell media was replaced with Axol Motor Neuron Recovery media supplemented with retinoic acid, Y-27623 2HCL and 1% Pen-Strep. The day after, half of the media was replaced with Axol Motor Neuron Maintenance media (ax0072) supplemented with 10 ng/mL CNTF, 5 ng/mL BDNF, 0.5 µM retinoic acid and 1% Pen-Strep. Half media changes were performed every other day during the entire maintenance period.

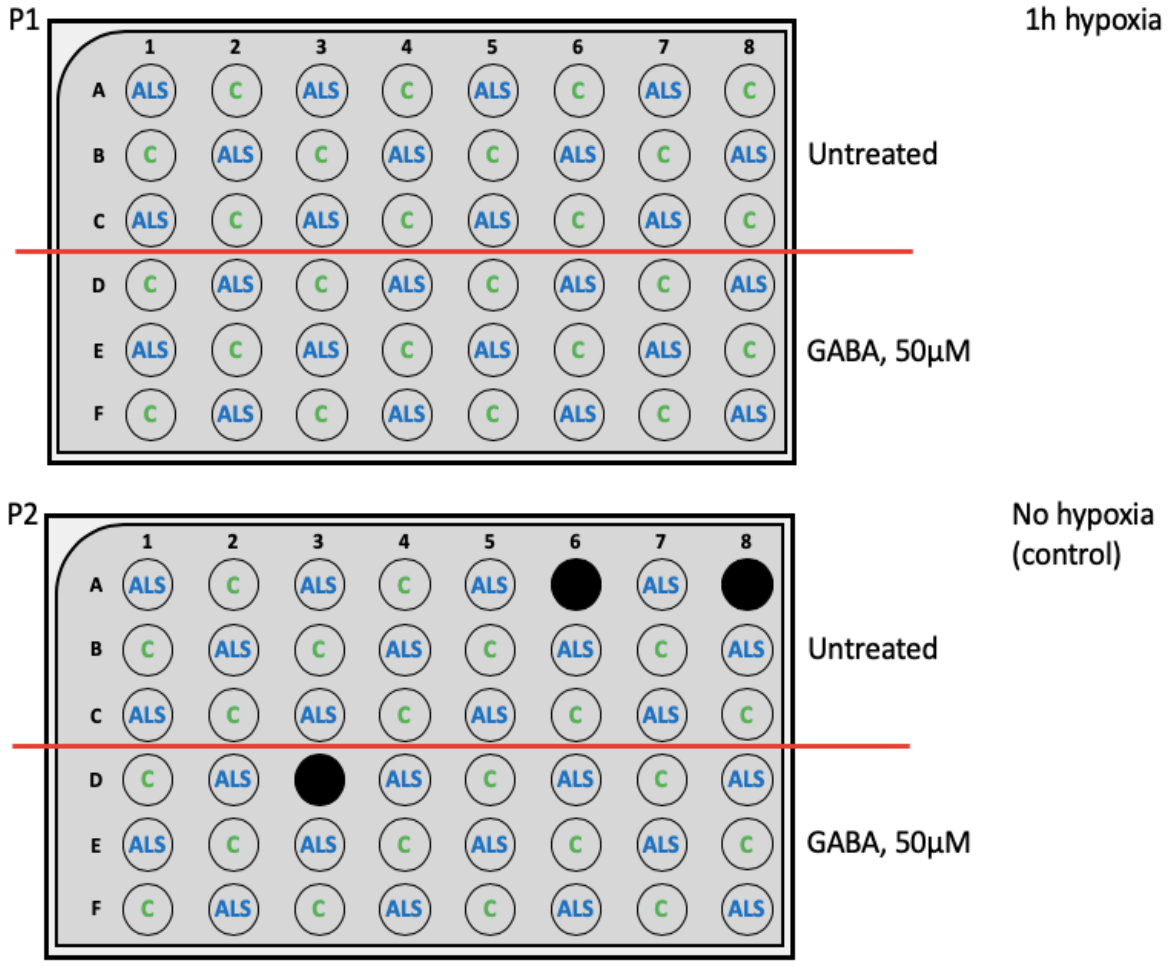

Fig. 7. Illustration of the 48-well MEA plates. The above figure illustrates the alternating seeding pattern for the ALS patient-specific cells and the healthy control cells. The wells on the top plate (P1) were exposed to 1 hour of hypoxia at 54DIV, whereas the wells on the bottom plate (P2) were not. The wells above the red line on both P1 and P2 were treated with 50 µM GABA, and the wells below the red line were untreated during hypoxia or control exposure. Black wells indicate unseeded wells or cells detached. (Figure used with permission from Vegard Fiskum.)

3.2.2 Electrophysiological recordings

For recordings of electrophysiological activity, the MEA plate was placed in the built-in chamber of the Maestro Pro recording system, with temperature of 37^0C and 5% CO_2. After being placed in the Axion Maestro, the neural networks were left for 1 hour to allow the activity to stabilize before recording. Each recording lasted for 1 hour. The first recording was made at culture age 49 DIV and continued every other day until the neural networks reached 53 DIV, and then daily after this. The Axion Maestro Pro identifies spikes by an adaptive threshold detection during recording. The voltage was filtered with a digital bandpass filter (200-3000 Hz), from which an average of the signal voltage was determined. Voltage exceeding the mean ± 7 standard deviations was detected as a spike. Each threshold was determined on an electrode basis. Spike times were exported via Neuroexplorer 5 to Matlab R2019b and analyzed using custom-made scripts (see Data analysis). Due to a technical fault in the acquisition process, the recording of activity at 58 DIV was not stored for the hypoxic plate (data point omitted), and the recording of the non-hypoxic plate only stored 23 minutes of the 1 hour planned recording.

3.2.3 Hypoxia exposure and GABA treatment

At 54 DIV, all networks on one of the plates (ALS = 24, healthy = 24) were exposed to hypoxic conditions. The networks on the other plate were used as controls (ALS = 24, healthy = 21). Within the hypoxic group and the control, half of the neural networks were also treated with GABA prior to hypoxia (1% O_2 and 5% CO_2 for 1 hour). 30 µL of 550µM GABA were added to the 300µL of cell media in each culture for a final GABA concentration of 50µM. Untreated neural networks were supplemented with 30 µL of cell media with no GABA. The experiment had four groups in total: GABA-treated hypoxic ({GABA +, Hypoxia +}, n=24), untreated hypoxic ({GABA -, Hypoxia +}, n=24), GABA-treated control ({GABA +, Hypoxia -}, n=23) and untreated control ({GABA -, Hypoxia -}, n=22). Prior to the experiment, baseline activity was recorded for all neural networks for 1 hour. During exposure to hypoxic conditions, activity for all neural networks was also recorded for 1 hour. After the hypoxia exposure, half media changes were made to all neural networks. After the hypoxia exposure, activity was recorded for 1 hour daily for 10 days, and half of the media was changed every other day. The last recording was made at 64 DIV. Fig. 8 summarizes the procedures for Experiment 2.

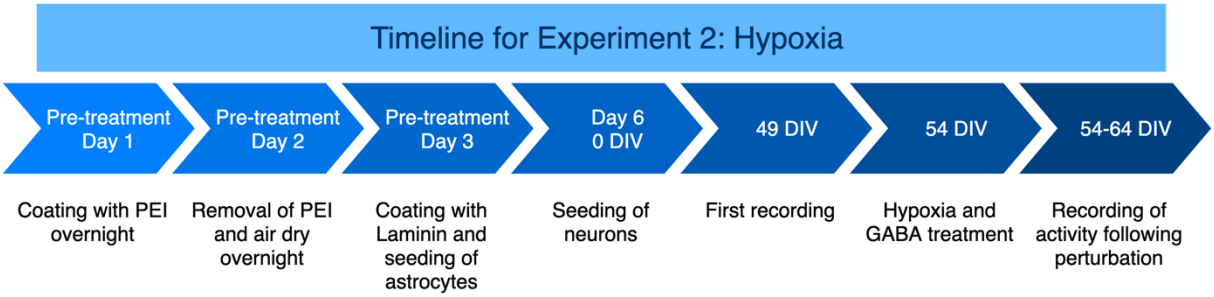

Fig. 8. Simplified timeline of culturing procedures and recordings. The above timeline illustrates the process from pre-treatment of MEAs, coating, culturing of neurons, start of recordings and timepoint for hypoxia. Day refers to the day from the start of the experiment including pre-treatment procedures, whereas DIV (days in vitro) refers to the day since seeding of neurons.

3.2.4 Immunocytochemistry and imaging

The neural networks on the ibidi chips were used for ICC to confirm motor neuron cell identity. The same protocol for ICC as described under Experiment 1 was used, however, 5 % Goat serum and 0.6 % Triton-X was used for blocking, and 2.5 % Goat serum and 0.3 % Triton-X was used for the primary and secondary antibody solutions. The neural networks were tested for expression of Islet1 (ab86472, 1:200), heavy neurofilament (ab4680, 1:1 000), GABA-b receptor 1 (ab55051, 1:100) and glutamate receptors type 2 and 3 (ab27225, 1:500), all with nuclear staining with Hoechst (14533, Sigma-Aldrich, 1:10 000). Images were obtained using an EVOS M5000 microscope, and all images were processed using Fiji.

3.2.5 Data analysis

The data was first sorted into an Excel file labelling all wells as ALS or healthy, hypoxia exposed or not, and GABA treated or not. The same script also identified network bursts, which were identified by examining a binned spike distribution using 50 ms bins. Every bin exceeding a threshold of mean ± 5 standard deviations of firing rate was identified as potentially part of a burst. Due to low activity in the data set, few bursts were identified, especially for the ALS group, and subsequent analyses were therefore based on spiking activity. A spiking threshold for each electrode was set to minimum 5 spikes per minute to avoid distortions in the data set due to low-activity electrodes. Electrodes with fewer than 5 spikes per minute were excluded from further analyses. Based on this criterion, an MFR for each well was calculated. To obtain the MFR, the sum of all spikes generated on all electrodes during a recording were divided by the total length of the recording, which generated a mean of spikes/second for each well. This was averaged within each of the experimental groups.

A coherence index (CI) was also calculated for each experimental group. The CI is defined as the ratio between the standard deviation and the mean of the spontaneous firing rate[96]. The index is a measure for the coordination/synchronicity in the network activity. The CI will be low in networks with little synchrony in activity and increase as the synchrony increases.

3.3 Experiment 3: Direct microRNA-based conversion

The direct conversion protocol used in this experiment is based on the protocol used in the paper by Richner and colleagues[97], and optimizations done by other members of the Sandvig group. The procedure consists of three main steps: transduction of fibroblasts with lentiviruses, re-plating of transduced fibroblasts at post-infection day 5 and culturing in neuronal growth medium for 3-4 weeks. miR-9/9* and miR-124 is used for the neuronal reprogramming as these seem to target genetic pathways involved in antagonizing neuronal cell fates. The exact mechanism of neuronal reprogramming is not yet known but miR-9/9*-124 induces remodeling of the epigenome and reconfigures chromatin accessibilities, thus activating a pan-neuronal program[55]. By adding MN-specific transcription factors, ISL1 and LHX3, the conversion is selectively driven towards a homogenous population of human MNs. The miRNAs are delivered by lentiviruses, produced at the Viral Vector Core Facility at the Kavli Institute for Systems Neuroscience, NTNU.

The protocol combines the expression of miRNAs with the antiapoptotic factor Bcl-xL, which promotes cell survival during conversion. The plasmid (pTight-BCL-9124) in the viruses is activated by doxycycline (Dox). Dox treatment is continued until cells express endogenous miR-9/9*-124 and the neuronal cell fate appears to be stable, which is reported to occur around day 30[97]. Dox treatment can be continued for longer, which might be beneficial if the experiments are going to be run over a long period of time. Dox induction is followed by antibiotic selection, in which Puromycin, Blasticidin and Geneticin is also added to the cultures. This step ensures removal of all non-transduced cells and surviving cells successfully express the miRNAs.

The re-plating process involves moving the transduced fibroblasts from a non-coated six-well plate to poly-L-ornithine (PLO), Laminin and Fibronectin coated substrates, as recommended by Richner and colleagues[97]. This is important to ensure that the converted cells mature in an environment suitable for a neuronal population. Fibroblasts do not attach well to PLO, but neurons do, and re-plating ensures proper adhesion for the cell population both prior to and after conversion. Additionally, there can be impurities in the lentivirus which can affect the health of the cells. These are significantly reduced when re-plating. We will use the same PLO, Laminin and Fibronectin coating in this experiment, however, for the MEAs we will use a combination of PEI and Laminin instead, because this coating is recommended by the manufacturer of the MEA plates (Axion Biosystems). See Fig. 9 for a representation of the direct reprogramming procedure.

3.3.1 Fibroblast expansion

To initiate the conversion, 1 million human fibroblasts were seeded onto two 6-well culture plates at a density of 250 000 cells per well. 500 000 were from an ALS patient with a SOD1 mutation and 500 000 were from a healthy individual. The cells were retrieved from the liquid nitrogen tank (-196 ºC) and thawed in a 37 ºC liquid water bath until almost fully thawed (approximately 3 minutes). In the laminar flow hood, the fibroblasts were transferred from the vial into a 15 mL conical tube containing 6 mL prewarmed Fibroblast Media (FM, see List of media/supplements). The cells were centrifuged at 180 x g for 7 minutes. Afterward, the supernatant was removed, and the cells were resuspended in 1 mL of FM. The total number of cells was determined in suspension *via* an automated cell counter. The cell suspension was diluted to around 100 000 cells per/mL and 3 mL of the suspension were seeded to each well. Only the four outer wells of the 6-well plates were used to avoid balancing problems when centrifuging in later steps. The cells were placed in the incubator (37 ºC, 5% CO_2) until fully confluent. Media changes should be carried out every other day, and as the cells were kept for three days before becoming fully confluent, a full media change was done two days after seeding.

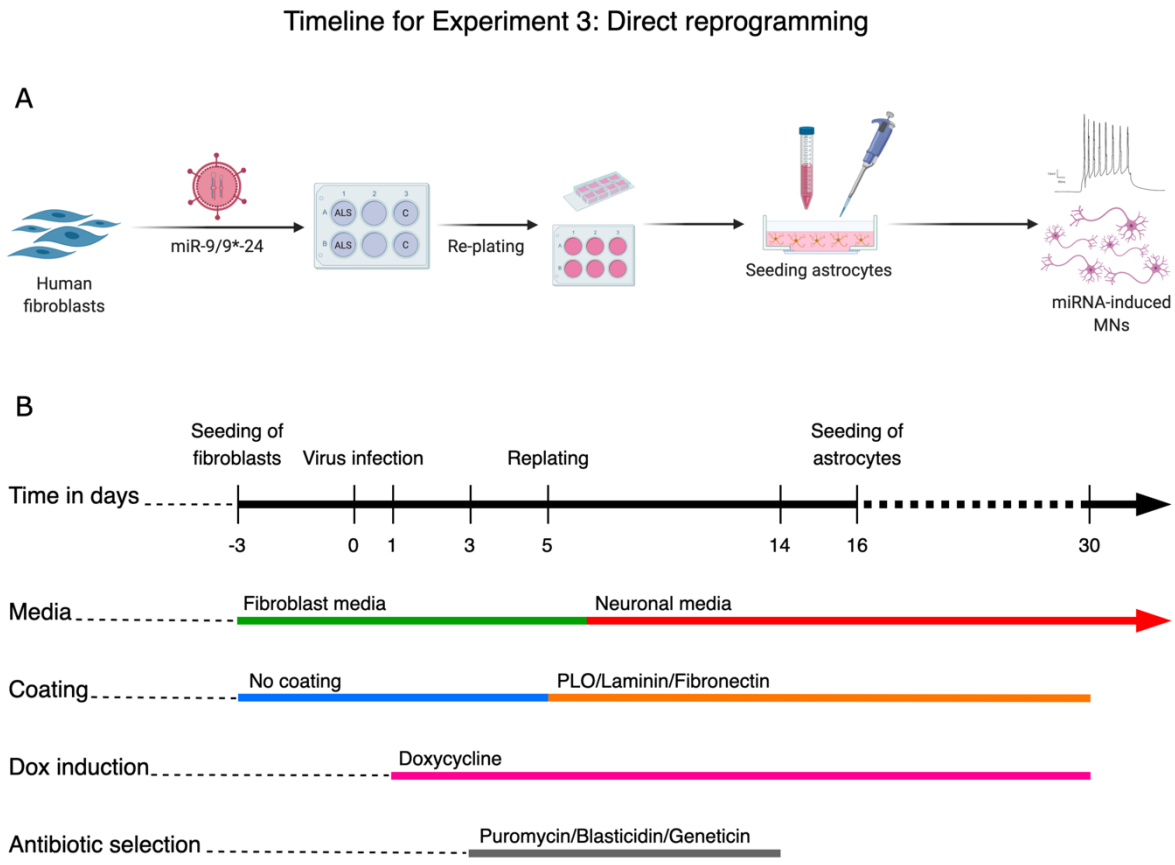

Fig. 9. Timeline of direct conversion of human fibroblasts to motor neurons. This timeline shows the reprogramming protocol from the seeding of fibroblasts (day -3), to virus infection (day 0) and re-plating, up until 30 days post-infection, when the cells should be fully mature and electrically active. B) includes changes in culturing medium and coating of surfaces, as well as start and end points for Dox induction and antibiotic selection. (Fig. A is made with BioRender, fig. B adapted from ref. 97.)

3.3.2 Virus infection

Once fully confluent, the cells were transduced with a reprogramming solution of FM, lentivirus and polybrene. Polybrene (Sigma-Aldrich) was added to the FM media to a final concentration of 8 µg/mL. The virus was slowly thawed in the fridge and kept on ice in the laminar flow hood while adding the respective amounts to the FM/polybrene solution (see List of reagents for transduction/transfection). The reprogramming solution was warmed in the 37 ºC liquid water bath. The old media on the plates were aspirated from the fibroblasts before adding the reprogramming solution to each well. The plates were weighed to ensure that they were within 50 mg of each other's weight. Additional prewarmed FM was added to the wells where necessary. The plates were then centrifuged at 1000 x g, 37 ºC for 30 minutes. After spinfection, the plates were carefully moved to the incubator.

3.3.3 Start of doxycycline induction and antibiotic selection

16-18 hours after spinfection, the reprogramming solution was removed, and the wells were washed with 2 mL prewarmed Dulbecco's Phosphate Buffered Saline (DPBS; Sigma-Aldrich) without calcium and magnesium. The sides of the plates were tapped lightly to remove any debris. The DPBS was aspirated, and replaced with 3 mL of fresh, prewarmed FM supplemented with Dox (1µg/mL) to induce expression of pTight-BCL-9124. Two days later, all media was replaced with 3 mL FM supplemented with Dox (1µg/mL), Puromycin (3µg/mL), Blasticidin (5µg/mL) and Geneticin (400µg/ml), initiating the antibiotic selection process.

3.3.4 Re-plating of transduced human fibroblasts

Five days after transduction the cells were re-plated onto MEAs, microfluidics and Ibidis. The media were removed, and each well was washed with 2 mL of warm DPBS, tapping the sides of the plate lightly to remove any debris. The wash was removed and 1 mL of 0.25% Trypsin-EDTA (Thermo Fisher) solution was added to each well. The plates were incubated for 2-3 minutes. The plates were moved around to help detach cells and the wells were inspected in the microscope. Once the cells detached, the Trypsin-EDTA was inactivated with 2 mL of FM supplemented with Dox (1µg/mL). The cells were carefully resuspended in the well before the entire volume was transferred to a 15 mL conical tube. A sample was collected for counting, and the cell count was performed while centrifuging the cells at 200 x g for 5 minutes. After spinning, the supernatant was aspirated, and the cells were resuspended with 1 mL FM supplemented with Dox (1µg/mL). Additional media was added to a final concentration of 1000 cells/µL. The cells were seeded onto pre-coated MEAs, microfluidics and ibidis and allowed to attach for approximately 1 hour in the incubator. When the cells had attached, the appropriate amount of FM supplemented with Dox was added to each well. The cells were stored in the 37 ºC, 5% CO_2 incubator.

3.3.5 Maintenance of reprogrammed neurons

The day after re-plating, the FM with Dox was aspirated and fully supplemented Neuronal Media (NM; see List of media/supplements) was added to each well. Two days after switching to NM, each well was supplemented with 0.5µg/mL Dox. This was repeated every four days from day 8 to day 28. Four days after switching to NM, half of the media was replenished with fully supplemented NM media. On the eighth day after switching to NM, all media was removed from each well and replaced with the same volume of warm, fully supplemented NM without selection antibiotics, but still with 1µg/mL Dox. Half of the media was replaced every four days starting from day 18. From day 30 onward, half media changes without Dox were carried out.

3.3.6 Seeding of astrocytes

Astrocytes were seeded at day 16 after transduction as they would have been killed at earlier stages by the selection antibiotics. After thawing, the astrocytes were transferred from the vial into a 15 mL conical tube containing 10 mL prewarmed non-supplemented NM. The cells were centrifuged at 290 x g for 5 minutes. The supernatant was removed, and the cells were resuspended in 1 mL supplemented NM. The total number of cells was determined in suspension via an automated cell counter. Each cell culture of reprogrammed

neurons was seeded with 10 % astrocytes relative to the number of cells initially seeded when re-plating.

3.3.7 Establishing neural networks on Axion Biosystems MEA plates

Neural networks were established using Axion Biosystems Cytoview 6-well MEA plates. These contain 64 electrodes arranged in an 8 x 8 grid in each of the conical shaped wells (M384-tMEA-6B). The plate has a transparent well bottom for visualization and assay multiplexing, and built-in humidity chambers. Each well has an internal diameter of 11.5 mm at the bottom and 22 mm at the top, and a height of 13.2 mm. The PEDOT electrodes have a 50 µm diameter and are separated by 300 µm. The wells also have a reference electrode placed around the edge of the well bottom. Cells are grown on top of the electrodes on a SU-8 insulation layer. Each of the electrodes are capable of recording or stimulation, which enables recording of the electrophysiological activity of the cells on top of or within the vicinity of 2.1 x 2.1 mm of the electrodes, as well as stimulation of all or selected electrodes. The Maestro Pro recording system was used for extracellular recordings from the 6-well MEA plates.

Coating, seeding and maintenance of cultures

Two 6-well Cytoview MEA plates were used in this experiment (Fig. 10). The MEA plates were coated with PEI and Laminin. 210 µL of PEI diluted in HEPES to a final concentration of 0.05% were added to each well. All humidity chambers were filled with sterile water and the plates were sealed with parafilm to prevent evaporation. The plates were left in the incubator (37 ºC, 5% CO_2) overnight. The next day, the PEI solution was removed, and all wells were washed four times with sterile water. Then all the water was removed, also from the humidity chambers, and the plates were left in the laminar flow hood to dry overnight. They were covered with tin foil to avoid exposure to UV light. The next day, all wells were coated with 210 µL of Natural Mouse Laminin (20 µg/mL) and Fibronectin (0.01%; Sigma-Aldrich) diluted in DPBS without calcium and magnesium. The humidity chambers were refilled with sterile water and the plates were sealed with parafilm and left in the incubator for 1 hour.

When seeding the directly converted cells, the Laminin was removed, and the cells were seeded directly without washing. 50 000 cells were seeded in each well, in a small volume (50 µL) concentrated within the reference electrodes. ALS patient-specific cells were seeded in three of the wells on each plate and healthy cells were seeded in the remaining three wells in an alternating fashion to avoid placement-or plate-specific effects. The plates were sealed with parafilm and the cells were left to attach in the incubator for approximately 1 hour. Then, the wells were filled with FM to a final volume of 1 mL, before being put back into the incubator. When switching to NM all FM was removed and 1 mL of NM was added to each well. Two days later, 5000 astrocytes were added to each well, seeding them dropwise directly into the media. The cultures were maintained with half media changes and Dox supplementation as described above (see Maintenance of reprogrammed neurons).

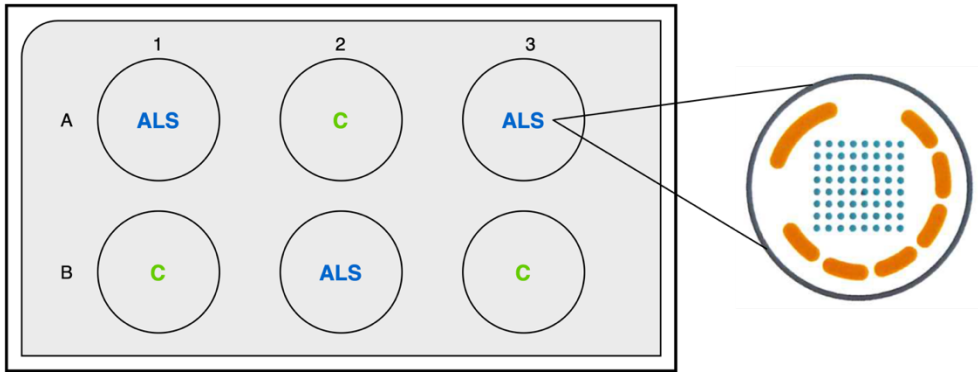

Fig. 10. Illustration of 6-well MEA plate. This figure shows the alternating pattern of ALS-patient specific cells and healthy control cells on the 6-well MEA plate. To the right is an overview of the organization of the electrodes (blue) and reference electrodes (orange) at the well bottom (from Cytoview MEA 6 Datasheet, Axion Biosystems).

3.3.8 Establishing multi-nodal neural networks on microfluidic devices with and without MEA interface

Multi-nodal neural networks were established using 3-well microfluidic chips fabricated at the NTNU Nanolab (see Experiment 1 for further details on the microfluidic chips). Eight 3-well microfluidic devices were used for this experiment, four with MEA interface and four without. The cell compartments in the standard microfluidic chips (Ø 3 mm) are connected by 52 microtunnels (30 µm in width, 5 µm in height and 300 µm in length). The cell compartments in the microfluidics with MEA interface are identical to the chips described in Experiment 1. The MEA2100 recording system (Multi Channel Systems) was used for recordings.

Coating, seeding and maintenance

Prior to coating, all microfluidics were sterilized under UV light in the laminar flow hood for 30 minutes. Each microfluidic chip was coated with 0.01 % PLO (Sigma-Aldrich), filling the outer wells to the top and 2/3 of the middle well in order to force the coating into the channels through hydrostatic pressure. They were placed in a petri dish which was sealed with parafilm to prevent evaporation and left in the incubator for two hours. The wells were subsequently washed three times with sterile water for 30 minutes each time. Afterward, the chips were coated with Laminin and Fibronectin, which were diluted in Leibovitz L-15 medium (Sigma-Aldrich) and supplemented with Sodium Bicarbonate (Sigma-Aldrich; 1:60 Natural Mouse Laminin, 1:40 Sodium Bicarbonate and 0.01 % Fibronectin) and left in the fridge (4 ºC) overnight.

The next day, the Laminin/Fibronectin coating was removed prior to seeding. 25 000 cells were seeded per well. ALS-patient specific cells were seeded in one of the peripheral wells and healthy cells in the other two (Fig. 11). The cells were left to attach in the incubator for approximately 1 hour before filling up the wells with FM. On the following day, all the FM was removed, and fully supplemented NM was added to the wells. Two days later, 2500 astrocytes were added to each well, seeding them dropwise directly into the media. The

cultures were maintained with half media changes and Dox supplementation as described above (see *Maintenance of reprogrammed neurons*).

3.3.9 Extracellular recording and immunocytochemistry assays

Recordings of the neural networks on the MEA plate and microfluidic chips were made at 30 DIV. No activity was evident at this stage, and thus the cultures were terminated. The ibidis were fixed on the same day but due to low cell density ICC was not performed.

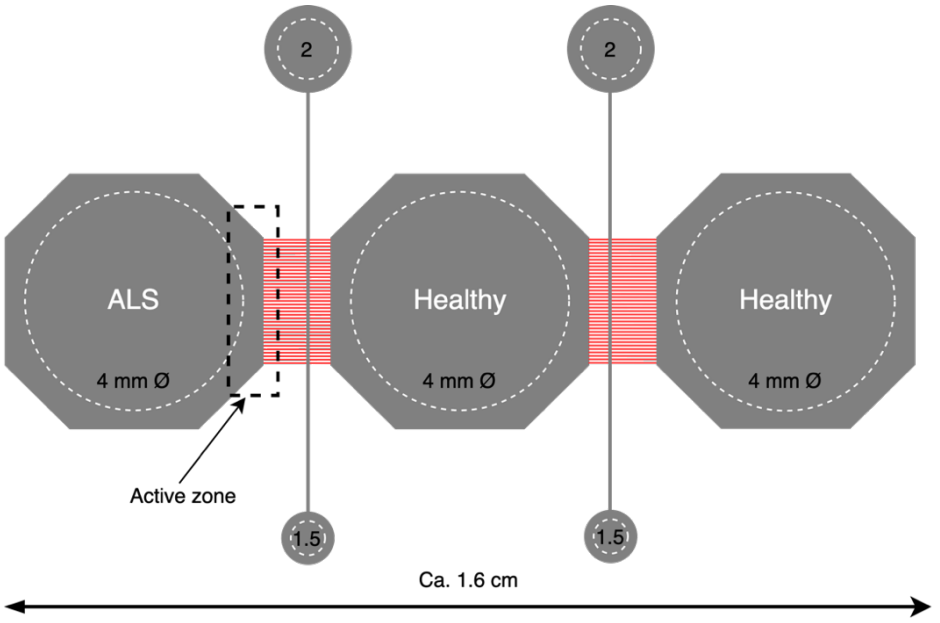

Fig. 11. Illustration of microfluidic chips. This illustration shows the design of the 3-well microfluidic chip and the seeding pattern of cells in Experiment 3 (ALS-healthy-healthy). The grey octagons represent the PDMS and the white perforated lines mark the punched-out areas that constitute the three open cell compartments. The red lines connecting the cell compartments are the tunnels, and the grey lines crossing the tunnels are the synaptic channels. The active zone is marked by the black perforated rectangle and represents the area between the end of the well and beginning of the tunnels. Cells migrate to this area before starting to grow axons into the tunnels. (Figure adapted from ref. 65.)

3.3.10 List of media and supplements for direct conversion:

Fibroblast media (50 mL, store at 4 ºC and use within 1 month):

40 ml	D-MEM, high glucose (Thermo Fisher)
7.5 ml	FBS (Thermo Fisher)
500 µL	MEM NEAA (Thermo Fisher)
500 µL	Sodium Pyruvate (Thermo Fisher)
500 µL	GlutaMAX (Thermo Fisher)
500 µL	Pen/Strep (Thermo Fisher)
500 µL	HEPES (Sigma-Aldrich)
5 µL	β-mercaptoethanol (Thermo Fisher)

Neuronal Base Media (100 mL):

98 mL	Neuronal Media (ScienCell, #1521)
1 mL	Neuronal Growth Supplement (ScienCell, #1562)
1 mL	Pen/Strep (ScienCell, #0503)

10 mL of Neuronal Base Media are supplemented with:

80 µL	Geneticin (400µg/mL; Sigma-Aldrich)
5 µL	Blasticidin (5µg/mL; Thermo Fisher)
3 µL	Puromycin (1µg/mL; Thermo Fisher)
1 µL	Doxycycline (1µg/ml; Thermo Fisher)
50 µL	Valproic Acid (Merck Millipore)
20 µL	DB cAMP (Sigma-Aldrich)
10 µL	ATRA (Sigma-Aldrich)
5 µL	BDNF (20µg/ml; PeproTech)
5 µL	CNTF (20µg/ml; PeproTech)
5 µL	GDNF (20µg/ml; PeproTech)
5 µL	NT-3 (20µg/ml; PeproTech)

Reagents for transduction/transfection:

2.5 million infectious units (IFU) per 100 000 cells were used, which translates to:

Construct	LP Titre/mL	Add to 3mL
BclxL	**2.4×10^{10}**	**35 µl**
hISL1	**1.9×10^{11}**	**10 µl**
hLHX3	**1.1×10^{11}**	**15 µl**
rtTA	**2×10^{10}**	**40 µl**

LP Titre = approximation of the number of lentivirus particles

Results

4.1 Experiment 1: Proof of concept

4.1.1 Development of neural networks on microfluidic chips

The neural networks on the microfluidic chips developed successfully and formed inter-nodal connections via the tunnels (Fig. 12). The density of the neural networks on the ibidi was quite sparse, but ICC assays confirmed the presence of neurons for the cells that were there, by expression of the marker neurofilament heavy which labels mature axons, and synaptophysin which labels pre-synaptic elements (Fig. 13G and 13H). NMDA-receptors were also present (Figure 13C). GFAP which labels astrocytes was also stained for, but this was non-specific (data not shown).

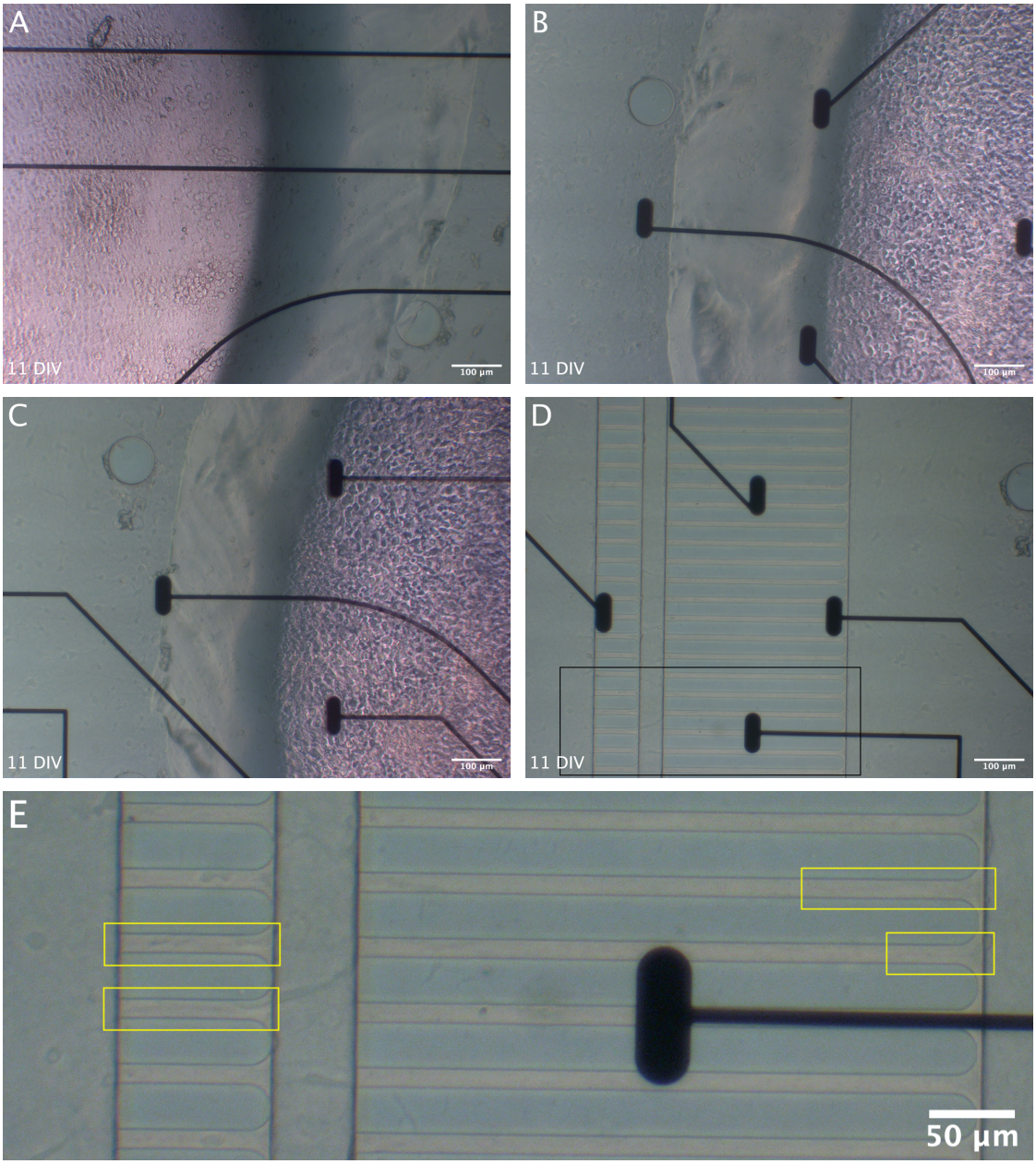

Fig. 12. Phase contrast images of one of the microfluidic chips at 11 DIV. A) Top chamber of the chip. The pink on the left side is the chamber with cells and the grey area on the right side is the active zone. Black lines are electrodes. **B)** Middle chamber of the chip. **C)** Bottom chamber of the chip. **D)** The tunnels between the top and the middle chamber on the chip. **E)** Enlargement of the black rectangle in D. Yellow boxes highlight areas where axons have started growing into the tunnels. All images are taken with a Zeiss microscope using a Zeiss 20x/0.3 NA objective. 100 µm scale bar (A-D) and 50 µm scale bar (E).

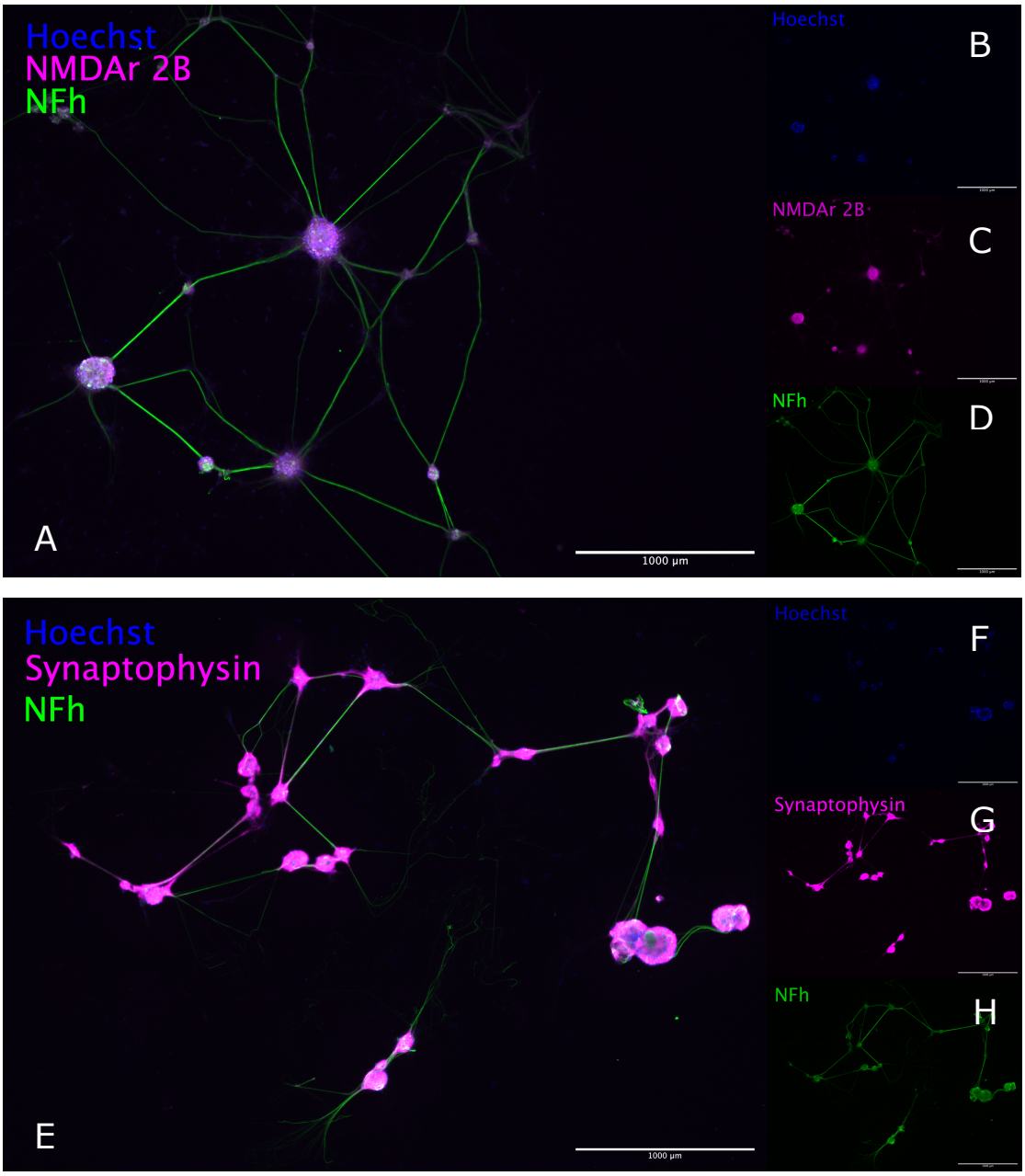

Fig. 13. Neurotypic markers for rat cortical neurons. Following 32 days of maturation, immunocytochemistry confirmed the cell identity of the rat cortical neurons used in Experiment 1 by expression of neurofilament heavy, NMDA-receptor 2B and synaptophysin. 1000 µm scale bars.

4.1.2 Electrophysiological activity of the structured neural networks

Measurement of the electrophysiological activity in the neural networks revealed a trend in the development of the network activity where the MFR increased from 11 DIV up until 23 DIV, at which point the activity appeared to stabilize (Fig. 14A). The increase in MFR developed similarly for the different networks, but for three of them (MIP2, 3 and 4) there was a negative relationship between the MFR and culture age from 19 to 23 DIV. Although the networks developed similarly there were consistent differences in how high the MFR was. MIP1 had a higher firing rate than the other networks throughout the entire recording period, whereas MIP4 had a lower firing rate than the other networks. MIP2 and MIP3 were consistently similar with regards to MFR. The total network correlation was higher for all cultures at the first day of recording (11 DIV) but decreased and remained quite stable from 15 DIV to 28 DIV (Fig. 14B). Again, there were differences between each of the networks, where MIP2 and MIP4 had a higher total network correlation than MIP1 and MIP3. MIP1 and MIP3 also followed each other more closely in total network correlation compared to MIP2 and MIP4.

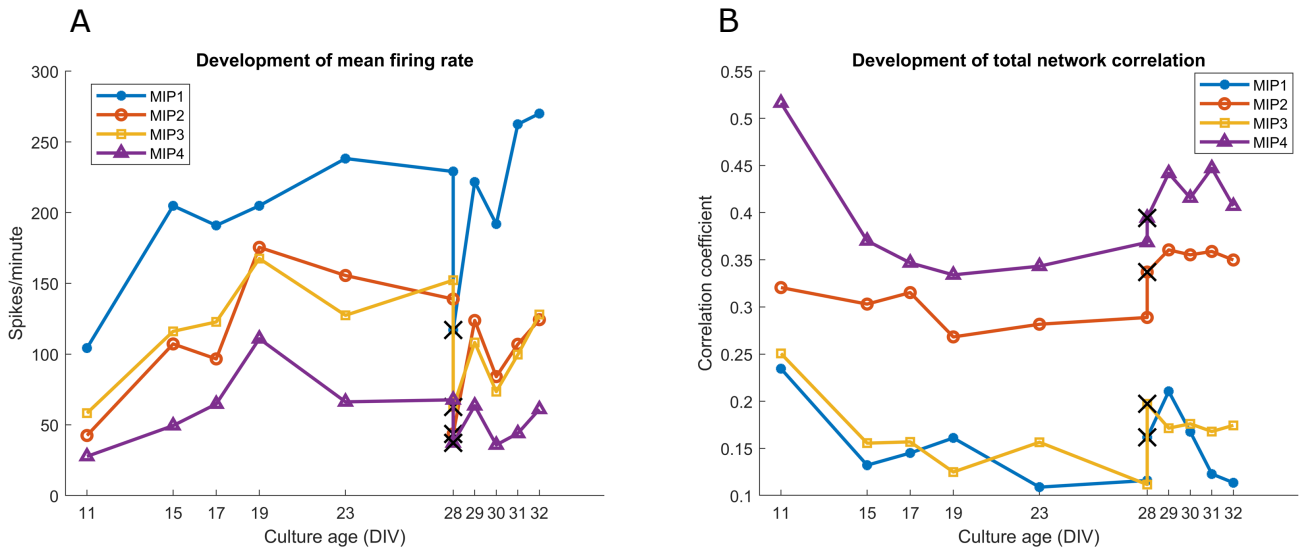

Fig. 14. Mean firing rate (MFR) and total network correlation for the four structured neural networks. A) MFR at different time points during the three weeks of recording. Both a baseline recording and a recording following NMDA stimulation (marked with a black cross) were made at 28 DIV. MIP refers to each of the microfluidic chips. **B)** Total network correlation at different time points, the black cross marks the time point of NMDA stimulation.

Interestingly, there was a clear decrease in MFR for all networks following the addition of NMDA to the top chamber. This was followed by an increase in MFR on the following day (29 DIV), and a decrease on 30 DIV. After this point, the activity increased again for all networks, approaching or passing the same MFR as baseline at 32 DIV. The raster plots illustrate the spiking activity of one structured networks before stimulation (Fig. 15A) and one day after (Fig. 15B). The total network correlation increased for all networks during NMDA stimulation. For MIP2, 3 and 4, the total network correlation remained higher compared to baseline during the rest of the recording period, although there were some variations from day to day. For MIP1, the total network correlation increased the day after stimulation, but then consistently decreased for the rest of the recording period. To assess how the activity in the different chambers was affected by the NMDA stimulation, the MFR for each chamber during the entirety of the recording during stimulation was calculated (Fig. 16). The MFR appeared to be quite synchronized between the different wells, although there were deviations at some time points. For MIP1, 2 and 3, the middle chamber had a consistently higher MFR than the top and bottom chambers. For MIP4, however, the MFR for the middle chamber was lower. The MFR for all the chambers was clearly lower during stimulation compared to baseline (Fig. 17). Based on the MFR only, the top chamber did not appear to be clearly affected by the stimulation. However, images taken during recording of the NMDA-stimulated networks indicated that there was more activity in the top chamber than in the middle and bottom chamber (Fig. 18).

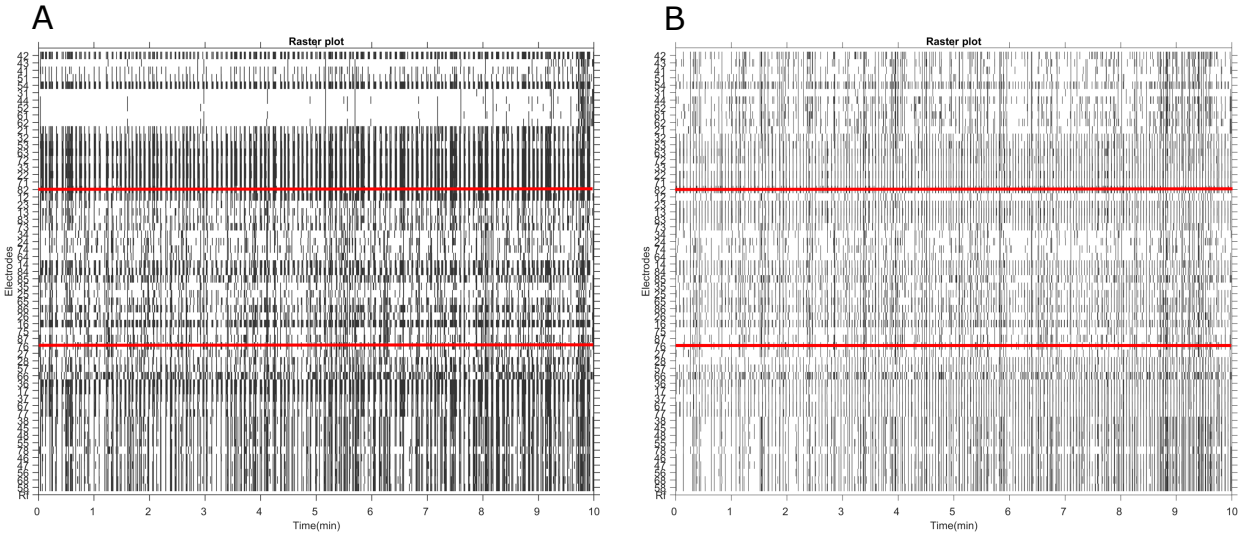

Fig. 15. Example raster plots for one of the microfluidic chips (MIP3). A) Raster plot at baseline (28 DIV). The different electrodes are aligned along the y-axis, and the x-axis shows the time in minutes for ten minutes of the 15-minute recording. The red lines are added to separate the activity for the different chambers. The top part is the top chamber, the middle part is the middle chamber, and the bottom part is the bottom chamber. Each vertical line represents a spike. **B)** Raster plot at 29 DIV, one day after stimulation.

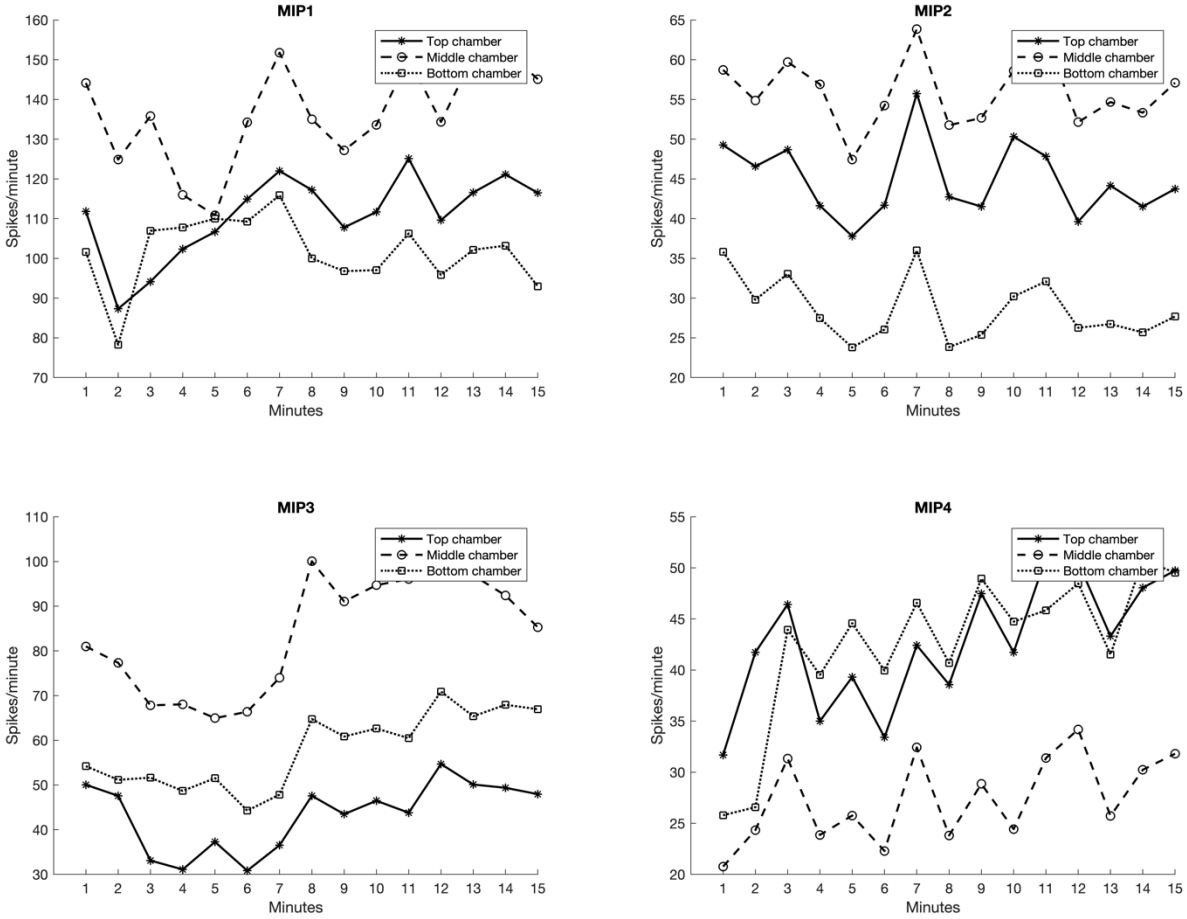

Fig. 16. Mean firing rate per minute for each of the chambers in the different networks for the 15-minute recording during stimulation. The top chamber was treated with NMDA.

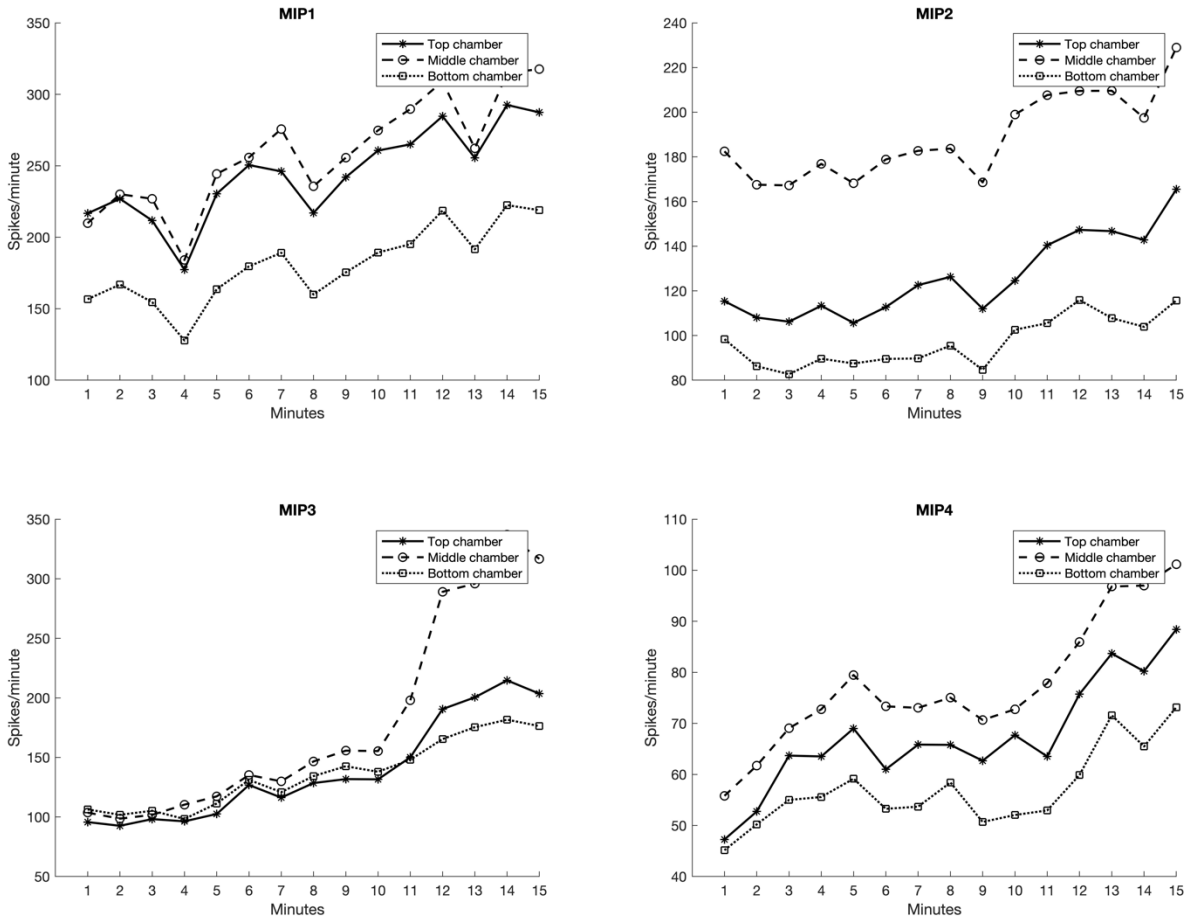

Fig. 17. Mean firing rate per minute for each of the chambers in the different networks for the 15-minute baseline recording prior to stimulation.

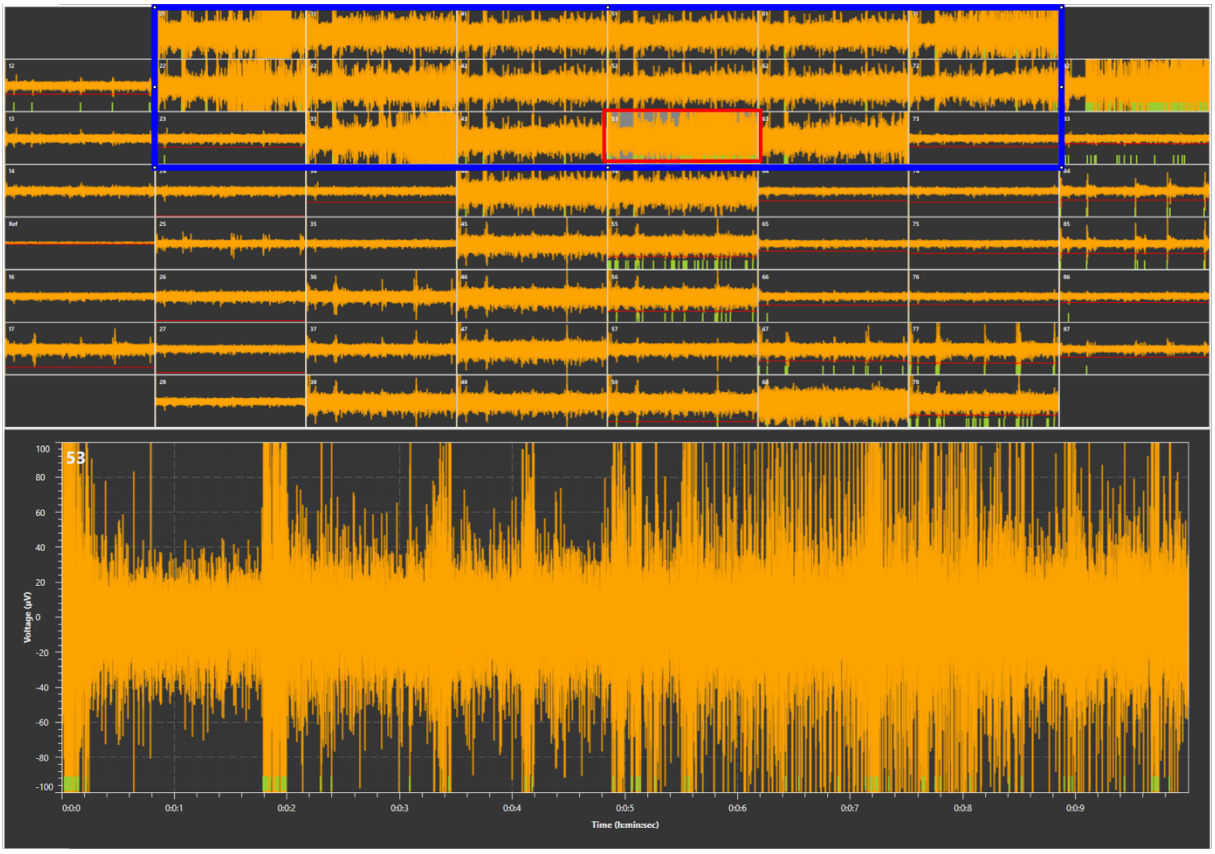

Fig. 18. Image taken during recording of an NMDA-stimulated network. The blue rectangle marks the electrodes located in the top chamber, which received NMDA. At the bottom is an enlargement of the activity recorded at electrode 53, marked with a red rectangle.

Based on the analyses above, two of the structured neural networks were selected for more analysis. MIP1 was selected because it appeared to deviate from the other network in terms of both MFR and change in total network correlation following stimulation. It was compared to MIP3, which was randomly chosen among the other three networks. Cross correlations showed a high within-chamber correlation for the bottom chamber at baseline (28 DIV, before stimulation) for both MIP1 and MIP3 (Fig. 19A and 20A). The correlation between the top and the middle chamber was also higher than the correlation between the top and the bottom chamber for MIP1, at least for some electrodes, although the within-chamber correlation for the top chamber was low. The correlation between the middle and the bottom chamber was higher than between the top and the middle chamber for MIP3. During stimulation, the two networks appeared to have a similar change in correlation. The within-chamber correlation for the top chamber increased for both MIP1 and MIP3 (Fig. 19B and 20B). Furthermore, the between-chamber correlation between the top and the middle chamber increased. Also, the correlation between the middle and bottom chamber appeared to decrease, especially for MIP3. One day after stimulation (29 DIV), the within-chamber correlation for the top chamber seemed to decrease for MIP1 (Fig. 19C). Furthermore, the between-chamber correlation appeared to increase for the top and bottom chamber, and for the middle and bottom chamber. For MIP3, the within-chamber correlation for the top chamber clearly decreased at 29 DIV (Fig. 20C). Additionally, the between-chamber correlation for the top and middle chamber, and for the middle and bottom chamber increased.

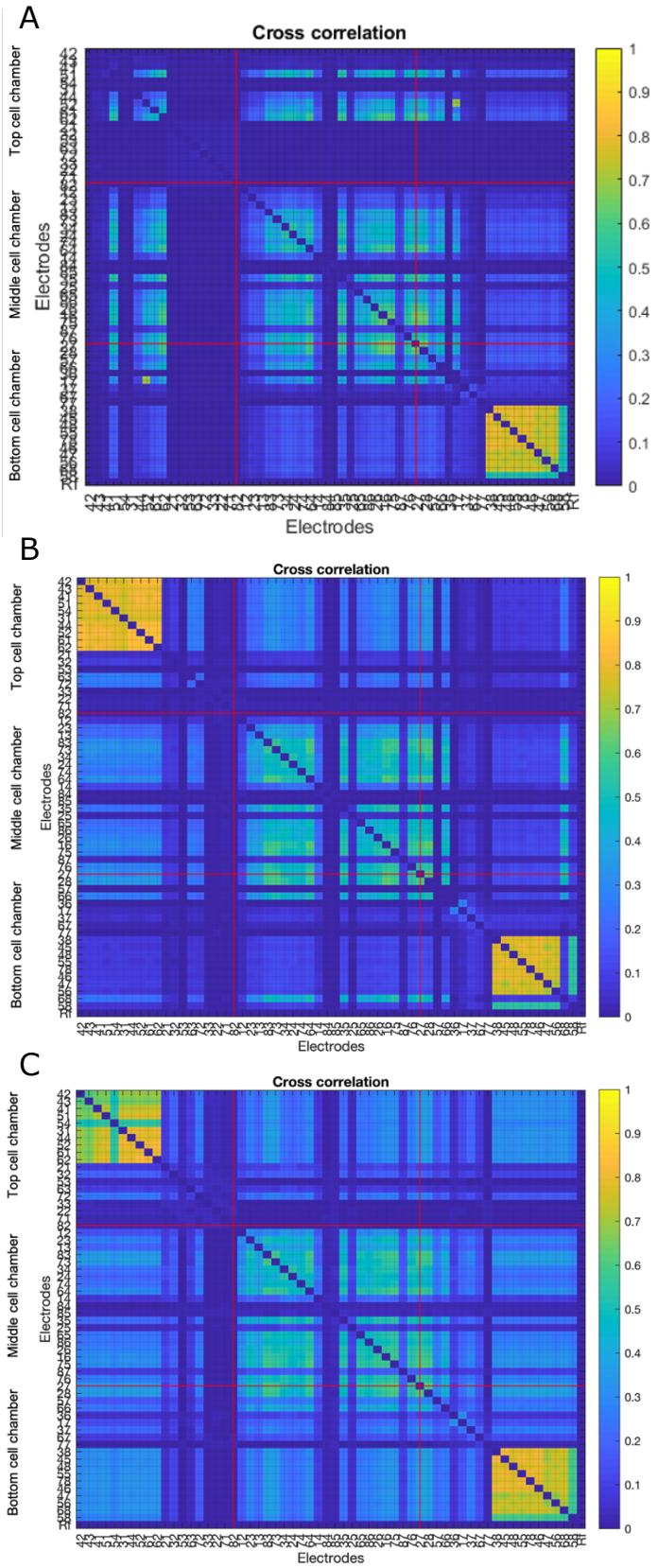

Fig. 19. Heatmaps for cross correlation of electrode activity within and between the different chambers in one of the microfluidic chips. A) Cross correlation for MIP1 at 28 DIV before stimulation. The numbers on the x- and y-axis correspond to the electrode numbers, organized by chamber. The red lines organize the heatmap into grids corresponding to the different chambers, which are labeled on the left side of the y-axis. For the top and bottom chamber, the electrodes located under the tunnels are included within the red grids. **B)** Cross correlation for MIP1 at 28 DIV during stimulation. **C)** Cross correlation for MIP1 at 29 DIV, one day after stimulation.

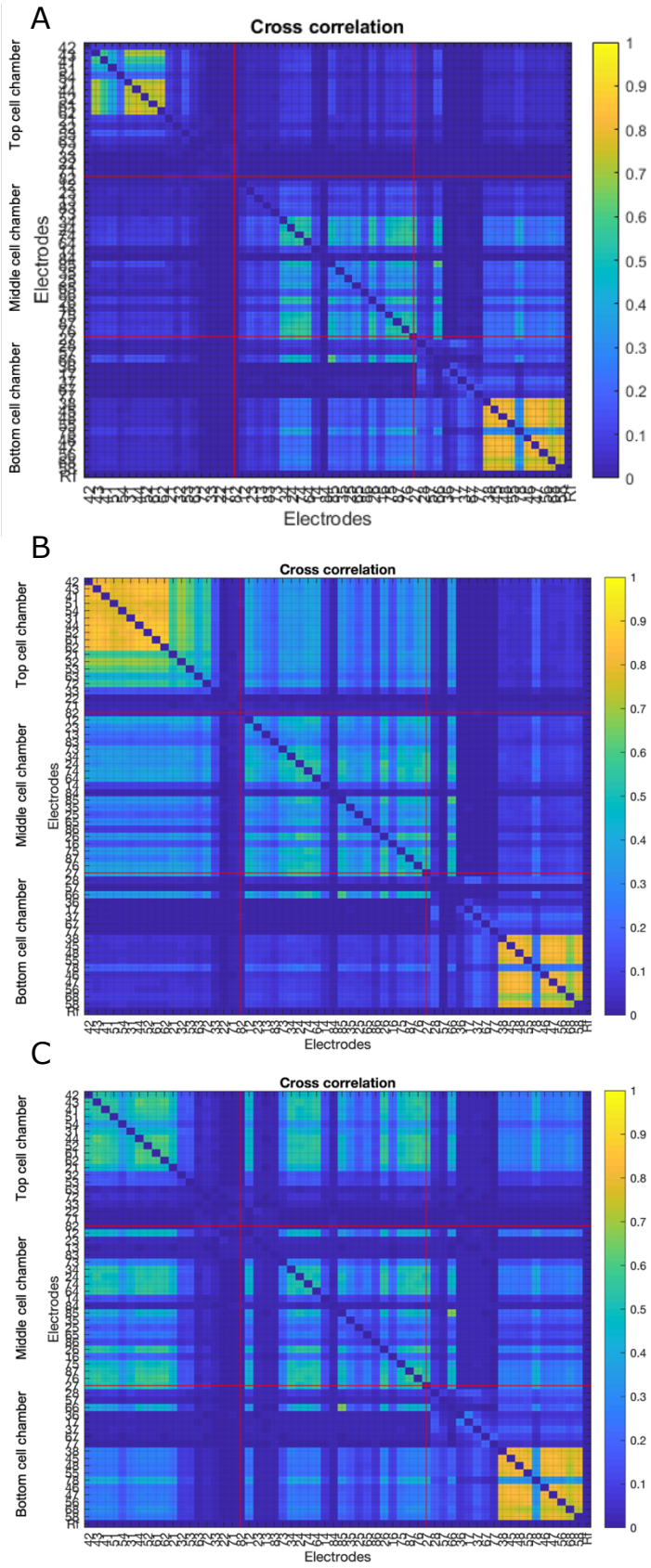

Fig. 20. Heatmaps for cross correlation of electrode activity within and between the different chambers in one of the microfluidic chips. A) Cross correlation for MIP3 at 28 DIV before stimulation. **B)** Cross correlation for MIP3 at 28 DIV during stimulation. **C)** Cross correlation for MIP3 at 29 DIV, one day after stimulation.

4.2 Experiment 2: Hypoxia

4.2.1 Development of neural networks on MEAs

The neural networks on the MEA plates appeared to develop successfully based on phase contrast images (data not shown). The ICC assays confirmed the presence of MNs in the control cells by expression of Islet1 (Fig. 21A-C). GABA-b receptor 1 and ionotropic glutamate receptors type 2 and 3 were also present, as well as neurofilament heavy (Fig. 21 D-H). However, Islet1 was not present in the ALS patient-specific cells (Fig. 22A-C), but GABA-b receptor 1, glutamate receptors type 2 and 3 and neurofilament heavy were (Fig. 22D-H).

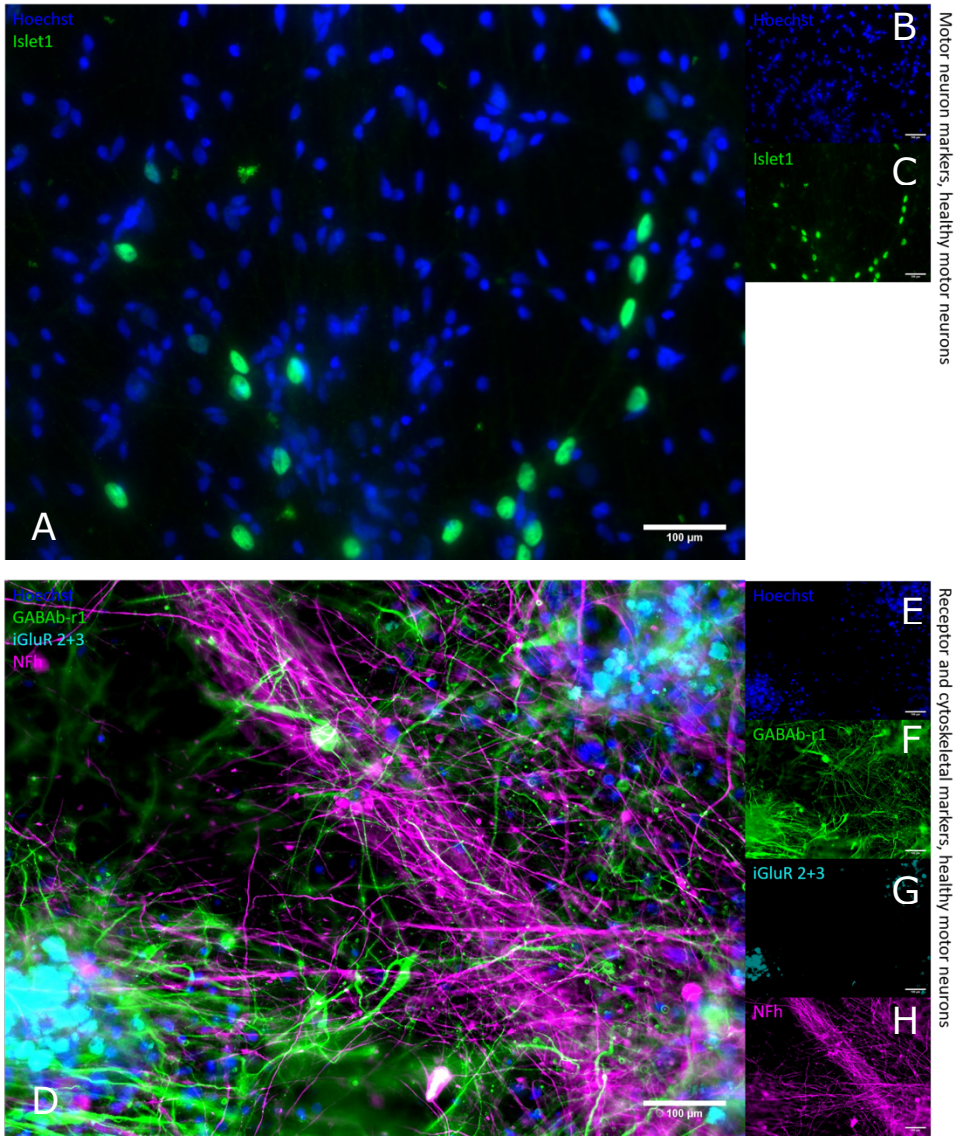

Fig. 21. Expression of neurotypic markers for healthy motor neurons. Following 64 days of maturation, immunocytochemistry confirmed the cell identity of the healthy motor neurons used in Experiment 2 by expression of Islet1, GABAb receptor 1, ionotropic glutamate receptors 2 and 3 and neurofilament heavy.

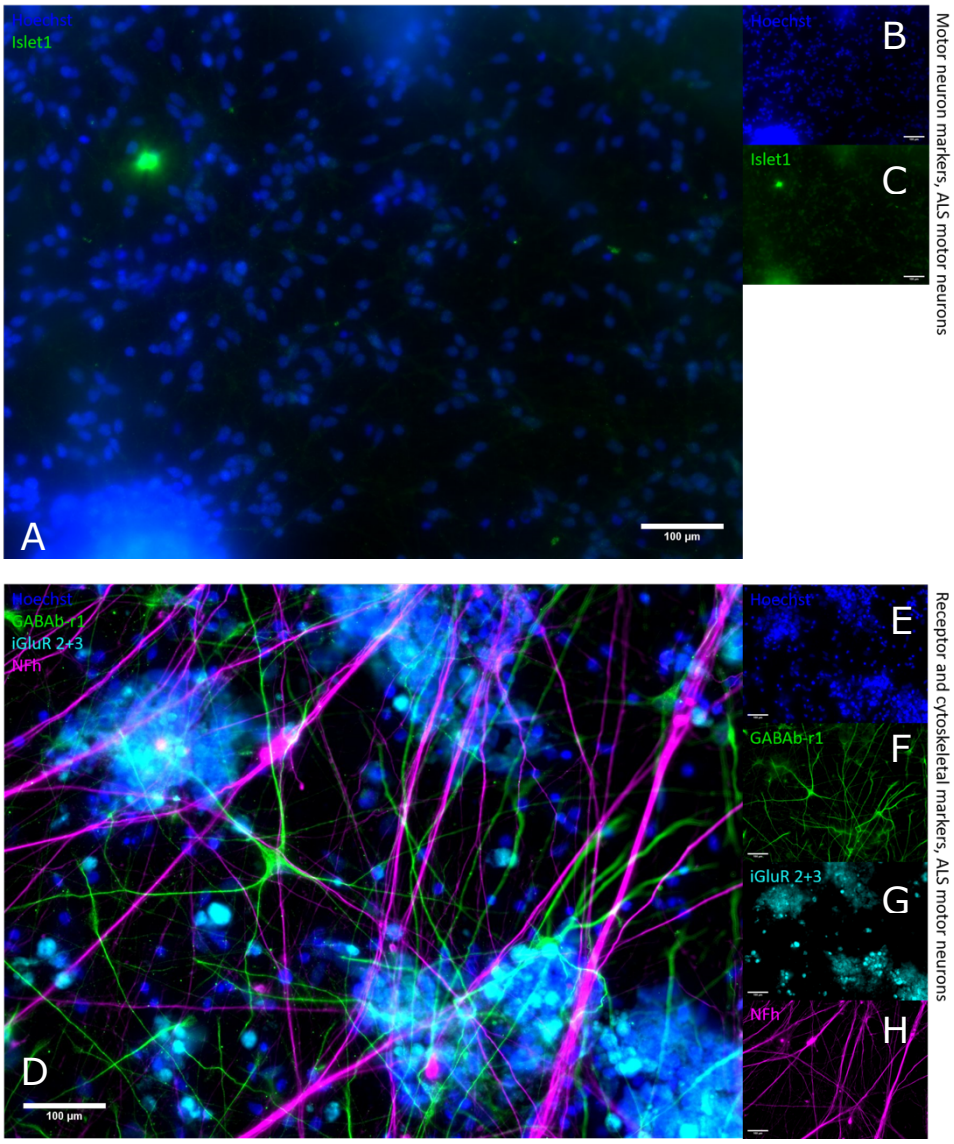

Fig. 22. Expression of neurotypic markers for ALS patient-specific motor neurons. Following 64 days of maturation, immunocytochemistry did not confirm the cell identity of the ALS patient-specific motor neurons used in Experiment 2 as Islet1 was not expressed. GABAb receptor 1, ionotropic glutamate receptors 2 and 3 and neurofilament heavy were expressed but not as strongly as for the healthy motor neurons.

4.2.2 Electrophysiological activity and hypoxia

The MFR for the healthy group remained stable during the recording period before hypoxia. The ALS group was not as active as the controls and did not improve significantly during the course of the experiment. There were large in-group variations in activity, especially for the ALS cells. It should be noted that due to the large variations in activity the presented graphs represent the data after low-activity electrodes have been filtered out (electrodes with less than 5 spikes/minute). Some data points are therefore missing due to low activity in the network. The raster plots shown were among the more active cultures in both groups and are therefore not representative for the entire group (Fig. 23A-B).

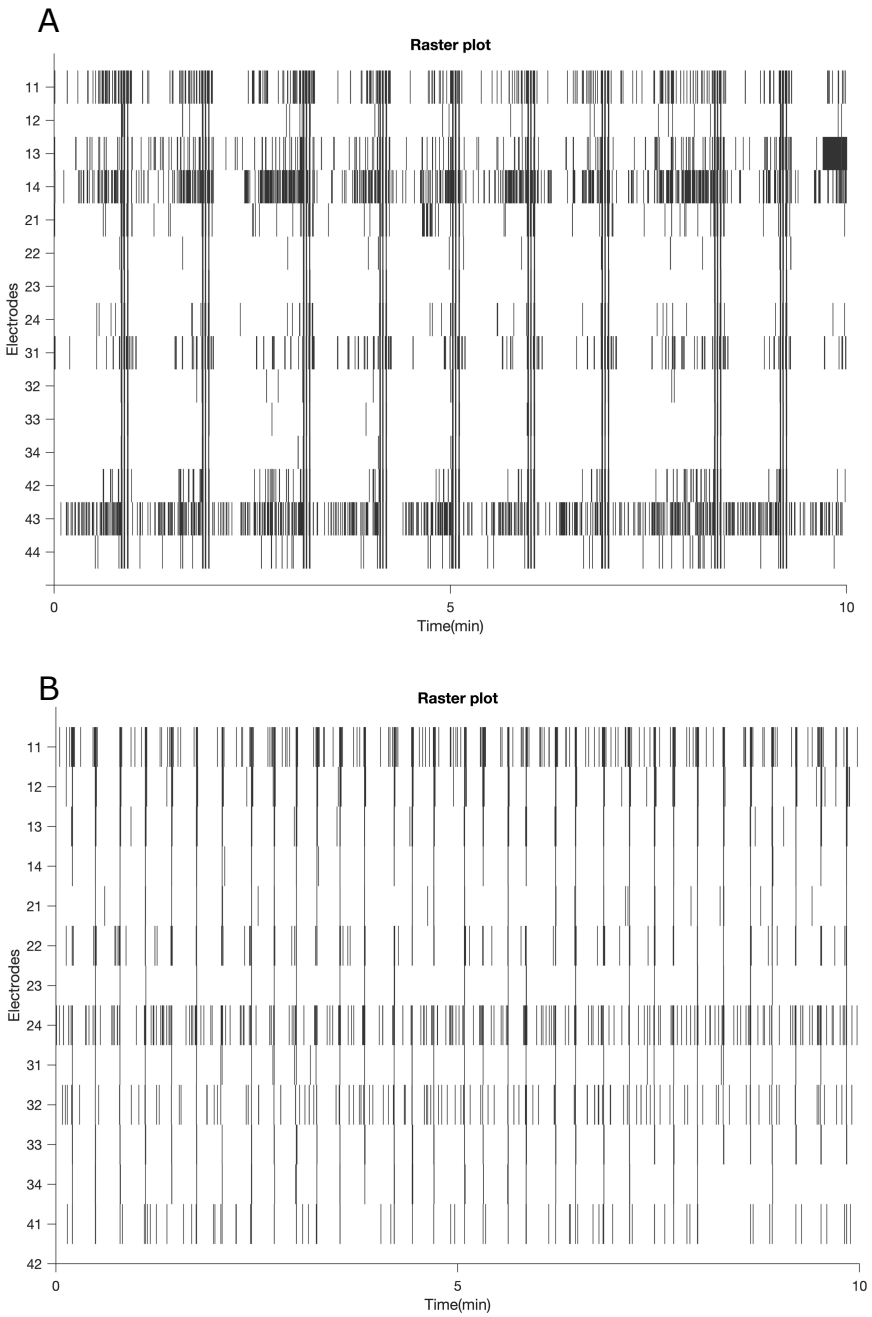

Fig. 23. Example raster plots for two networks on 16-electrode MEA. A) Raster plot for a network with healthy neurons at 54 DIV (baseline). The electrode numbers are aligned along the y-axis. Electrodes with less than 5 spikes/minute are excluded. The x-axis shows the time in minutes for ten minutes of the 60-minute recording. Each vertical line represents a spike. **B)** Raster plot for a network with ALS patient-specific neurons at 54 DIV (baseline).

4.2.3 Developments in MFR and CI for the healthy group

The compare the baseline activity and response to hypoxia between the healthy and the ALS group, the MFR for each experimental group in each condition (Healthy and ALS) was compared, as well as the CI, a measure for the synchronization of activity in the network. At baseline (i.e. before hypoxia, Fig 24A), there were variations in the MFR for all of the groups in the healthy condition, but it remained stable within each group. Following hypoxia, larger fluctuations in MFR were observed for all the healthy experimental groups. The MFR for the untreated non-hypoxic group did not change significantly at 55 DIV, one day after hypoxia, but did increase after that and started fluctuating a little from 57 DIV. The MFR for the GABA-treated non-hypoxic group did not increase much one day after hypoxia, but did clearly increase after that, although a data point for 56 DIV is missing. At 58 DIV the MFR decreased again, before increasing and stabilizing from 60 DIV onward. The MFR for the untreated hypoxic group clearly increased one day after hypoxia, before decreasing again at 56 DIV and then increasing up until 59 DIV. From 59 DIV onward, the MFR increased and decreased from day to day. The MFR for the GABA-treated hypoxic group increased following hypoxia, but not as much as for the untreated hypoxic group (however, the data point for 55 DIV is missing). The MFR for this group consistently increased until 59 DIV, after which the MFR increased and decreased in the same manner as for the untreated hypoxic group, but with larger fluctuations.

The CI for the healthy networks remained between 5 and 15 during the baseline recordings (Fig. 25A). Similar to the MFR, larger fluctuations were observed for the CI following hypoxia. The CI for the untreated non-hypoxic group had the lowest fluctuations in CI. The CI for the GABA-treated non-hypoxic group decreased in the days following stimulation, increased from 57 DIV to 58 DIV, and then appeared to stabilize at a level slightly lower than baseline. The CI for the untreated hypoxic group decreased one day after hypoxia and had some fluctuations in the following days. From 59 DIV onward, the CI for this group increased and decreased in an alternating fashion from day to day. The CI for the GABA-treated non-hypoxic group, appeared to steadily decrease until 59 DIV, but some data points are missing here. From 59 DIV onward, the CI increased and decreased from day to day.

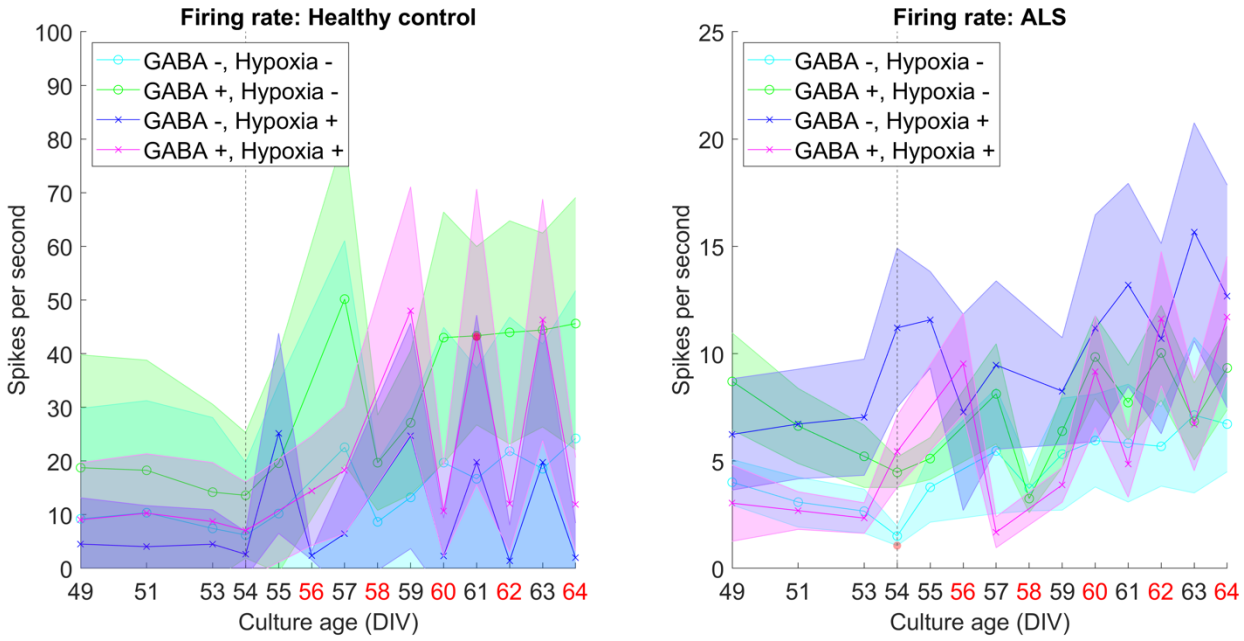

Fig. 24. Mean firing rate (MFR) for the healthy and ALS group before and after hypoxia. A) MFR for the healthy group. The firing rate in spikes per second is represented along the y-axis. The culture age is shown along the x-axis, red days indicate days of media change (which were done after recording). The dashed vertical line at 54 DIV marks the day of hypoxia. **B)** MFR for the ALS group. Note the differences between the y-axes.

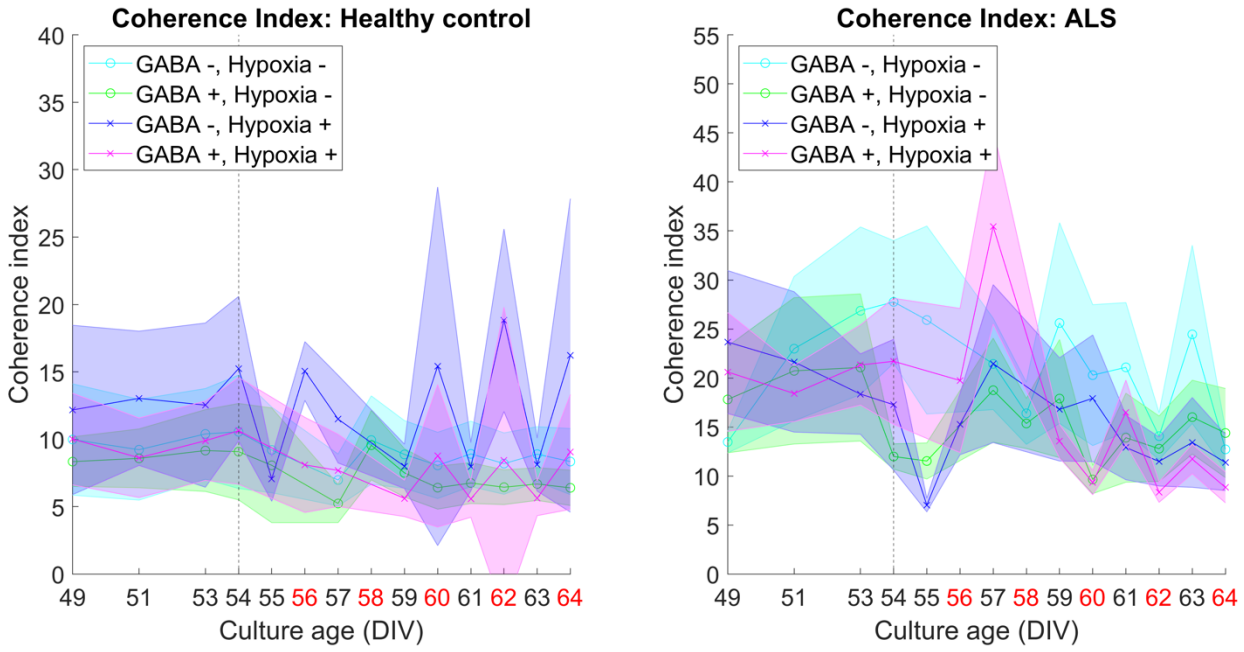

Fig. 25. Coherence index (CI) for the healthy and ALS group before and after hypoxia. A) CI for the healthy group. The CI (synchronization of the network) is represented along the y-axis. The culture age is shown along the x-axis, red days indicate days of media change (which were done after recording). The dashed vertical line at 54 DIV marks the day of hypoxia. **B)** CI for the ALS group.

4.2.4 Developments in MFR and CI for the ALS group

The MFR for the ALS group was much lower than for the healthy group (Fig. 24B). The MFR also appeared to decrease slightly during the baseline recordings, except for the untreated hypoxic group. Larger fluctuations in MFR were also observed following hypoxia in the ALS group. The MFR for the untreated non-hypoxic group had a steady increase in MFR up until 64 DIV, except for a slight decrease at 58 DIV. The MFR for the GABA-treated non-hypoxic group also increased in the days following stimulation, but then started fluctuating more. From 59 DIV the alternating pattern of increased and decreased MFR from day to day became evident also here. The MFR for the untreated hypoxic group did not appear to change one day after hypoxia but started fluctuating in the following days and also appeared to have an overall increase in MFR during the remainder of the experiment. The MFR for the GABA-treated hypoxic group had a missing data point one day following hypoxia, but had increased at 56 DIV. After this, a clear decrease in MFR was observed, before it started to increase and decrease from day to day from 59 DIV onward, in the same pattern as for the GABA-treated non-hypoxic group.

Overall, the CI for the ALS group was higher than for the healthy group (Fig. 25B). At baseline, the CI varied slightly from day to day within the different experimental groups and between the groups, but the fluctuations were larger following hypoxia. The CI for the untreated non-hypoxic group had some quite large fluctuations in CI during the entire experiment. However, the CI changes more abruptly after 58 DIV. The CI for the GABA-treated non-hypoxic group did not change much at one day after stimulation but started fluctuating after this. There appeared to be an overall decrease in CI for this group compared to baseline over the ten days following stimulation. The CI for the untreated hypoxic group decreased following hypoxia, and then increased again over the next two days. From 57 DIV onward, the CI for this group steadily decreased, although some fluctuations occurred from day to day. The CI for the GABA-treated hypoxic group did not change much in the first two days after hypoxia, although the data point for 55 DIV is missing. However, the CI clearly increased from 56 to 57 DIV, before decreasing again and, although some fluctuations occurred, the overall CI decreased compared to baseline.

4.3 Experiment 3: Direct reprogramming of adult human fibroblasts

4.3.1 Morphological and structural development of reprogrammed fibroblasts

The fibroblasts attached well to the surfaces of the six-well plates and were transduced when they reached approximately 90-100 % confluency. Fibroblasts are elongated with an elliptical nucleus. Following transduction, no major visible morphological changes appeared (Fig. 26A and D). Two days after Dox induction, on the same day as the selection antibiotics were added, there were still no clearly visible changes (Fig. 26B and E). However, four days after Dox induction, detachment and cell death were prominent. Dead cells were free-floating and had a round but uneven shape (Fig. 26C and F). The color was bright with beige and/or white dots, indicative of stress vacuoles. Surviving cells retained the characteristic shape of fibroblasts.

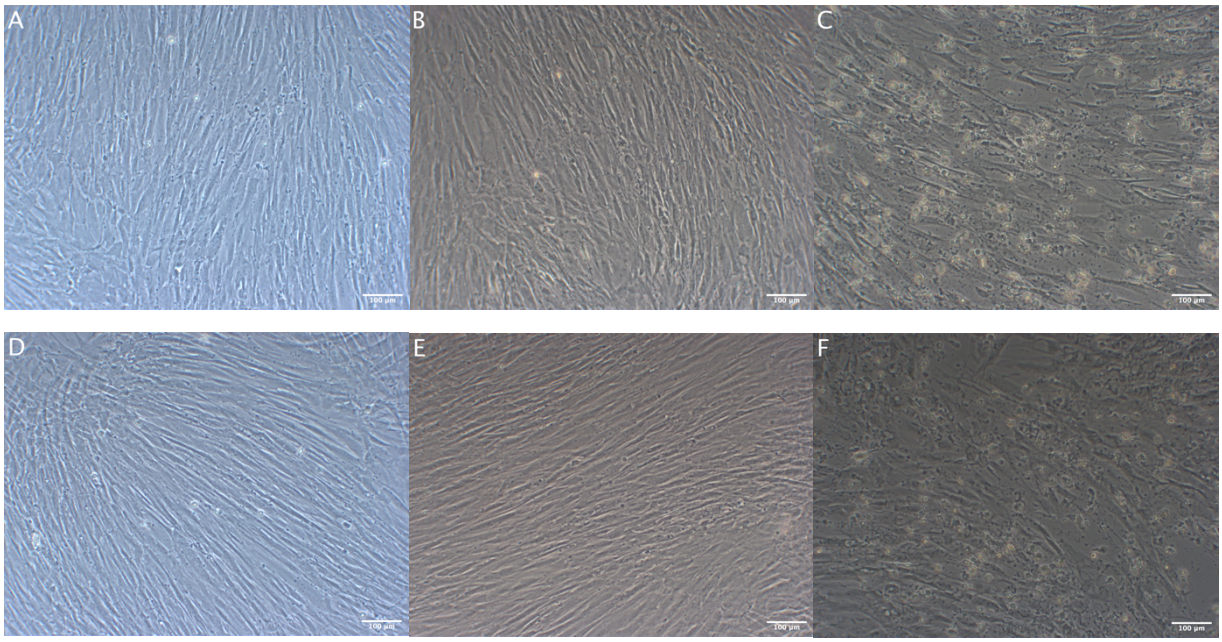

Fig. 26. Phase contrast images of adult human fibroblasts from an ALS patient (A, B, C) and from a healthy individual (D, E, F). These images show the development of the fibroblasts 18 hours after transfection (A, D), two days after Dox induction (B, E) and two days after the start of the antibiotic selection process, just prior to re-plating (C, F). All images are taken with Zeiss microscope using a Zeiss 20x/0.3 NA objective. 100 µm scale bar.

Following re-plating, a substantial amount of the cells detached and died. In the MEAs, surviving cells primarily attached around the edges of the MEA, but some cells attached in the electrode area as well (Fig. 27). The ALS patient-specific cells attached better in the electrode area than the healthy cells. However, although the cultures generally looked sparse, in the days following re-plating the cells that did attach gradually adopted a more neuron-like morphology. The middle part of the cells became smaller and rounder and started looking like the soma. The elongations became thinner and some of them started to grow neurites and form connections with other cells. After the seeding of astrocytes, the cells gradually started to look unhealthy. Stress vacuoles were present in the cultures four days after seeding the astrocytes (Fig. 28A). Six days after seeding astrocytes, the cells started to detach, and the cultures looked sparser (Fig. 28B). Nevertheless, the were still many surviving cells, with clear neurites and axons. However, two weeks later almost all cells had detached (Fig. 28C). The activity of the cells was recorded at 30 DIV, but there was no clear activity.

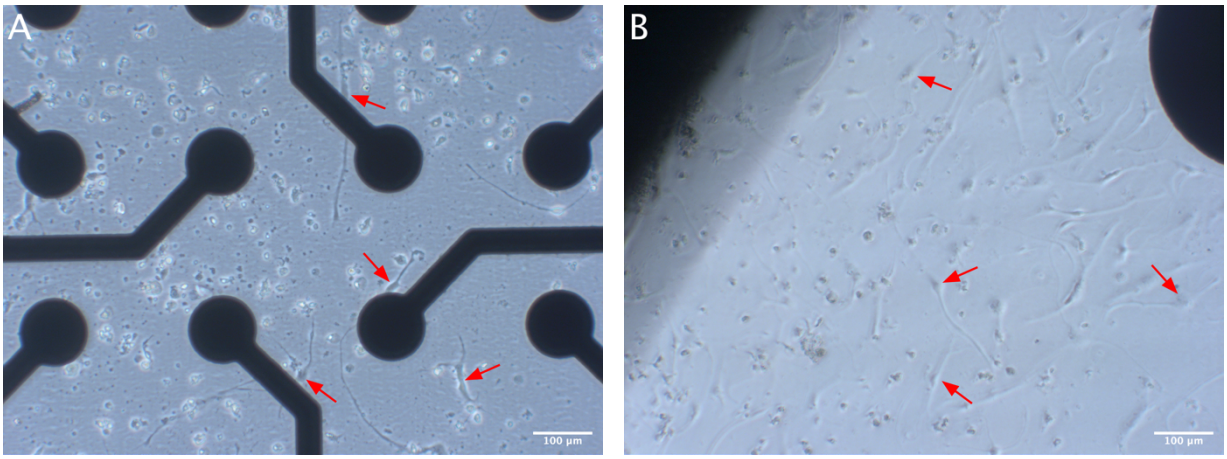

Fig. 27. Phase contrast images of healthy directly reprogrammed motor neurons on MEA. These images show a network of healthy reprogrammed neurons six days after seeding astrocytes. The neurons did not attach well in the electrode tip area (**A**), and there were little neurite extensions with the exception of a few cells (red arrows). The neurons attached better in the periphery along the edge of the MEA (**B**, cells highlighted with red arrows). All images are taken with Zeiss microscope using a Zeiss 20x/0.3 NA objective (A) and . 100 µm scale bar.

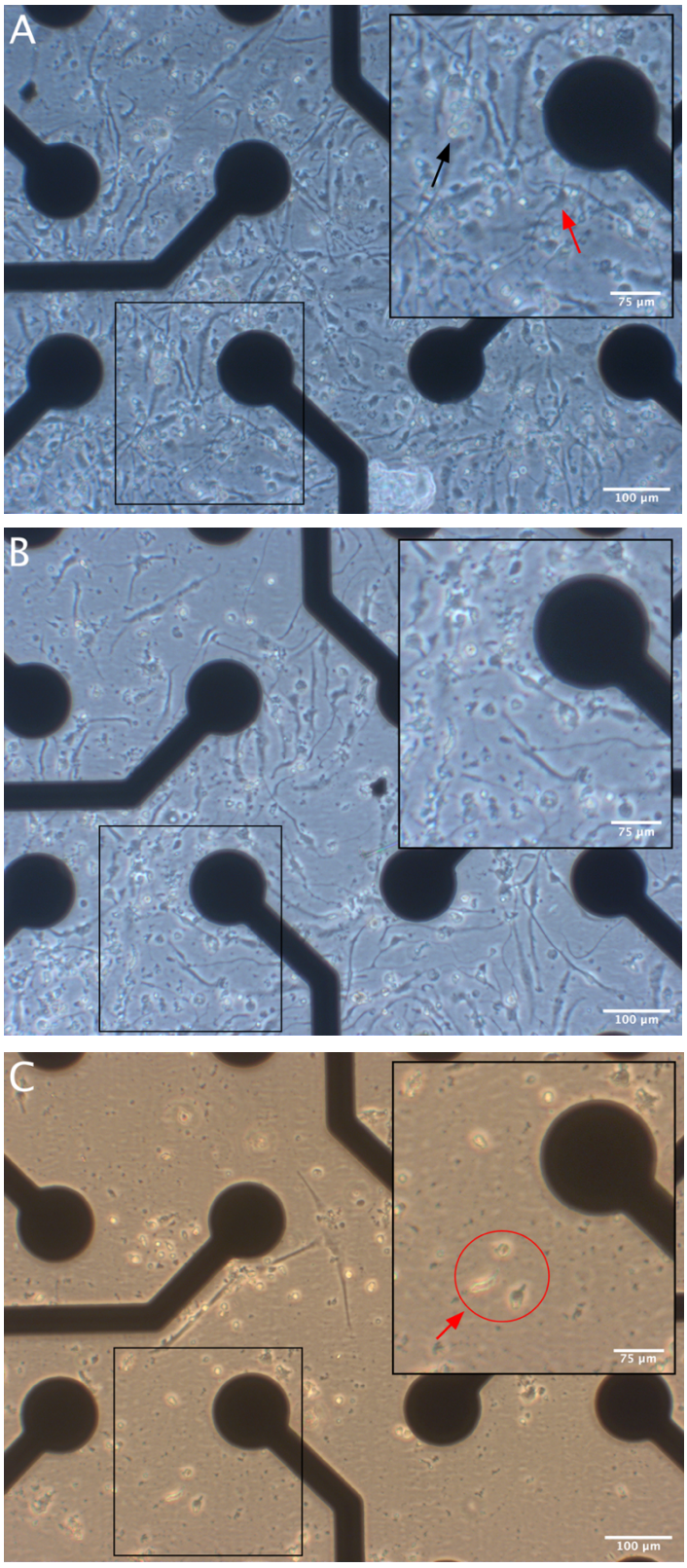

Fig. 28. Phase contrast images of ALS patient-specific directly reprogrammed motor neurons on MEA. These images show the development of the same network of ALS-patient specific cells. **A)** The network four days after the seeding of astrocytes. There were some dead cells (black arrow) but most of the cells attached well and the neurons started to adopt a neuron-like morphology (red arrow). **B)** The network six days after seeding astrocytes, and the network look sparser compared to A. **C)** The network 20 days after seeding astrocytes. Almost all of the cells were dead or dying at this point. The black circle highlights an area of dying cells. All images are taken with Zeiss microscope using a Zeiss 20x/0.3 NA objective. 100 µm scale bar. 75 µm scale bar on insets.

In the microfluidics, the cells attached well, both the ALS patient-specific cells and the healthy cells (Fig. 29). However, many of them had a round shape without clear elongations or neurites, a morphology characteristic to that of dying cells. The cells retained this morphology after seeding astrocytes, and the astrocytes did not appear to attach well. Over the next weeks, the cells did not detach, but there were no major developments in their morphology, and they did not adopt a typical neuron-like shape. The activity of the cells in the microfluidics was also recorded at 30 DIV, but the networks were silent. Similar to the MEAs, the cells in the ibidis attached primarily around the edges. Furthermore, detachment and cell death were more prominent in the ibidis than in the MEAs and microfluidics. After seeding astrocytes in the ibidis, the reprogrammed cells clustered on top of the astrocytes. They were also bright or white in color, suggesting that they were stressed.

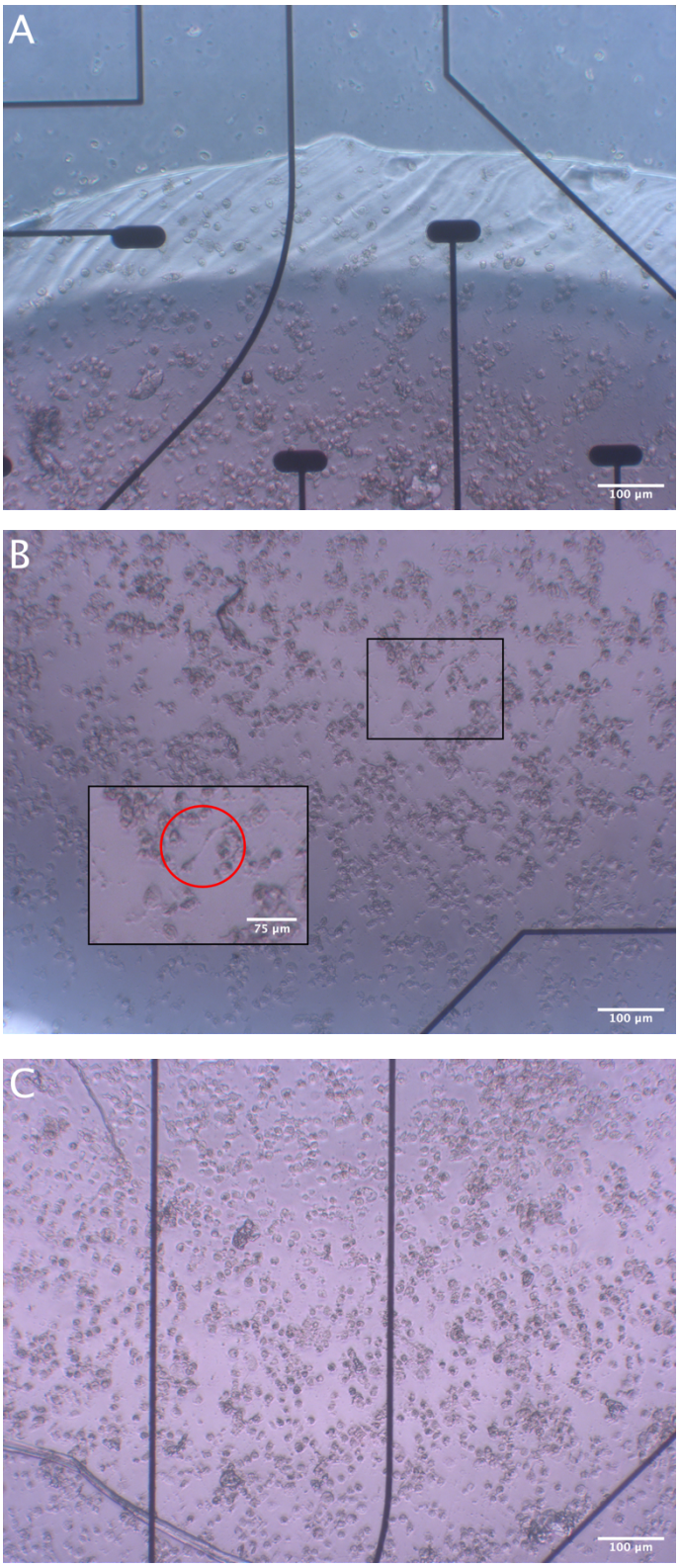

Fig. 29. Phase contrast images of directly reprogrammed neurons on microfluidic chip with MEA interface. A) The top chamber with ALS patient-specific neurons. **B)** and **C)** shows the middle and bottom well with healthy neurons. Most of the cells had a round shape with minimal neurite extensions. The red circle in B highlights a cell that had started to develop into a neuron. All images are taken with Zeiss microscope using a Zeiss 20x/0.3 NA objective. 100 µm scale bar. 75 µm scale bar on inset.

Discussion

The aim of this thesis was to establish a structured *in vitro* neural network to model and recapitulate electrophysiological aspects of disease progression in ALS. This entailed stimulating structured neural networks on microfluidic chips as a proof of concept of how perturbations can progress between interconnected chambers in Experiment 1. Differences in electrophysiological activity between healthy and ALS-patient specific neurons at baseline and in response to stress (hypoxic conditions) were assessed in Experiment 2. Finally, human fibroblasts were directly converted into MNs and plated on MEAs and microfluidic chips to assess ALS disease progression in Experiment 3. Experiment 1 demonstrates that perturbations to one chamber only can cause effects that affect the entire structured network. Experiment 2 suggests that there are some differences in the activity of healthy and ALS patient-specific neurons, but the overall low activity warrant these results to be interpreted with caution. Finally, the fibroblasts were successfully transduced but did not develop into fully mature and electrically active neurons, thereby preventing us from examining the spread of ALS to healthy neurons.

5.1 Spread of perturbations in structured neural networks

As mentioned in the introduction, the highly complex and interconnected nature of the brain affects the functionality of the network, and vice versa[78]. Furthermore, disease propagates more easily between areas that are more extensively connected[38]. Thus, the study of neural network behavior and neurodegenerative disease progression necessitate models that make it possible to recapitulate these features. Structuring *in vitro* neural networks as we did in the microfluidic chips, enable us to investigate the functional consequences of perturbations, even at more distant sites. Interestingly, following stimulation with NMDA in the top chamber only, we found that the MFR decreased (Fig. 14A). One potential reason for this could be that the overstimulation caused the neurons to fire excessively at first, which was then followed by a decrease in activity. This is consistent with similar results from the Sandvig group using Kainate acid to stimulate the top chamber[98]. Here, the MFR during stimulation also decreased compared to baseline, but this was due to an overactivation at first, followed by an abrupt decrease in activity at single electrodes. When assessing the MFR for each of the chambers in our experiment, the top chamber did not appear to have higher activity than the other chambers (Fig. 16). As we only assessed the MFR, it could be that such a transient overactivation occurred only at some electrodes, but the general activity level during stimulation was lower for all the microfluidic chips compared to baseline during the entirety of the stimulation (Fig. 17). Thus, no evident overactivation early on was observed in the processed data. Yet, the visualization of the spiking activity during recording showed more activity for the electrodes in the top chamber than in the other chambers during the whole recording (Fig. 18). As such, another potential reason for the decreased MFR could be that the spikes were not identified during data processing. The spike sorting sets a standard deviation based on the baseline activity (i.e. background noise) during that recording. Activity deviating from that standard deviation is identified as spikes. If the baseline activity is high, the standard deviation will be set higher, and if many electrodes are very active, the activity might not be captured as spikes but as background noise instead. Accordingly, the NMDA stimulation most likely produced overactivation in the top well, but this was not captured during spike sorting and therefore the MFR appeared to decrease following perturbation.

In contrast to the MFR, the correlation within each microfluidic chip increased following stimulation. Based on the correlation matrices in Fig. 19 and 20, the within-chamber correlation for the bottom chamber was high prior to stimulation. The between-chamber correlation between the top and the middle chamber appeared to be stronger in MIP1 compared to the between-chamber correlations for the bottom and the middle chamber, but only for some electrodes. The between-chamber correlation between the top and the bottom chambers was low. This is expected, as there are in all likelihood no direct links between the top and the bottom chambers. In MIP3, the between-chamber correlation was strong for the bottom and middle chambers, but not for the top and the middle chambers. A strong between-chamber correlation between the bottom and the middle chamber is expected as there are probably direct links between the chambers. However, due to direct connections between the top and the middle chambers we also expected to find a correlation similar to the one between the bottom and the middle chamber. As becomes clear when studying the total network correlation at baseline, there were variations between the different microfluidic chips. This could be a reflection of the differences in the underlying structure of the networks. It is possible that the structural connectivity between the bottom and the middle chambers was stronger than the connectivity between the top and the middle. However, one day after stimulation, it appeared that the between-chamber correlation increased for both of the microfluidic chips, whereas the within-correlation for the top chamber decreased, especially for MIP3. Prior to stimulation, the bottom chamber appeared to have stronger links to the middle chamber, especially for MIP3, but this shifted during stimulation for both microfluidic chips. The within-chamber correlation for the top chamber increased, as well as the between-chamber correlation for the top and the middle chambers. The alterations in correlations were quite similar for both of the chips which could suggest that the stimulation in the top chamber amplified the communication between the top and the middle chamber, leading to an increase in the correlation between the two. Following stimulation, the overall network correlation appeared to have increased for both chips. Furthermore, the between-chamber correlation for the top and middle chambers remained stronger than prior to stimulation. This was even clearer for MIP3, where it seemed like the top chamber took over some of the influence the bottom chamber had on the middle chamber. There might have been some underlying plasticity mechanisms strengthening the connections between the top and middle chamber, resulting in increased synchronization across the entire network due to the links between the middle and bottom chambers. Thus, there appeared to be structural connections through all chambers, but the functional connections might not have been equally strong throughout the entire network at baseline, but then seemed to be altered following stimulation.

The alterations in functional connectivity following perturbation extended beyond the direct links in the structured networks, as there appeared to be increased correlation between the top and the bottom chambers. This is reminiscent of a small-world network organization. As described in the introduction, the small-world network is characterized by high local clustering, and a few long-range connections bridging the entire network via a few intermediate steps[91]. Thus, the structural connections between the different chambers in the 3-nodal microfluidic chip can represent these long-range connections, and the alterations in synchronization across the entire network appear to mimic the spread of activity via short-path lengths between any given pair of nodes in the network. The small-world organization is believed to optimize information processing by local specialization and global integration[92]. Our results from Experiment 1 suggests that the overactivation in one part of the network increased overall network synchronization, while also partly destroying the local synchronization within the stimulated chamber. Although we did not

observe an increase in overall network activity, this could indicate that segregation of information might become impaired following spread of perturbation in a network. The small-world organization might also have implications for the spread of disease, as the underlying topology of the brain can shape disease progression[38]. The impaired local specialization combined with increased global integration might result in less segregation of pieces of information and translated to an *in vivo* neurodegenerative disease like ALS might manifest itself in impairment of cognitive skills or impaired integration of motor skills and fine motor control.

The effects of perturbations in a network with a small-world organization also depend on which nodes are affected as perturbations spread more profoundly when affecting connector hubs[39]. In Experiment 1, we saw that the network correlation increased for three of the microfluidic chips over the days following stimulation and decreased and almost reached baseline for one of the chips (MIP1). When comparing the correlation matrices for MIP1 and MIP3, the pattern of decreased within-chamber correlation for the top well and increased between-chamber correlations was not as strong for MIP1 as for MIP3. Instead, the between-chamber correlation for the bottom and the middle chambers remained quite strong following stimulation, although it decreased during stimulation. Thus, it is possible that more neurons with extensive connections within the chamber were affected differently in MIP3 and MIP1. If connector hubs become significantly affected by perturbations, and communicate with large parts of the network, the overall activity or synchronization of the network will most likely also become clearly affected by the perturbation. However, if there are fewer connector hubs initially, or these are less affected by the perturbation, the perturbation might not spread as profoundly. It is possible that some of the neurons in the top chamber of MIP1 were well-connected to the middle chamber, but less connected within its own chamber, and as such the within-chamber correlation did not show the same pattern as seen in MIP3, i.e. a strong increase during stimulation, followed by a decrease one day after stimulation. It is also possible that if fewer connector hubs were affected in MIP1, the perturbation did not spread as profoundly overall, and this can explain why the total network correlation for MIP1 decreased to baseline a few days after stimulation.

In general, the consequences of the perturbation appeared to be considerably determined by the underlying structure in the networks. Thus, controlling the structure of modeled neural networks with the use of microfluidic chips can generate a more relevant setting for modeling neurodegenerative disease spread, especially in the context of a small-world topology. The small-world organization may also have implications for the emergence of critical dynamics. One study found that critical states only emerge in network topologies with small-world features[99]. The combination of local segregation *via* short-range connections and global integration *via* a few long-range connections, should support the generation of neuronal avalanches of all sizes[100]. Due to time constraints we were not able to directly assess criticality measures such as power law distribution of avalanche sizes, but the increased total network correlation following stimulation implies that the activity becomes increasingly synchronized. Although we did not observe an increase in MFR, this could be indicative of a super critical state, as observed in epileptic seizures[90]. As discussed in the introduction, deviations from criticality might be a sign of dysfunction or disease in the brain. Therefore, the investigation of criticality in healthy neural networks, and how such properties are affected by perturbations, might reveal network dynamics relevant for neurodegenerative diseases like ALS.

It should be emphasized that the results from Experiment 1 are merely preliminary and there are several limitations with the study. First of all, the fact that we did not observe the increased MFR that was expected following overexcitation makes it difficult to make any conclusions about the data purely based on correlation analyses. Thus, more extensive statistical analyses assessing activity at an electrode basis, as well as more in-depth investigations of correlation in terms of significance testing should have been incorporated. However, due to time constraints this was not completed. Secondly, there was some misalignment of the electrodes so some of the electrodes belonging to a specific chamber were aligned under the tunnels instead. Consequently, the interpretation of which electrodes belongs to which chamber is not completely accurate. Thirdly, we did not confirm that the NMDA stimulation was confined to the top chamber only. The flow barrier should ensure this, but live microscopy of fluorescently labeled ROS production can be applied to confirm this (see ref. 98 for details on this). As such, there is a possibility that the effects of the stimulation occurred due to a flow of NMDA through the tunnels. Nevertheless, Experiment 1 suggests that perturbations to a fluidically isolated chamber affect the network activity and that these effects can spread over long-range connections to more distant parts of the network.

5.2 Differences in activity between healthy and ALS patient-specific neurons

The results from the ICC assays for the ALS patient-specific cells in Experiment 2 cast doubt about the identity of the cells, as they did not express Islet1, an essential factor for several aspects of MN development (Fig. 22)[101]. Furthermore, the ALS cells were clearly less active than the healthy cells based on MFR and the spiking activity presented in the raster plots, even after low-activity electrodes had been excluded (Fig. 23 and Fig. 24). This is not consistent with previous findings showing hyperexcitability in *in vitro* studies with ALS-specific neurons from both mice and human iPSCs[102,103]. Yet, there appears to be some spiking activity based on the MFR and the raster plots, and the CI has been calculated for all groups, although some data points are missing. It is possible that the cells were simply not fully mature yet. The supplier of the cells (Axol Biosciences) recommended seven weeks of maturation (i.e. 49 DIV) before the cells were fully active, and the cells used for ICC were fixed after nine weeks, at 64 DIV. However, other work in our lab with the same cell type found expression of Islet1 at a later stage for some of these cells. Furthermore, a general trend observed for the MFR of the ALS-specific neurons was that it appeared to increase toward the end of the experiment. Thus, the cells might have been premature, or possibly have been in a mixed population of MNs and non-neuronal cells, and this puts some constraints on what conclusions can be made from the data.

Overall, the network synchronization appeared to decrease slightly following hypoxia for both the healthy and the ALS group through the course of the experiment (Fig. 25). Also, the synchronization for the ALS group was higher than the synchronization for the healthy group at baseline, but toward the end of the experiment it approached the same level that was observed for the healthy group at baseline. Higher synchronization in ALS-specific cells is consistent with previous findings, showing that synchronization between different brain areas increases in ALS patients[104]. Although such findings are based on imaging techniques and the level of investigation is at the macroscale rather than the mesoscale like in our *in vitro* models, it is not surprising that such a trait could be recapitulated at the network level. Diffusion Tensor Imaging (DTI) has shown impairments in the structural network in

ALS patients, affecting the communication between different motor regions[105]. This suggest that ALS also affects the capacity of different motor regions to connect and communicate, and this may very well become apparent in single networks as well, as the *in vitro* method requires the neurons to self-organize into a coherent and well-connected network. Further elaborating this, it has been suggested that changes in functional connectivity and synchronization might be an effect of reduced structural connectivity[106]. Thus, the fact that the CI for the ALS networks was higher than the healthy networks at baseline might reflect an underlying impairment in the self-organization and wiring of the network. However, increased functional connectivity in ALS has also been related to hyperexcitability[107], a feature that was not observed in our results. In this regard, increased activity and synchronization could be considered a result of plasticity mechanisms initiated to compensate for increasing limb weakness[107,108]. Yet, the low MFR in the ALS networks in our results make this an unlikely explanation for the higher CI. It is possible that higher synchronization was simply caused by a general lack of activity in the networks. Oftentimes, we have observed higher synchronization in early phases of the development of neural network activity, when there are few neurons active. This could be caused by the connections between the few neurons that are active, and therefore they fire together. This was also observed in Experiment 1, where the total network correlation was higher at 11 DIV, when the MFR was lower (Fig. 13). This is also consistent with the observation that as the MFR for the ALS networks increased toward the end of the recording period, the CI decreased.

An interesting finding for the hypoxic groups in the healthy networks was that following 59 DIV, the MFR started fluctuating from day to day (Fig. 24A). The MFR decreased on days of media change and increased on days of no media change. The media change was always made after recordings. The decreases in MFR might therefore have been a reaction to a low level of nutrition in the media. The MFR increased again on the days following a media change, when the nutrition level had been replenished. Interestingly, as the MFR decreased on days of media change, the CI increased. Thus, this could corroborate the arguments made above, that when the activity is lower, the synchronization becomes higher. Fluctuations in MFR from 59 DIV was also observed for the GABA-treated hypoxic group in the ALS networks (Fig. 24B). However, this was in the opposite direction, i.e. the MFR increased on days of media change and then decreased on days of no media change. The untreated hypoxic ALS group showed a similar pattern of fluctuations as the healthy groups, but the fluctuations were not as large. Consistent with the findings from the healthy networks, the CI for the GABA-treated hypoxic ALS group also increased when the MFR decreased, and decreased when the MFR increased on the days after 59 DIV. Hence, there appeared to be a delayed effect of the hypoxia exposure which led to large fluctuations in activity following 59 DIV. A possible explanation for the hypoxic healthy networks can be that hypoxic conditions made the networks more stressed and thereby more vulnerable to low levels of nutrition. For the GABA-treated hypoxic ALS networks, the hypoxia also appears to have induced some level of stress a few days later, but this seems to be more independent of the nutrition level in the media. Furthermore, as observed, the overall MFR for all the ALS networks was significantly lower compared to the healthy networks, and the ALS networks seemed to be less affected by the hypoxic conditions. However, due to the low activity it is difficult to determine whether there were any actual differences between the healthy and the ALS patient-specific cells, and whether these results are representative. This should therefore be further investigated in future studies using more electrically active neurons with clear confirmation of cell type.

5.3 Direct reprogramming of human adult fibroblasts

Our final step was to investigate the spread of the differences in activity between healthy and ALS patient-specific directly reprogrammed cells in the 3-nodal microfluidic chip. The results from the direct reprogramming showed that some of the fibroblasts did start to structurally develop into neurons, but they did not survive for long, nor did they exhibit electrophysiological activity. It generally seemed like the cells did not handle the re-plating procedure very well, as detachment and cell death became more prominent after this stage.

The electrophysiological activity in the MEAs was recorded after the cells had started to detach and die, and the cultures were therefore quite sparse at this point. Thus, the lack of activity could be caused by the lack of connections within the network. The cells also attached better in the periphery of the MEA culture chamber where there are no electrodes, so if these cells were active, this would not have been captured by the electrodes (Fig. 27). In general, the ALS cells attached better around the electrodes than the healthy cells. A potential reason for this could be that the surface was allowed longer time to dry after removing the coating in these wells (as discussed in more detail below). The cells in the microfluidic chips had still not detached when the activity was recorded, but they did not look like fully developed neurons, and the round shape and lack of neurites suggests that they were not healthy (Fig. 29). The lack of electrophysiological activity could therefore also be a result of the general health of the cells. The direct reprogramming is a harsh treatment, where the cells are infected with viruses, exposed to a large amount of antibiotics and then re-plated, all within a few days. Furthermore, Trypsin-EDTA is used to detach the cells during the re-plating, a compound that is also known to be hard on the cells[109]. However, the small well diameter makes it hard to study the neural networks in the microfluidic chips with the microscope, and thus it is difficult to make any conclusions about the state of the networks purely based on visual inspection.

As mentioned in the introduction, there are two fundamental characteristics of the CNS that can be recapitulated *in vitro*, i.e. self-organization and emergence of electrophysiological activity. The fact that some of the MEA cultures developed into networks in the early phases following re-plating suggest that there are some inherent self-organizing properties in these cells. However, as the cultures aged the cells started to die, and as such they did not self-organize into fully structured neural networks. One reason for the cell death could be that the astrocytes did not attach properly, and thus the reprogrammed cells did not get the metabolic support they needed. Astrocytes have been shown to be important for both neuronal attachment and survival[110]. Two days before seeding astrocytes, the culture media containing selection antibiotics was removed, a crucial part of the protocol as the selection antibiotics kill all the cells that have not been infected with the virus. However, if any remainders of the media containing selection antibiotics were left in the wells, this could have killed some of the astrocytes, and can be a reason for the poor attachment. In summary, the attempt to establish neural networks with directly reprogrammed cells was unsuccessful, however, several steps in the protocol could be improved to yield better results in the future.

First of all, we transduced and re-plated a large number of fibroblasts at once (1 million). This is more cells than what has been used in previous attempts on culturing directly reprogrammed cells in the lab. This also means that we needed a correspondingly large

amount of virus to efficiently transduce as many cells as possible. However, evenly distributing this amount of virus, especially as the fibroblasts might have started to layer on top of each other, might prove difficult. Additionally, the large number of cells made the re-plating time consuming, and the cells might have started to die before we were able to actually plate them. As mentioned above, the direct reprogramming is a harsh process and as such the cells might be less robust to re-plating than other types of cells. Transducing and re-plating a smaller number of cells at once can therefore ensure a more equal distribution of viruses, as well as making the re-plating more efficient. A second point is that the surfaces of the wells should dry before seeding (during re-plating) to avoid that the cells float out to the edges/periphery as observed in the MEAs and ibidis. We seeded the cells directly after removing the coating, but other work with directly reprogrammed cells in the Sandvig group has reported better attachment when letting the surfaces dry for a while before seeding (unpublished material). In the microfluidics however, it is desirable with some coating left for the cells to float toward the tunnels. A third potential improvement could be to add another media change prior to the seeding of astrocytes to ensure that all selection antibiotics are completely removed. This might result in better attachment for the astrocytes which again could improve survival for the reprogrammed cells, both in terms of metabolic support and long-term attachment.

5.4. Limitations

As highlighted throughout this thesis there are many advantages of using *in vitro* methods, and they can recapitulate fundamental features of the CNS. However, certain limitations still need to be addressed. First of all, as mentioned in the introduction, the neurons are removed from their natural environment. Although certain aspects of this is remodeled with the use of astrocytes in co-culture, and the culture media and culture vessel coating mimicking the extracellular environment, the cultured neural networks are still studied in isolation from the rest of the brain. Several cell types are missing in our cultures, such as microglia, oligodendrocytes and interneurons, and the functional interplay and structural connectivity between different regions of the brain are lost in such reductionistic models. Furthermore, the brain is a 3-dimensional organization, but the *in vitro* models used in this thesis are only 2-dimensional. The functional connectivity of the network is dependent on the underlying structure and removing these structural features might exclude several properties important for the functionality of the network.

Secondly, although MEAs can capture important traits of the neural network activity, the electrodes only record the fluctuations in voltage in close proximity to any given electrode. As such, the recorded activity cannot reflect single neuron activity nor activity from the entire network. Furthermore, the random organization of cultured neurons on MEAs results in high variance in the measured electrophysiological activity. It can therefore be challenging to statistically analyze the data and draw generalized conclusions, as became evident in both Experiment 1 and 2, where there were large variations in the datasets.

Lastly, there are many inherent advantages of using iPSCs/directly reprogrammed cells, especially in disease modeling. Nevertheless, there can be variations between cell lines, and as observed in Experiment 3, the procedure of directly reprogramming cells can be time consuming and challenging. Furthermore, there might be unknown consequences related to the modifications of the epigenome. In the end, reductionistic models are

necessary in the context of neuroscientific research at the meso- and microscale, but the implications of the results must be interpreted with these limitations in mind.

5.5 Future directions

This thesis demonstrates that perturbations can spread across chambers in the microfluidic chip despite fluidic isolation, yet we failed to demonstrate that this chip can be used to model disease spread in ALS. Nevertheless, as has been demonstrated in other work in the Sandvig group, it is possible to establish neural networks using directly reprogrammed cells (both from ALS patients and healthy individuals) in microfluidic chips (unpublished material). Thus, the logical next step should be to incorporate the improvements for the direct conversion protocol mentioned above to examine whether this yields a more robust model. When established, the model can be used to not only study the spread of abnormal electrophysiological activity, but also the spread of other disease-indicating markers such as ROS, alterations in pH-levels, inflammatory markers or protein aggregates. Furthermore, the model can be used to study the spread of disease between neurons and non-neuronal cells. By co-culturing healthy astrocytes with ALS patient-specific neurons it is possible to look for inflammatory markers in the astrocytes. Moreover, ALS patient-specific astrocytes can be co-cultured with healthy neurons to examine the spread of disease from non-neuronal cells to neurons.

In our original experimental design, we attempted to test the dying-forward hypothesis by examining whether ALS spreads *via* axonal projections to healthy cells in the adjacent chamber. However, it is also possible to alter the design to study the dying-backward hypothesis. The direction of the growth of axonal projections into the tunnels can be guided by seeding the wells at different time points. By seeding healthy cells in the top well, letting the axons grow for some time, and then seeding ALS-patient specific cells in the middle well, it is possible to study whether ALS can spread in a dying back manner to the top chamber. Furthermore, this design can be used to model a spinal cord/neuromuscular junction, with ALS patient-specific neurons in the top well, healthy neurons in the middle well, and myocytes in the bottom well, to study the spread all the way from UMNs to LMNs, to the muscle.

In a long-term perspective it is desirable to identify characteristics of ALS disease progression that can be identified at initial stages for early intervention. To accomplish this, it is necessary with a better understanding of the structure-function relationships in the healthy state. Many challenges remain, but the recent advancements in *in vitro* techniques combined with other methodological approaches are starting to bridge the gap between the healthy and the diseased brain.

Conclusion

The overall purpose of this thesis was to investigate how the structural and functional dynamics of neural networks shape the spread of pathology in the context of ALS. We have established that induced perturbations can spread in multi-nodal *in vitro* neural networks, however, we were not able to recapitulate the disease progression of ALS.

In Experiment 1 we saw that induced overstimulation applied to one chamber only in the microfluidic chip did not result in increased MFR, but it did alter the synchronization of the network behavior, both within the chambers and between the chambers. Specifically, the overall network synchronization between all the chambers increased, whereas the within-chamber correlation for the stimulated chamber appeared to decrease following stimulation. This suggest that perturbations in a limited part of the network can have widespread effects on the global network activity, while simultaneously partly breaking down the local synchronization within the perturbed parts. In Experiment 2 we investigated the differences in activity and synchronization between healthy and ALS patient-specific cells under normal conditions and following a stress-inducing event (hypoxia). These results imply that there are some inherent differences in the activity of the two groups, but due to a low activity level and uncertainty concerning the cell identity, these results were inconclusive. In Experiment 3, we were not able to successfully implement the direct reprogramming of adult human fibroblasts and use these to model disease spread. However, the results from the early phases indicate that a more successful and robust conversion protocol can be generated by incorporation of the improvements mentioned above. In conclusion, these preliminary findings show that it is possible to model the effects of structure-function relationships on the spread of perturbations *in vitro*, although we were unable to demonstrate it specifically for ALS. This thus constitutes a promising approach for the study of neurodegenerative disease progression in future studies.

References

1. Bento-Abreu, A., Van Damme, P., Van Den Bosch, L. & Robberecht, W. The neurobiology of amyotrophic lateral sclerosis. *Eur. J. Neurosci.* **31**, 2247–2265 (2010).
2. Zarei, S. *et al.* A comprehensive review of amyotrophic lateral sclerosis. *Surg. Neurol. Int.* **6**, (2015).
3. Robberecht, W. & Philips, T. The changing scene of amyotrophic lateral sclerosis. *Nat. Rev. Neurosci.* **14**, 248–264 (2013).
4. Taylor, J. P., Brown, R. H. & Cleveland, D. W. Decoding ALS: From genes to mechanism. *Nature* **539**, 197–206 (2016).
5. Kaus, A. & Sareen, D. Als patient stem cells for unveiling disease signatures of motoneuron susceptibility: Perspectives on the deadly mitochondria, ER stress and calcium triad. *Front. Cell. Neurosci.* **9**, 1–26 (2015).
6. Ragagnin, A. M. G., Shadfar, S., Vidal, M., Jamali, M. S. & Atkin, J. D. Motor neuron susceptibility in ALS/FTD. *Front. Neurosci.* **13**, (2019).
7. Rosen, D. R. *et al.* lateral sclerosis. **362**, 59–62 (1993).
8. Ilieva, H., Polymenidou, M. & Cleveland, D. W. Non-cell autonomous toxicity in neurodegenerative disorders: ALS and beyond. *J. Cell Biol.* **187**, 761–772 (2009).
9. Parone, P. A. *et al.* Enhancing mitochondrial calcium buffering capacity reduces aggregation of misfolded SOD1 and motor neuron cell death without extending survival in mouse models of inherited amyotrophic lateral sclerosis. *J. Neurosci.* **33**, 4657–4671 (2013).
10. Therrien, M., Dion, P. A. & Rouleau, G. A. ALS: Recent Developments from Genetics Studies. *Curr. Neurol. Neurosci. Rep.* **16**, (2016).
11. Neumann M., et al. Phosphorylated TDP-43 in frontotemporal lobar degeneration and amyotrophic lateral sclerosis. *Science (80-.).* **314**, 130–133 (2006).
12. Prasad, A., Bharathi, V., Sivalingam, V., Girdhar, A. & Patel, B. K. Molecular mechanisms of TDP-43 misfolding and pathology in amyotrophic lateral sclerosis. *Front. Mol. Neurosci.* **12**, 1–36 (2019).
13. Braak, H. *et al.* Amyotrophic lateral sclerosis - A model of corticofugal axonal spread. *Nat. Rev. Neurol.* **9**, 708–714 (2013).
14. Uryu, K. et al. Concomitant TAR-DNA-binding protein 43 pathology is present in Alzheimer Disease and corticobasal degeneration but not in other tauopathies. *J Neuropathol Exp Neurol* **67**, 555–564 (2008).
15. Do-Ha, D., Buskila, Y. & Ooi, L. Impairments in Motor Neurons, Interneurons and Astrocytes Contribute to Hyperexcitability in ALS: Underlying Mechanisms and Paths to Therapy. *Mol. Neurobiol.* **55**, 1410–1418 (2018).
16. Petri, S. *et al.* Distribution of GABAA receptor mRNa in the motor cortex of ALS patients. *J. Neuropathol. Exp. Neurol.* **62**, 1041–1051 (2003).
17. Pieri, M., Carunchio, I., Curcio, L., Mercuri, N. B. & Zona, C. Increased persistent sodium current determines cortical hyperexcitability in a genetic model of amyotrophic lateral sclerosis. *Exp. Neurol.* **215**, 368–379 (2009).
18. Shibuya, K. *et al.* Markedly reduced axonal potassium channel expression in human sporadic amyotrophic lateral sclerosis: An immunohistochemical study. *Exp. Neurol.* **232**, 149–153 (2011).
19. Yamanaka, K. & Komine, O. The multi-dimensional roles of astrocytes in ALS. *Neurosci. Res.* **126**, 31–38 (2018).
20. Coyle, J. T. & Puttfarcken, P. Oxidative Stress, Glutamate, and Neurodegenerative Disorders. *Science (80-.).* **262**, 689–695 (1993).
21. Tadic, V., Prell, T., Lautenschlaeger, J. & Grosskreutz, J. The ER mitochondria calcium cycle and ER stress response as therapeutic targets in amyotrophic lateral sclerosis. *Front. Cell. Neurosci.* **8**, 1–17 (2014).
22. Van Den Bosch, L., Van Damme, P., Bogaert, E. & Robberecht, W. The role of excitotoxicity in the pathogenesis of amyotrophic lateral sclerosis. *Biochim. Biophys. Acta - Mol. Basis Dis.* **1762**, 1068–1082 (2006).

23. Alexianu, M. E. *et al.* The role of calcium-binding proteins in selective motoneuron vulnerability in amyotrophic lateral sclerosis. *Ann. Neurol.* **36**, 846–858 (1994).
24. Kawahara, Y. *et al.* Human spinal motoneurons express low relative abundance of GluR2 mRNA: An implication for excitotoxicity in ALS. *J. Neurochem.* **85**, 680–689 (2003).
25. Eisen, A. & Weber, M. The motor cortex and amyotrophic lateral sclerosis. *Muscle and Nerve* **24**, 564–573 (2001).
26. Chou, S. M. & Norris, F. H. Amyotrophic lateral sclerosis: Lower motor neuron disease spreading to upper motor neurons. *Muscle Nerve* 864–869 (1993) doi:10.1016/B978-1-4160-2591-7.10101-8.
27. Campanari, M. L., Bourefis, A. R. & Kabashi, E. Diagnostic challenge and neuromuscular junction contribution to ALS pathogenesis. *Front. Neurol.* **10**, 1–8 (2019).
28. Dupuis, L. & Loeffler, J. P. Neuromuscular junction destruction during amyotrophic lateral sclerosis: insights from transgenic models. *Curr. Opin. Pharmacol.* **9**, 341–346 (2009).
29. Eisen, A. *et al.* Cortical influences drive amyotrophic lateral sclerosis. *J. Neurol. Neurosurg. Psychiatry* **88**, 917–924 (2017).
30. McAlary, L., Plotkin, S. S., Yerbury, J. J. & Cashman, N. Prion-like Propagation of Protein Misfolding and Aggregation in Amyotrophic Lateral Sclerosis. *Front. Mol. Neurosci.* **12**, 262 (2019).
31. Maniecka, Z. & Polymenidou, M. From nucleation to widespread propagation: A prion-like concept for ALS. *Virus Res.* **207**, 94–105 (2015).
32. Brettschneider, J. *et al.* Stages of pTDP-43 pathology in amyotrophic lateral sclerosis. *Ann. Neurol.* **74**, 20–38 (2013).
33. Irwin, D. J. *et al.* Evaluation of potential infectivity of Alzheimer and Parkinson disease proteins in recipients of cadaver-derived human growth hormone. *JAMA Neurol.* **70**, 462–468 (2013).
34. Nagai, M. *et al.* Astrocytes expressing ALS-linked mutated SOD1 release factors selectively toxic to motor neurons. *Nat. Neurosci.* **10**, 615–622 (2007).
35. Grad, L. I. *et al.* Intercellular propagated misfolding of wild-type Cu/Zn superoxide dismutase occurs via exosome-dependent and -independent mechanisms. *Proc. Natl. Acad. Sci. U. S. A.* **111**, 3620–3625 (2014).
36. Ayers, J. I., Fromholt, S. E., O'Neal, V. M., Diamond, J. H. & Borchelt, D. R. Prion-like propagation of mutant SOD1 misfolding and motor neuron disease spread along neuroanatomical pathways. *Acta Neuropathol.* **131**, 103–114 (2016).
37. Feiler, M. S. *et al.* TDP-43 is intercellularly transmitted across axon terminals. *J. Cell Biol.* **211**, 897–911 (2015).
38. Fornito, A., Zalesky, A. & Breakspear, M. The connectomics of brain disorders. *Nat. Rev. Neurosci.* **16**, 159–172 (2015).
39. Honey, C. J. & Sporns, O. Dynamical consequences of lesions in cortical networks. *Hum. Brain Mapp.* **29**, 802–809 (2008).
40. Philips, T. & Robberecht, W. Neuroinflammation in amyotrophic lateral sclerosis: Role of glial activation in motor neuron disease. *Lancet Neurol.* **10**, 253–263 (2011).
41. Lino, M. M., Schneider, C. & Caroni, P. Accumulation of SOD1 Mutants in Postnatal Motoneurons Does Not Cause Motoneuron Pathology or Motoneuron Disease. *J. Neurosci.* **22**, 4825–4832 (2002).
42. Pramatarova, A., Laganière, J., Roussel, J., Brisebois, K. & Rouleau, G. A. Neuron-specific expression of mutant superoxide dismutase 1 in transgenic mice does not lead to motor impairment. *J. Neurosci.* **21**, 3369–3374 (2001).
43. Beers, D. R. *et al.* Wild-type microglia extend survival in PU.1 knockout mice with familial amyotrophic lateral sclerosis. *Proc. Natl. Acad. Sci. U. S. A.* **103**, 16021–16026 (2006).

44. Yamanaka, K.; Seung Joo Chun, Severine Biollee, Noriko Fujimori-Tonou, Hirofumi Yamashita, David H. Gutmann, Ryosuke Takahashi, Hidemi Misawa, D. W. C. Astrocytes as determinants of disease progression in inherited ALS. *Nat. Neurosci.* **11**, 1–5 (2011).
45. Philips, T. *et al.* Oligodendrocyte dysfunction in the pathogenesis of amyotrophic lateral sclerosis. *Brain* **136**, 471–482 (2013).
46. Philips, T. & Rothstein, J. D. Rodent models of amyotrophic lateral sclerosis. *Curr. Protoc. Pharmacol.* **2015**, 5.67.1-5.67.21 (2015).
47. Aggarwal, S. & Cudkowicz, M. ALS Drug Development: Reflections from the Past and a Way Forward. *Neurotherapeutics* **5**, 516–527 (2008).
48. Guo, W., Fumagalli, L., Prior, R. & van den Bosch, L. Current advances and limitations in modeling ALS/FTD in a dish using induced pluripotent stem cells. *Front. Neurosci.* **11**, 1–20 (2017).
49. Takahashi, K. & Yamanaka, S. Induction of Pluripotent Stem Cells from Mouse Embryonic and Adult Fibroblast Cultures by Defined Factors. *Cell* **126**, 663–676 (2006).
50. Karagiannis, P. *et al.* Induced pluripotent stem cells and their use in human models of disease and development. *Physiol. Rev.* **99**, 79–114 (2019).
51. Van Damme, P., Robberecht, W. & Van Den Bosch, L. Modelling amyotrophic lateral sclerosis: Progress and possibilities. *DMM Dis. Model. Mech.* **10**, 537–549 (2017).
52. Patterson, M. *et al.* Defining the nature of human pluripotent stem cell progeny. *Cell Res.* **22**, 178–193 (2012).
53. Vierbuchen, T. *et al.* Direct conversion of fibroblasts to functional neurons by defined factors. *Nature* **463**, 1035–1041 (2010).
54. Yoo, A. S. *et al.* MicroRNA-mediated conversion of human fibroblasts to neurons. *Nature* **476**, 228–231 (2011).
55. Abernathy, D. G. *et al.* MicroRNAs Induce a Permissive Chromatin Environment that Enables Neuronal Subtype-Specific Reprogramming of Adult Human Fibroblasts. *Cell Stem Cell* **21**, 332-348.e9 (2017).
56. Lu, Y. L. & Yoo, A. S. Mechanistic insights into MicroRNA-induced neuronal reprogramming of human adult fibroblasts. *Front. Neurosci.* **12**, 1–9 (2018).
57. Huh, C. J. *et al.* Maintenance of age in human neurons generated by microRNA-based neuronal conversion of fibroblasts. *Elife* **5**, 1–14 (2016).
58. Victor, M. B. *et al.* Striatal neurons directly converted from Huntington's disease patient fibroblasts recapitulate age-associated disease phenotypes. *Nat. Neurosci.* **21**, 341–352 (2018).
59. Tononi, G., Sporns, O. & Edelman, G. M. A measure for brain complexity: Relating functional segregation and integration in the nervous system. *Proc. Natl. Acad. Sci. U. S. A.* **91**, 5033–5037 (1994).
60. Telesford, Q. K., Simpson, S. L., Burdette, J. H., Hayasaka, S. & Laurienti, P. J. The Brain as a Complex System: Using Network Science as a Tool for Understanding the Brain. *Brain Connect.* **1**, 295–308 (2011).
61. Tessier-Lavigne, M. & Goodman, C. S. The Molecular Biology of Axon Guidance. *Science (80-.).* **274**, 1123–1133 (1996).
62. Luhmann, H. J. *et al.* Spontaneous neuronal activity in developing neocortical networks: From single cells to large-scale interactions. *Front. Neural Circuits* **10**, 1–14 (2016).
63. Jones, I. L. *et al.* The potential of microelectrode arrays and microelectronics for biomedical research and diagnostics. *Anal. Bioanal. Chem.* **399**, 2313–2329 (2011).
64. Morin, F. *et al.* Constraining the connectivity of neuronal networks cultured on microelectrode arrays with microfluidic techniques: A step towards neuron-based functional chips. *Biosens. Bioelectron.* **21**, 1093–1100 (2006).
65. van de Wijdeven, R. *et al.* A novel lab-on-chip platform enabling axotomy and neuromodulation in a multi-nodal network. *Biosens. Bioelectron.* **140**, 111329 (2019).

66. Forró, C. *et al.* Modular microstructure design to build neuronal networks of defined functional connectivity. *Biosens. Bioelectron.* **122**, 75–87 (2018).
67. Mateos-Aparicio, P. & Rodríguez-Moreno, A. The impact of studying brain plasticity. *Front. Cell. Neurosci.* **13**, 1–5 (2019).
68. Sharma, N., Classen, J. & Cohen, L. G. *Neural plasticity and its contribution to functional recovery*. *Handbook of Clinical Neurology* vol. 110 (Elsevier B.V., 2013).
69. Yee, A. X., Hsu, Y. T. & Chen, L. A metaplasticity view of the interaction between homeostatic and hebbian plasticity. *Philos. Trans. R. Soc. B Biol. Sci.* **372**, (2017).
70. Turrigiano, G. Homeostatic synaptic plasticity: Local and global mechanisms for stabilizing neuronal function. *Cold Spring Harb. Perspect. Biol.* **4**, 1–17 (2012).
71. Zhao, C., Deng, W. & Gage, F. H. Mechanisms and Functional Implications of Adult Neurogenesis. *Cell* **132**, 645–660 (2008).
72. Mahar, M. & Cavalli, V. Intrinsic mechanisms of neuronal axon regeneration. *Nat. Rev. Neurosci.* **19**, 323–337 (2018).
73. Schwab, M. & Strittmater, S. Nogo limits neural plasticity and recovery from injury. *Curr. Opin. Neurobiol.* **23**, 1–7 (2014).
74. Klein, R. Bidirectional modulation of synaptic functions by Eph/ephrin signaling. *Nat. Neurosci.* **12**, 15–20 (2009).
75. Van Hoecke, A. *et al.* EPHA4 is a disease modifier of amyotrophic lateral sclerosis in animal models and in humans. *Nat. Med.* **18**, 1418–1422 (2012).
76. Birger, A., Ottolenghi, M., Perez, L., Reubinoff, B. & Behar, O. ALS-related human cortical and motor neurons survival is differentially affected by Sema3A article. *Cell Death Dis.* **9**, (2018).
77. Lo, E. H. Degeneration and repair in central nervous system disease. *Nat. Med.* **16**, 1205–1209 (2010).
78. Bullmore, E. & Sporns, O. Complex brain networks: Graph theoretical analysis of structural and functional systems. *Nat. Rev. Neurosci.* **10**, 186–198 (2009).
79. Passingham, R. E., Stephan, K. E. & Kötter, R. The anatomical basis of functional localization in the cortex. *Nat. Rev. Neurosci.* **3**, 606–616 (2002).
80. Marder, E. & Goaillard, J. M. Variability, compensation and homeostasis in neuron and network function. *Nat. Rev. Neurosci.* **7**, 563–574 (2006).
81. Voytek, B. & Knight, R. T. Dynamic network communication as a unifying neural basis for cognition, development, aging and disease. *Physiol. Behav.* **77**, 1089–1097 (2015).
82. Ghatak, S. *et al.* Mechanisms of hyperexcitability in alzheimer's disease hiPSC-derived neurons and cerebral organoids vs. Isogenic control. *Elife* **8**, 1–22 (2019).
83. Sporns, O., Tononi, G. & Edelman, G. M. Connectivity and complexity: The relationship between neuroanatomy and brain dynamics. *Neural Networks* **13**, 909–922 (2000).
84. Hesse, J. & Gross, T. Self-organized criticality as a fundamental property of neural systems. *Front. Syst. Neurosci.* **8**, 1–14 (2014).
85. Bak, P., Tang, C. & Wiesenfeld, K. Self-organized criticality. *Phys Rev A* **38**, 364–375 (1988).
86. Marković, D. & Gros, C. Power laws and self-organized criticality in theory and nature. *Phys. Rep.* **536**, 41–74 (2014).
87. Beggs, J. M. & Plenz, D. Neuronal Avalanches in Neocortical Circuits. *J. Neurosci.* **23**, 11167–11177 (2003).
88. Valverde, S., Ohse, S., Turalska, M., West, B. J. & Garcia-Ojalvo, J. Structural determinants of criticality in biological networks. *Front. Physiol.* **6**, 1–9 (2015).
89. Moretti, P. & Muñoz, M. A. Griffiths phases and the stretching of criticality in brain networks. *Nat. Commun.* **4**, (2013).
90. Meisel, C., Storch, A., Hallmeyer-Elgner, S., Bullmore, E. & Gross, T. Failure of adaptive self-organized criticality during epileptic seizure attacks. *PLoS Comput. Biol.* **8**, (2012).
91. Watts, D. J. & Strogatz, S. H. Collective dynamics of 'small-world' networks. *Nature* **393**, 440–442 (1998).

92. Bassett, D. S. & Bullmore, E. Small-world brain networks. *Neuroscientist* **12**, 512–523 (2006).
93. Bassett, D. S. & Bullmore, E. T. Small-World Brain Networks Revisited. *Neuroscientist* **23**, 499–516 (2017).
94. Alstott, J., Breakspear, M., Hagmann, P., Cammoun, L. & Sporns, O. Modeling the impact of lesions in the human brain. *PLoS Comput. Biol.* **5**, (2009).
95. van de Wijdeven, R. *et al.* Structuring a multi-nodal neural network in vitro within a novel design microfluidic chip. *Biomed. Microdevices* **20**, (2018).
96. Wang, X. J. Pacemaker neurons for the theta rhythm and their synchronization in the septohippocampal reciprocal loop. *J. Neurophysiol.* **87**, 889–900 (2002).
97. Richner, M., Victor, M. B., Liu, Y., Abernathy, D. & Yoo, A. S. MicroRNA-based conversion of human fibroblasts into striatal medium spiny neurons. *Nat. Protoc.* **10**, 1543–1555 (2015).
98. Valderhaug, V. D., Ramstad, O. H. & Wijdeven, R. Van De. Structural and functional alterations associated with the LRRK2 G2019S mutation revealed in structured human neural networks. *bioRxiv* (2020).
99. Massobrio, P., Pasquale, V. & Martinoia, S. Self-organized criticality in cortical assemblies occurs in concurrent scale-free and small-world networks. *Sci. Rep.* **5**, 1–16 (2015).
100. Friedman, N. *et al.* Universal critical dynamics in high resolution neuronal avalanche data. *Phys. Rev. Lett.* **108**, 1–5 (2012).
101. Liang, X. *et al.* Isl1 Is required for multiple aspects of motor neuron development. *Mol. Cell. Neurosci.* **47**, 215–222 (2011).
102. Marcuzzo, S. *et al.* Hyperexcitability in Cultured Cortical Neuron Networks from the G93A-SOD1 Amyotrophic Lateral Sclerosis Model Mouse and its Molecular Correlates. *Neuroscience* **416**, 88–99 (2019).
103. Wainger, B. J. *et al.* Intrinsic membrane hyperexcitability of ALS patient-derived motor neurons. *Cell Rep.* **7**, 1–11 (2014).
104. Sorrentino, P. *et al.* Brain functional networks become more connected as amyotrophic lateral sclerosis progresses: a source level magnetoencephalographic study. *NeuroImage Clin.* **20**, 564–571 (2018).
105. Verstraete, E. *et al.* Motor network degeneration in amyotrophic lateral sclerosis: A structural and functional connectivity study. *PLoS One* **5**, 1–9 (2010).
106. Douaud, G., Filippini, N., Knight, S., Talbot, K. & Turner, M. R. Integration of structural and functional magnetic resonance imaging in amyotrophic lateral sclerosis. *Brain* **134**, 3467–3476 (2011).
107. Geevasinga, N. *et al.* Brain functional connectome abnormalities in amyotrophic lateral sclerosis are associated with disability and cortical hyperexcitability. *Eur. J. Neurol.* **24**, 1507–1517 (2017).
108. Agosta, F. *et al.* Sensorimotor functional connectivity changes in amyotrophic lateral sclerosis. *Cereb. Cortex* **21**, 2291–2298 (2011).
109. Huang, H. *et al.* Trypsin-induced proteome alteration during cell subculture in mammalian cells. *J Biomed Sci* **17**, (2010).
110. Wang, X. F. & Cynader, M. S. Effects of astrocytes on neuronal attachment and survival shown in a serum-free co-culture system. *Brain Res. Protoc.* **4**, 209–216 (1999).

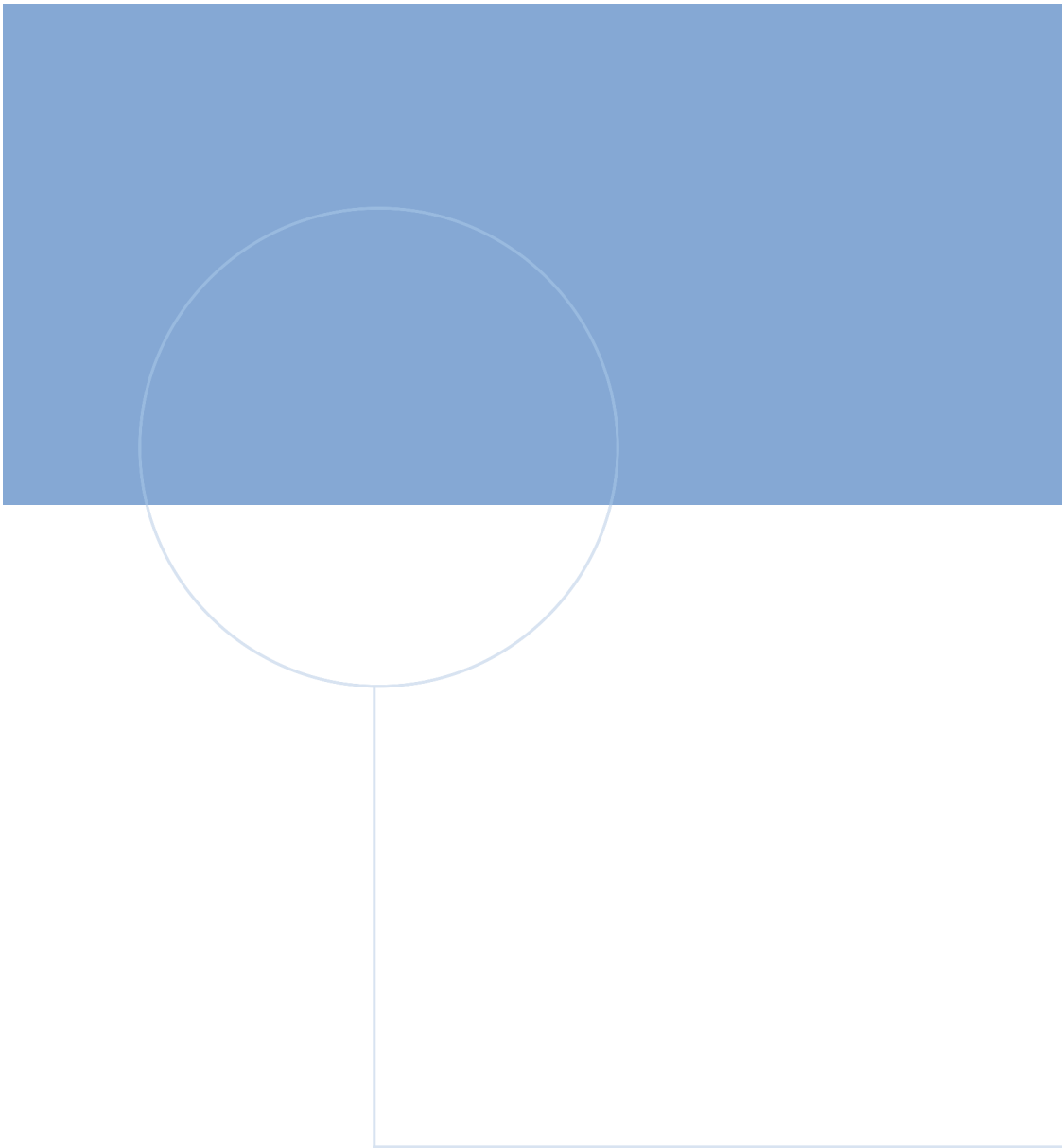

NTNU

Norwegian University of
Science and Technology